Impact of Aerothermal Modeling on the Estimation of Turbine Blade Life

by

Jean E. Collin

B. Eng. Mechanical Engineering
McGill University (Montreal), 2002

Submitted to the Department of Mechanical Engineering
In Partial Fulfillment of the Requirements for the
Degree of

MASTER OF SCIENCE IN MECHANICAL ENGINEERING

at the

MASSACHUSETTS INSTITUTE OF TECHNOLOGY
[September 2004]
August 2004

Signature of Author _____
Department of Mechanical Engineering
August 13, 2004

Certified by _____
Edward M. Greitzer
H. N. Slater Professor of Aeronautics and Astronautics
Thesis Supervisor

Certified by _____
David L. Darmofal
Associate Professor of Aeronautics and Astronautics
Thesis Supervisor

Certified by _____
Bora Mikic
Professor of Mechanical Engineering
Thesis Reader

Accepted by _____
Ain A. Sonin
Professor of Mechanical Engineering
Chairman, Department Graduate Committee

IMPACT OF AEROTHERMAL MODELING ON THE ESTIMATION OF TURBINE BLADE LIFE

by

Jean E. Collin

Submitted to the Department of Mechanical Engineering
On August 13, 2004 in partial fulfillment of the requirements for the degree of
Master of Science in Mechanical Engineering

Abstract

The impact of aerothermal modeling on estimates of turbine blade heat transfer and life was assessed for three high pressure turbine blades. The work was conducted as part of a project aimed at the evaluation of the effect of variability on turbine life. Pressure and thermal loads were extracted from numerical simulations, postprocessed, and used as external boundary conditions in thermal-structural calculations aimed at the estimation of blade life.

Deterministic calculations of life showed that blade life differences of 17% and 34%, relative to the baseline blade, were primarily due to structural differences between the blades rather than differences in external aerodynamic and heat transfer characteristics. The simulation results for the three blade geometries were used to construct *probabilistic* external thermal boundary conditions with variability based on expected in-service variability for heat transfer coefficient and convection temperature. In a parallel study, these were used as noise parameters, along with metal and thermal barrier coating conductivity, thermal barrier coating thickness, internal cooling temperature, and internal heat transfer coefficient, in three probabilistic blade life calculations. Consistent with the deterministic findings, a weak to moderate correlation was found between the variability in external thermal conditions and that in blade life. The key driver of life variability was the variability in the internal cooling temperature.

The impact of modeling approximations and geometric and flow features on blade life was also investigated on one of the nominal geometries. A set of two-dimensional numerical results were used to assess the impact of using simplified data in the estimation of life. Geometric and flow features considered in three-dimensional studies were a seal cavity between rotor and stator, seal cavity flow, fillet geometry, and inlet boundary layers with and without seal cavity. Despite differences in blade external heat transfer of 10% - 15% in the life-limiting region, the estimated life for all blades in these studies was within 2.6% of the nominal.

For turbine blades of similar design and operating conditions, given our modeling approach, it was concluded that (1) the level of heat transfer differences observed between blade designs does not play an important role in the estimation of blade life and (2) high fidelity modeling of external aerothermodynamics is not required for reliable life estimates.

Thesis Supervisors:	Dr. Edward M. Greitzer
	Dr. David L. Darmofal
Titles:	H. N. Slater Professor of Aeronautics and Astronautics
	Associate Professor of Aeronautics and Astronautics

Acknowledgements

My goal at MIT was to acquire practical research and engineering experience among the world's best. Many people have contributed to my satisfaction of this goal and I would like to take this opportunity to thank them.

First, I would like to thank Professors Edward M. Greitzer and David L. Darmofal for their contributions to my development as an engineer. Their guidance throughout my time at MIT were key. I would also like to thank Dr. Victor E. Garzon and Dr. Yifang Gong for their friendship and technical contributions during this work. I would like to express my thanks to Professor Bora Mikic for his technical advice and for agreeing to be my Mechanical Engineering thesis reader, even while on sabbatical.

I would like to thank Mitsubishi Heavy Industries, and in particular, Dr. Sunao Aoki and Mr. Hideaki Sugishita for having sponsored and provided the necessary inputs for the project. Their collaboration ensured that the results of the work were germane to the industrial sector.

I would like to thank my labmates, Matt Lackner, Yong Wang, Andrew Luers and Apostolos Kountras for their friendship and tolerance of the everpresent coffee odor permeating our office. In particular, I would like to thank Apostolos for his camaraderie, advice, and for his part of the project without which my work would have been incomplete.

This thesis would not have been possible without the support of Paul Warren and Garrett Barter for the many computer problems encountered, Julie Finn for the administrative issues associated with working on a team project, and Holly Anderson and Mary McDavitt for making the software acquisition process as painless as possible.

Other MIT students, far removed from my project, also contributed to my success here. There are too many to name but of particular importance are my roommates, Frank O'Sullivan and longtime undergraduate friends and fellow Building 31 inhabitants, Grant Smedley and Mathieu Bernier to all of whom I am indebted for their friendship and support.

I am deeply indebted to my girlfriend and fellow mechanical engineer, Tristany Tang, whose patience, understanding, and advice throughout these two long years have been nothing short of extraordinary. Finally, I would like to dedicate this thesis to my parents Michel and Nicole and my brother Chuck, without whose unwavering love, support, and patience I would not have been able to complete my work.

Table of Contents

Acknowledgements **5**

List of Figures **11**

List of Tables **15**

Nomenclature **17**

1. Introduction **21**

1.1 Motivation and Background 21

1.2 Problem Statement 22

1.3 Objectives 23

1.4 Overall Approach 23

1.5 Outline of Thesis 25

1.6 Contributions 27

2. Computational Modeling Approach **29**

2.1 Grid Generation for High-Fidelity Heat Transfer Simulations 29

2.2 Flow Solver 30

2.3 Turbulence Modeling for High-Fidelity Heat Transfer Simulations 30

2.4 CFD Case Setup 31

2.4.1 Computational Grids 31

2.4.2 Boundary Conditions 34

2.5 Validation of Computational Setup 37

2.6 Estimation of Life 41

3. Impact of Blade Design on Heat Transfer and Life **43**

3.1 Heat Transfer Governing Flow Features 44

3.2 Heat Transfer Comparison of Nominal Blades 45

3.2.1 Heat Transfer Comparison in Life-Limiting Region 49

3.3 Comparison of Deterministic Life Estimates 49

3.4 Comparison of Probabilistic Life Estimates 51

4. Impact of Modeling Approximations on Heat Transfer and Life **55**

4.1 Two-Dimensional Flow 55

4.1.1 Description of Study 55

4.1.2 Global Heat Transfer Observations 58
4.1.3 Heat Transfer Differences and Trends 59
4.1.4 Comparison of Two- and Three-Dimensional CFD Results 61
4.1.6 Thermal – Structural Analyses 63
4.2 Impact of Geometric and Flow Modeling on Blade Life Estimation 66
4.2.1 Effect of Seal Cavity 66
4.2.1.1 Description of Study 66
4.2.1.2 Overall Heat Transfer Comparison 67
4.2.1.3 Heat Transfer Comparison in Life-Limiting Region 69
4.2.1.4 Effect of Seal Cavity on Blade Life 70
4.2.2 Effect of Seal Flow 71
4.2.2.1 Description of Study 71
4.2.2.2 Overall Heat Transfer Comparison 71
4.2.2.3 Heat Transfer Comparison in Life-Limiting Region 74
4.2.2.4 Effect of Seal Flow on Blade Life 74
4.2.3 Effect of Inlet Boundary Layer with Seal Cavity 75
4.2.3.1 Description of Study 75
4.2.3.2 Overall Heat Transfer Comparison 76
4.2.3.3 Heat Transfer Comparison in Life-Limiting Region 78
4.2.3.4 Effect of Inlet Boundary Layer with Cavity on Blade Life 78
5. Concluding Remarks 81
5.1 Summary and Conclusions 81
5.2 Recommendations for Future Work 83
Appendices 85
A. Literature Surveys on Grid Generation and Turbulence Modeling for High-Fidelity Heat Transfer Simulations 85
A1 Gridding Requirements and Selection of Grid Generator 85
A1.1 Literature Survey Results 87
A1.1.1 Near-Wall Grid Resolution 87
A1.1.2 Near-Wall Grid Stretching 87
A1.1.3 Overall Grid Size 90

A1.1.4 Other General Heat Transfer Grid Generation Guidelines 92
A1.2 Additional Grid Considerations for Current Study 93
A1.3 Selection of Grid Type and Grid Generator 93
A2 Turbulence Modeling Requirements and Selection of Turbulence Model 95
A2.1 Formation and Evolution of Secondary Flows 95
A2.2 Near-Wall Modeling of Turbulent Quantities 99
A2.3 Simulation of Boundary Layer Transition 103
A2.4 Applicability for Compressible Flows 109
A2.5 Conclusions Concerning Turbulence Model Selection 110
B. Equations and Constants for v2-f Turbulence Model 111
B1 Equations: 111
B2 Constants (default values): 112
C. CFD Solution Process and Case Convergence 113
D. Effect of Turbulence Intensity on Blade Heat Transfer 115
E. Calculation of Convection Boundary Conditions 119
E1 Comparison of Available Methods 119
E2 Impact of Choice of Recovery Factor Method 123
F. Adjustment of Driving Temperature for Film and Showerhead Cooling 127
F1 Trailing Edge Film Cooling 128
F2 Tip Film Cooling 129
F3 Leading Edge Showerhead Cooling 130
G. Grid Convergence Study 132
H. Additional Three-Dimensional Case Studies 135
H1 Effect of Root Fillet Geometry 135
H1.1 Description of Study 135
H1.2 Overall Heat Transfer Comparison 136
H1.3 Heat Transfer Comparison in Life-Limiting Region 139
H1.4 Effect of Root Fillet Geometry on Blade Life 140
H2 Effect of Inlet Boundary Layer Without Seal Cavity 140
H2.1 Description of Study 140
H2.2 Overall Heat Transfer Comparison 141

H2.3 Heat Transfer Comparison in Life-Limiting Region 143
H2.4 Effect of Inlet Boundary Layer without Seal Cavity on Blade Life 144

List of Figures

Figure 1.1: Industrial gas turbine inlet temperature trend in last 60 years [7] 21
Figure 1.2: Overall computational flowchart. 25
Figure 2.1: Fillet modification due to proximity of seal cavity to blade leading edge 32
Figure 2.2: Blade and endwall surface grids a) without seal cavity and b) with seal cavity .. 34
Figure 2.3: Nominal two-dimensional FLUENT grid for VKI test case. 38
Figure 2.4: Heat transfer results of benchmark studies with VKI Blade. 40
Figure 2.5: Meridional view of structural model. 41
Figure 2.6: Results of mapping operation for a) convection temperature and b) heat transfer coefficient 42
Figure 3.1: Life-limiting region in CFD comparisons. 43
Figure 3.2: Sketch of secondary flows in a typical axial turbine cascade [77] 44
Figure 3.3: Relative velocity vectors colored by non-dimensional relative total temperature on a plane of constant axial position near mid-passage showing the colder hub and cavity flow in the vortex core surrounded by hotter main gas path flow 45
Figure 3.4: Contours of non-dimensional hub heat transfer showing the high heat transfer gradients resulting from the passage vortex impingement-detachment as it migrates through the passage. 46
Figure 3.5: Comparison of three-dimensional heat transfer results 47
Figure 3.6: Effect of stronger secondary flows on near-hub suction side heat transfer 48
Figure 3.7: Heat flux contours showing effect of tip vortex on near-tip suction side heat transfer 49
Figure 3.8: Metal temperature distributions on pressure (top) and suction (bottom) side 50
Figure 3.9: Blade life distributions for three nominal blades 53
Figure 4.1: Two-dimensional, 5% span grid for Blade 1 56
Figure 4.2: Comparison of two-dimensional heat transfer results at 50% span. 59
Figure 4.3: Two-dimensional pressure distribution at 50% span. 60
Figure 4.4: Two- and three-dimensional heat transfer results in pressure side life-limiting region of Blade 1 (5% span). 61

Figure 4.5: Two- and three-dimensional heat transfer results in the suction side trailing edge region of Blade 1 62
Figure 4.6: Two- and three-dimensional near-hub heat transfer comparison 63
Figure 4.7: Suction side metal temperature distributions 64
Figure 4.8: Pressure side stress distribution 64
Figure 4.9: Pressure side strain distribution 65
Figure 4.10: Two-dimensional 50% pitch CFD domain projections showing geometry a) without and b) with seal cavity. 67
Figure 4.11: Effect of seal cavity on heat transfer 68
Figure 4.12: Heat transfer enhancing effect of seal cavity on suction side near-hub heat flux pattern 69
Figure 4.13: Metal temperature distributions on pressure (top) and suction (bottom) side.... 70
Figure 4.14: Effect of seal flow on heat transfer 72
Figure 4.15: Three-dimensional Stanton number contours showing effect of seal flow on heat transfer 73
Figure 4.16: Metal temperature distributions on pressure (top) and suction (bottom) side.... 74
Figure 4.17: Effect of inlet boundary layer with seal cavity on heat transfer 77
Figure 4.18: Heat flux contours showing effect of secondary flow impingement on suction side heat transfer 78
Figure 4.19: Metal temperature distributions on pressure (top) and suction (bottom) side.... 79
Figure A 1:Two-dimensional cross-section of typical multi-block structured grid [33]. 86
Figure A 2: Effect of streamwise grid density on Stanton number [16] 88
Figure A 3: Effect of first cell y^+ on Stanton number [16]. 88
Figure A 4: Effect of spanwise cell stretching on Stanton number [16] 89
Figure A 5: Effect of spanwise cell stretching on surface pressure coefficient [16]. 89
Figure A 6: Two-dimensional cross-section of multi-block grid used in [46] 90
Figure A 7: Effect of grid density on predicted loss coefficient contours [46]. 91
Figure A 8: Experimentally obtained horseshoe vortex rollup in vane stagnation plane [49]. 96
Figure A 9: CFD prediction of horseshoe vortex roll-up in vane stagnation plane using three different turbulence models [43] 97

Figure A 10: Effect of secondary flows on rotor suction side Stanton number distribution [43]. 98
Figure A 11: Two-dimensional heat transfer comparison between experiments and predictions with standard two-equation models, time-scale bound two-equation models, and the standard v^2-f model on a VKI blade geometry [63] 101
Figure A 12: Effect of limiting TKE production on turbulence intensity distribution [63]. 102
Figure A 13: Comparison of various turbulence model in capturing rate of increase in pitchwise-averaged endwall heat transfer [43] 104
Figure A 14: Comparison of midspan transition prediction using RKE and v^2-f turbulence models [43] 104
Figure A 15: Stanton number distribution at various spanwise locations in a transonic turbine cascade using the v^2-f model. [48] 105
Figure A 16: Heat flux distributions obtained with various turbulence models in a two-dimensional rotor simulation [56] 107
Figure A 17: Stanton number distribution obtained with the modified SST k-ω model at three spanwise locations [33] 108
Figure A 18: Stanton number distributions obtained using the SST k-ω model in its un-modified (top) and modified forms (bottom) [33]. 108
Figure A 19: Two-dimensional nozzle guide vane heat transfer distribution obtained using three different low Reynolds number k-ε models [61] 109
Figure A 20: Stanton number contours obtained from a) computations with the v^2-f turbulence model and b) experiments in transonic flow conditions [48] 110
Figure D 1: Blade locations for two-dimensional heat transfer comparison. 115
Figure D 2: Two-dimensional, near-wall turbulence intensity distributions at 50% span.... 116
Figure D 3: Effect of inlet turbulence intensity on two-dimensional, 50% span heat transfer. 118
Figure D 4: Effect of turbulence intensity on flat plate heat transfer and transition location [10]. 118
Figure D 5: Effect of freestream turbulence on calculated, 50% span, two-dimensional, suction side heat transfer. 119

Figure E 1: Two-dimensional pressure distribution with isothermal and adiabatic wall conditions at 50% span. 122
Figure E 2: Two-dimensional heat transfer coefficient comparison using Recovery Factor Method and 2-Calculation Method at 50% span..... 123
Figure E 3: Comparison of actual adiabatic wall temperature and that estimated using the Recovery Factor Method..... 126
Figure F 1: Trailing edge pressure side near-tip film cooling configuration..... 128
Figure F 2: Single hole angled injection, flat plate film cooling effectiveness distribution as a function of pitchwise distance from center of cooling hole [72]..... 129
Figure F 3: Tip crown and internal cooling passage outlets..... 130
Figure F 4: Leading edge showerhead cooling configuration. 131
Figure F 5: Showerhead film cooling effectiveness distribution..... 132
Figure F 6: Heat transfer driving temperature 132
Figure G 1: Blade 1 suction side heat transfer coefficient with nominal (top) and refined (bottom) grid. 133
Figure G 2: Three-dimensional heat transfer results on nominal and refined grid..... 134
Figure H 1: Fillet geometries (on suction side) compared for effect on heat transfer and life 136
Figure H 2: Actual Blade 1 fillet geometry. 137
Figure H 3: Straight fillet configuration used in nominal calculations..... 137
Figure H 4: Effect of root fillet on heat transfer 138
Figure H 5: Three-dimensional suction side heat flux patterns for various fillet geometries139
Figure H 6: Effect of inlet boundary layers without seal cavity on heat transfer 142
Figure H 7: Three-dimensional heat flux contours showing impact of flow impingement on suction side heat transfer..... 143
Figure H 8: Three-dimensional heat flux contours showing impact of flow impingement on near-tip suction side heat transfer 143
Figure H 9: Metal temperature distributions on pressure (top) and suction (bottom) side... 145

List of Tables

Table 1.1: Design parameters at hub, mean, and tip sections for three blade geometries. 24
Table 2.1: Area-averaged and maximum values of y^+ for three-dimensional calculation on Blade 1 with seal cavity. 34
Table 2.2: Pressure and temperature boundary conditions for stator and rotor main gas path. 35
Table 2.3: Midspan aerothermal parameters for VKI and nominal MHI cases. 38
Table 2.4: Area-averaged y^+ values for FLUENT VKI benchmark cases. 39
Table 3.1: Leading edge peak heat transfer differences from nominal 46
Table 3.2: Noise parameter variability used in the probabilistic thermal-structural analyses 51
Table 3.3: Deterministic, mean, and standard deviation of blade life for three nominal blades .. 52
Table 3.4: Blade life correlation coefficients for three nominal blades. 53
Table 4.1: Summary of life impact of various modeling approximations. 55
Table 4.2: Effect of seal cavity on leading edge peak heat transfer. 67
Table 4.3: Effect of seal flow on leading edge peak heat transfer. 72
Table 4.4: Effect of inlet boundary layer with seal cavity on leading edge heat peak transfer. ... 76
Table A 1: Grid characteristics in grid convergence study [16] 88
Table A 2: Grid point distribution used in [46]. 90
Table A 3: Leading edge horseshoe vortex roll-up comparison using two RKE models and one v^2-f turbulence model. 98
Table C 1: Three-dimensional CFD wheel speed and Courant number schedule. 113
Table D 1: Trends in quantities monitored for interpretation of two-dimensional heat transfer results. 117
Table E 1: Heat flux errors (in percent) incurred in using the Recovery Factor Method versus the 2-Calculation Method to provide boundary conditions to the thermal-structural analyses. 127
Table H 1: Effect of root fillet geometry on results of thermal-structural calculations. 140
Table H 2: Effect of inlet boundary layer without seal cavity on leading edge peak heat transfer. 141

Nomenclature

Symbols

ARC	distance along airfoil surface from stagnation point to trailing edge
c	chord
c_p	specific heat at constant pressure
C_p	coefficient of pressure
f	relaxation function in v^2-f model
F	blowing ratio, $u_c\rho_c/u_g\rho_g$
h	local specific enthalpy
I	momentum ratio, $u_c^2\rho_c/u_g^2\rho_g$
k	turbulent kinetic energy
K	acceleration parameter,
M	Mach Number
P	pressure, TKE production
P_r	Prandtl number
q	heat flux
r	recovery factor
R	gas constant
s	span
S_t	Stanton number
T	temperature, time scale
Tu	turbulence intensity
u	velocity component
U	velocity magnitude
v^2	turbulent velocity component normal to mean velocity direction in v^2-f model
y^+	non-dimensional wall distance

Greek

ε	turbulence dissipation rate

γ	ratio of specific heats
μ	viscosity
ω	specific turbulence dissipation rate
T	specific turbulence dissipation rate
ρ	density
τ	shear stress

Subscripts

aw	adiabatic wall condition
cas	casing location
e	edge of boundary layer
hub	hub location
is	isentropic condition
n	normal to the wall
ref	reference quantity
t	turbulence quantity
T	total quantity
w	wall condition

Abbreviations

CAD	Computer-Aided Design
CFD	Computational Fluid Dynamics
DNS	Direct Numerical Simulation
LES	Large Eddy Simulation
LEWA	Leading Edge Wedge Angle
MHI	Mitsubishi Heavy Industries, Ltd.
OEM	Original Equipment Manufacturer
RFM	Recovery Factor Method
RKE	Realizable k-ε model

RLE	Leading Edge Radius
RNG	Renormalization Group
RTE	Trailing Edge Radius
TBC	Thermal Barrier Coating
TEWA	Trailing Edge Wedge Angle
TKE	Turbulent Kinetic Energy
WF	Wall Functions

1. Introduction

1.1 Motivation and Background

In the gas turbine industry, engine manufacturers continue to strive for higher hot-section temperatures in pursuit of the associated power density and cycle efficiency benefits. As seen in Figure 1.1, gas turbine inlet temperatures have been increasing since the machine's invention in the early part of the last century. Today, power generation turbine inlet temperatures exceed 1500°C [1]. To achieve such high temperatures, a careful compromise of the conflicting requirements of low cost, durability, and high performance must be struck. In the competitive power generation sector, engine availability is crucial and component durability and cost remain primary concerns for both manufacturer and operator.

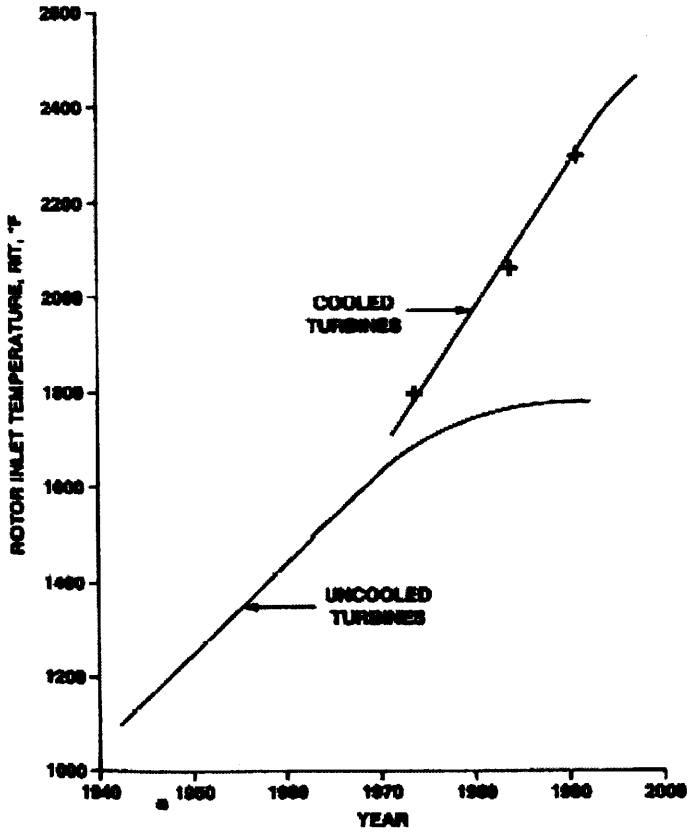

Figure 1.1: Industrial gas turbine inlet temperature trend in last 60 years [7]

The impact of structural loads on turbine blades is exacerbated by the corrosive, high temperature environment in which the blades operate. Failure mechanisms include creep, surface corrosion, low and high cycle fatigue, and surface oxidation [87]. A single blade failure can lead to costly engine stoppages and maintenance.

There have been few efforts made to establish an explicit connection between aerothermal modeling and turbine blade life. Some studies focused on the impact of geometric modifications to blade leading edges [74, 91] and film cooling configurations [18, 26, 31, 32, 41, 69, 82] on losses and heat transfer. Others focused on the heat transfer impact of inlet quantities (incidence angle, Reynolds number, turbulence intensity) and profiles [17, 35, 44, 45, 61, 68, 85] as well as internal cooling passage and rib geometry [70, 71, 83, 84, 86]. Still, others combined the problems of internal and external cooling in conjugate heat transfer analyses [12-15, 39, 50, 51, 58, 81, 90]. However, in the majority of these studies, high heat transfer areas were, by default, assumed to have a detrimental impact on life without further analysis.

One of the challenges associated with establishing such a turbine aero-to-life connection is the multidisciplinary nature of the analyses required. This thesis will focus on the first half of these analyses, the external aerothermodynamics. In a parallel study [53], the thermal-structural problem within the blade material will be solved and the results used to estimate life. The goal of the thesis is the enhancement of the aero-to-life connection with focus on the impact of typical geometric and flow features found in the high pressure turbine.

1.2 Problem Statement

In-depth blade life estimation takes place in the design stages in which most geometric features have already been fixed [2]. This renders design iterations based on durability very costly. Methods are thus sought to allow designers to take into account blade durability at earlier stages. To develop these methods, the links between geometric and flow features in high-fidelity aerothermal modeling and blade life must be better understood leading to the construction of simple durability models suitable for use in the preliminary stages of design.

1.3 Objectives

The first objective of this thesis is the establishment of aerothermal modeling requirements for the end-to-end calculation of blade life starting from upstream aerothermal boundary conditions. In addition to surveying current best-practices for grid generation and turbulence modeling for the accurate estimation of turbine blade heat transfer, the impact of various fluid dynamic and geometric modeling approximations on the blade heat transfer and life are quantified.

A second objective is the assessment of the impact of blade design changes on deterministic blade life and on the robustness of blade life to variability. Also, the impact of external heat transfer variability on blade life variability is quantified and compared to the impact of other sources of variability.

1.4 Overall Approach

The overall project has two parallel studies, one dealing with the external aerothermodynamics and one dealing with the internal thermal-structural problem leading to the estimation of life. The first is the subject of this thesis, while the second is the subject of [53]. Specifically, CFD calculations were used to provide external thermal boundary conditions to an FEM thermal-structural analysis. To investigate the impact of blade design on life, and robustness, three different first stage rotor blade geometries were considered (all provided by MHI). The blades were constructed to span a representative portion of the allowable design space while satisfying a minimum work requirement. Table 1.1 lists the design variables for the three blades, relative to the baseline design (Blade 1).

Although ideally, a thermal solution would be done employing a conjugate heat transfer method including film cooling, the computational expense, in terms of grid generation and solution convergence, of such an approach was deemed impractical for the purposes of this project. Rather, the external heat transfer problem was solved using CFD simulations without film cooling and assuming isothermal solid surfaces. External convection boundary conditions were constructed from these results and the effect of film and showerhead cooling incorporated into

the thermal boundary conditions as corrections to the heat transfer driving temperature. The methods used to generate the convection boundary conditions and to account for the effects of film and showerhead cooling are described in Appendices E and F. The external boundary conditions (both thermal and pressure loads) were then applied to the solid model. The external conditions, combined with internal convection boundary conditions and structural loads imposed by the rotating disc formed a complete set of boundary conditions for the FEM analysis [53]. The FEM calculations were used to estimate the turbine blade life taking into account the MHI loading cycle and the effects of creep and low cycle fatigue.

Blade Number		1	2	3
Pitch/Chord	hub	0.8	0.7	0.9
	mean	1.0	0.9	1.1
	tip	1.1	1.0	1.2
Max Thickness Ratio	hub	1	0.9	1.1
	mean	1	0.9	1.1
	tip	1	0.9	1.1
RLE Ratio	hub	1	1.1	0.9
	mean	1	1.1	0.9
	tip	1	1.1	0.9
RTE Ratio	hub	1	1.1	0.9
	mean	1	1.1	0.9
	tip	1	1.1	1.0
LEWA Ratio	hub	1	1.1	0.9
	mean	1	1.1	0.9
	tip	1	1.1	0.9
TEWA Ratio	hub	1	1.1	0.9
	mean	1	1.1	0.9
	tip	1	1.1	0.9

Table 1.1: Design parameters at hub, mean, and tip sections for three blade geometries.

One project goal was the identification of differences in blade life variability among the three blades in the presence of typical "noise parameters". These noise parameters were meant to represent quantities not explicitly controlled by the designer or subject to variability through tolerancing. The noise parameters chosen for this study were

- External heat transfer coefficient
- External flow temperature
- Internal heat transfer coefficient
- Internal flow temperature

- Thermal barrier coating thermal conductivity
- Thermal barrier coating thickness
- Metal thermal conductivity

The mean values for the internal convection and structural parameters can be found in [53]. For the external convection conditions, the mean values were assumed to be those obtained from the CFD calculations. Designs exhibiting decreased life variability with these noise parameters are deemed more robust to variation, and would point at an area of the design space to be exploited in future designs.

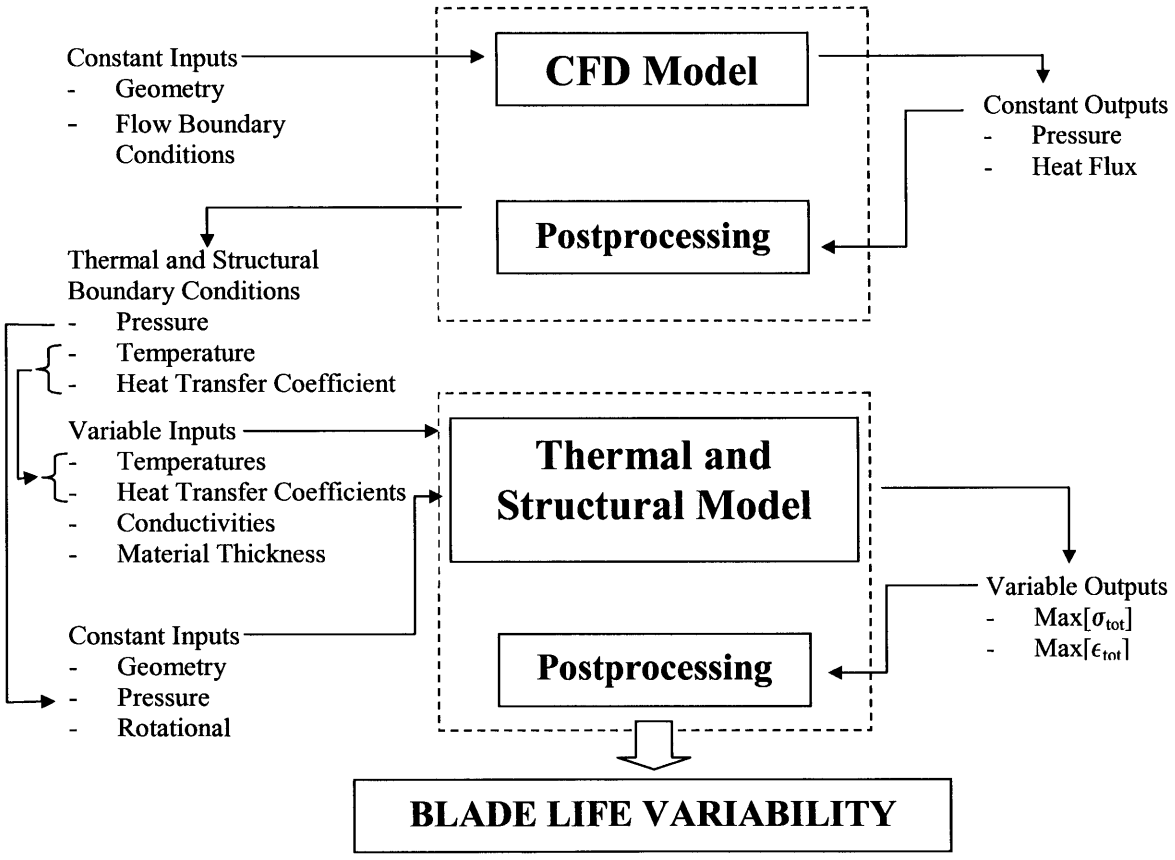

Figure 1.2: Overall computational flowchart.

A computational flowchart is provided in Figure 1.2 of the input-output relationships and the steps taken to pass from aerothermal analyses to blade life variability. In the deterministic calculations, the variable inputs were kept constant at their nominal values and a single life estimate was obtained.

1.5 Outline of Thesis

The thesis is organized as follows. The computational setup is described in Chapter 2 beginning with a summary of a literature survey on grid generation for high-fidelity heat transfer simulations. This is followed by a description of the chosen flow solver and a summary of a literature survey on turbulence modeling for high-fidelity heat transfer simulations. Section 2.5 provides computational results used in validating the combination of grid topology and resolution, flow solver, and turbulence model. The chapter is concluded with a brief description of the mapping process from CFD to FEM and the approach used in the calculation of life.

The results of three-dimensional CFD analyses are described in Chapter 3. First, the flow features governing the heat transfer patterns on the blades are identified. Second, the results obtained for the three geometries are compared to point out the drivers responsible for observed differences. Next the deterministic life results for the three geometries are presented and the impact of external thermal conditions discussed. The chapter is concluded with the presentation of probabilistic life estimates for the three blades and a discussion regarding the impact of external thermal conditions on blade life variability.

Chapter 4 deals with the impact of modeling approximations and geometric and flow features on blade life estimation. First, heat transfer results of two-dimensional CFD analyses on the three geometries at four spanwise locations are presented and compared against results obtained from three-dimensional calculations. The two-dimensional results are then used to generate three-dimensional thermal boundary conditions and the life estimates obtained from this simplified CFD data and that based on three-dimensional CFD data compared. Next, the impact of rotor-stator interface seal cavity, seal flow, and inlet boundary layers on blade heat transfer and life is presented through a series of aero-to-life case studies on the Blade 1 geometry.

A summary and conclusions are provided in Chapter 5 along with recommendations for future work.

Several appendices supplementing the content of the thesis follow Chapter 5. The first consists of two literature surveys on grid generation and turbulence modeling for high-fidelity heat transfer simulations and identifies the chosen approaches for both. The equations and constants employed in the v^2-f turbulence model are listed in Appendix B. The CFD solution process and convergence criteria are outlined in Appendix C. Appendix D presents results of analyses used to confirm the observed effect of turbulence intensity on heat transfer in two-dimensional preliminary calculations. Appendix E describes the method used to calculate the convection boundary conditions along with an estimate of its accuracy relative to a more computationally expensive method. The approach used to account for film and showerhead cooling in the CFD results is described in Appendix F. The results of a grid convergence study are presented in Appendix G. Appendix H describes the impact of root fillet geometry and inlet boundary layers without seal cavity on blade heat transfer and life.

1.6 Contributions

The contributions of the thesis are:

- The establishment of the first half of a framework for the end-to-end aero-to-life analysis of turbine blades.

- The assessment of the life impact of typical high pressure turbine geometric and flow features for use in the construction of simplified durability models.

- An assessment of the role of external aerothermodynamics on the estimation of turbine blade life and its variability.

2. Computational Modeling Approach

2.1 Grid Generation for High-Fidelity Heat Transfer Simulations

A literature survey was conducted to identify the grid characteristics for high fidelity heat transfer simulations in turbine geometries. The full survey can be found in Appendix A1. Summarizing the survey, a general guideline for the generation of high-fidelity heat transfer grids was defined.

- A first cell non-dimensional wall distance (y^+) on the order of unity should be used [21, 33, 43, 48, 61, 73].
- Given a maximum first cell non-dimensional wall distance ($y^+_{max} < 2$), a low near-wall cell stretching ratio is better than a reduced first cell y^+ value [46].
- Grid cell stretching values, especially in the high-gradient viscous regions, should be kept between roughly 0.8 and 1.25 to ensure grid smoothness and numerical capture of near-wall gradients [16, 33, 65].
- Grids intended for heat transfer simulations should have on the order of 25-40 grid points within the boundary layers [56].
- 50-100 grid points in the spanwise direction are recommended for half-span simulations intended to accurately represent vortex cores and secondary flows [27, 46].
- Full span grids at least 1 to 2 million cells per blade row should be used for high-fidelity simulation of secondary flow and heat transfer [23, 34, 46, 65].
- In addition to grid resolution and smoothness, grid cell orthogonality (low cell skewness), particularly in the high cell aspect ratio near-wall regions, should be considered because it accelerates solution convergence [46, 65].

The results of the survey, combined with a need for minimal grid generation times and high grid reusability were considered during the comparison of three grid generation packages (GridPro[1],

[1] GridPro, Program Development Company LLC, 300 Hamilton Avenue, Suite 409, White Plains, NY 10601

Gridgen®[2], and TrueGrid®[3]). All three were capable of generating high-quality multi-block structured grids consistent with the requirements found in the literature. However, the level of automation and grid reusability provided by the topology-based approach used in the GridPro grid generator was determined to best satisfy the needs of the project.

2.2 Flow Solver

The commercial package FLUENT 6[4] was used for the CFD analyses. It is an unstructured, finite volume, pressure-based code capable of simulating compressible flows with heat transfer. The choice was based on flexibility with regard to grid types, options for turbulence modeling, as well as level of maturity in the research and industrial sectors. The code can handle unstructured, hybrid, and structured grids providing considerable freedom in the grid generation process. FLUENT 6 also provides a number of choices for turbulence modeling ranging from the 1-equation Spalart-Almaras model to Reynolds Stress Modeling. Details of the code can be found in [5].

2.3 Turbulence Modeling for High-Fidelity Heat Transfer Simulations

A literature survey, located in Appendix A2, was conducted to determine a suitable approach for the modeling of turbulence in the turbine environment. The four-equation v^2-f model (see Appendix B) was chosen as best satisfying the needs of the project.

During the survey, the v^2-f model was compared against several variants of the two-equation k-ε and k-ω models. Due to their added computational cost and the fact that they have not yet been shown to be a consistently superior approach, Reynolds Stress Models were not considered in the comparison. Similarly DNS and LES did not constitute valid alternatives due to their prohibitively high demand on computational resources. Most of the models compared were

---

[2] Gridgen®, Pointwise, Inc., 213 S. Jennings Ave., Fort Worth, Texas 76104-1107
[3] TrueGrid®, XYZ Scientific Applications, Inc., 1324 Concannon Blvd., Livermore, CA 94550
[4] FLUENT 6, Fluent, Inc., 10 Cavendish Court, Centerra Park Lebanon, New Hampshire 03766.

either directly available in FLUENT 6 or could be implemented using User-Defined Functions [5].

In the literature consulted, the v^2-f model was shown to be generally superior to the other RANS-based models in capturing the relevant flow phenomena including formation and evolution of secondary flow structures in regions susceptible to low durability, near-wall anisotropic behavior of turbulence quantities and their relation to heat transfer coefficient distributions, and boundary layer transition. Its applicability for compressible flows was demonstrated by its capability to describe heat transfer and boundary layer transition in transonic simulations [48, 63]. The v^2-f model, as implemented in FLUENT 6, was therefore chosen for turbulence modeling in this project.

2.4 CFD Case Setup

This section deals with the inputs to the CFD calculations. The section begins with a description of the computational grids, followed by a discussion regarding boundary conditions.

2.4.1 Computational Grids

As described in Section 1.4, the three blade geometries were provided by MHI and were designed to satisfy a minimum work requirement. At the time of grid generation, no CAD data was available for the blade and seal cavity geometries. Rather, coordinates at 13 spanwise sections (not taking into account the root fillet), a stacking location, dimensions for the tip clearance (1.94% of rotor inlet span) and root fillet radius (5.8% of rotor inlet span) were provided for the blades and a scaled cross-sectional schematic of the MHI stage was provided to help model the cavity geometry. The inlet and outlet axial locations and endwall geometry were also provided in the cross-sectional schematic. The same endwall, seal cavity, tip clearance, and root fillet geometry and dimensions were used in all three blade models.

The spanwise blade coordinates were used to generate the blade shapes using surface splines. The round fillet in the actual MHI geometry was not replicated. Rather, following the generation

of the basic blade shapes, a 45° wedge of side equal to the fillet radius was added at the base of the blades creating a straight fillet at the interface with the contoured hub. The straight fillet arrangement was designated as the nominal configuration and was used for the three blades considered in this thesis and most of the case studies presented in Chapter 4. Due to the proximity of the cavity to the blade leading edge, the fillet geometry was modified in this region. The 5.8% span height of the fillet was maintained but the fillet pitch was reduced to accommodate the cavity. Figure 2.1 a) shows the fillet geometry at the leading edge near the cavity where the fillet pitch has been reduced to zero. Part b) of the same figure shows the fillet at the suction side shoulder where the full pitch of the fillet was used. All geometry files for all stage surfaces (blade, fillet, endwalls, tip, cavity) and construction surfaces used for grid control were generated in MATLAB[5] and exported in GridPro-compatible format.

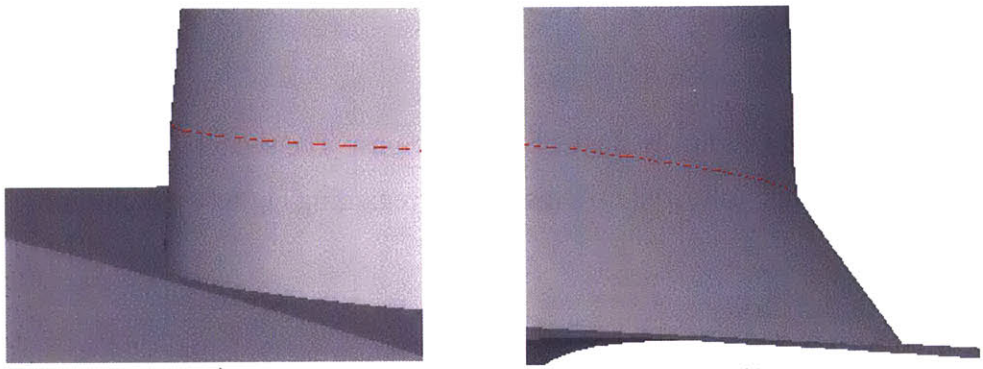

Figure 2.1: Fillet modification due to proximity of seal cavity to blade leading edge: a) fillet geometry at leading edge, b) fillet geometry at suction side shoulder. The red line represents the height of the fillet.

GridPro grids are generated in three steps. First, a multi-block grid topology is created based on the surfaces and volumes requiring meshing. The grid topology generation step is by far the most costly in terms of human effort. Special topology creation techniques for grid control and cell count management were employed in the tip, near-hub, and leading and trailing edge regions of the blade. The majority of these techniques are described in the GridPro tutorial exercises and result in good grid resolution in areas of interest while reducing grid density in regions of less importance. Following the topology creation, specific portions of the resulting lattice of points and edges are assigned to the computational domain's surfaces. These surface assignments,

[5] MATLAB®, The Mathworks, Inc., 3 Apple Hill Drive, Natick MA 01760-2098

combined with the option of interactive user-specified grid density allow the user to control the grid during the iterative smoothing process in the second phase of grid generation. Several versions of a grid template were designed and tested on the nominal geometry until a suitable candidate was obtained.

Once the topology is assigned to the appropriate surfaces, an Euler grid is generated throughout the computational volume. The grid is so called because it does not yet include near-wall refinement such as would be needed in a Navier-Stokes analysis. The reader is referred to the GridPro user's guide [3] and GUI reference manual [4] for a description of the topology generation rules and strategies.

The final step in the grid generation process is called grid clustering and is conducted in regions where near-wall gradients are to be captured. For the three-dimensional grids, grid clustering was employed on the blade, blade tip, and both endwalls (including cavity). Grid clustering is controlled by specifying the size of the first cell off the wall of interest and a growth ratio defined as the ratio of one cell's size to that of its neighbor closer to the wall being clustered. During clustering, the GridPro code attempts to respect these two specifications over all of the chosen surfaces. Complex geometries and large variations in Euler grid off-wall cell growth result in more or less off-wall stretching than desired in the clustering process. However, the growth ratio obtained in the final grid can easily be verified and the clustering reinitiated with modified parameters if not within acceptable limits.

A first cell grid size expected to yield y^+ values near unity was used in all grids. Iterations of grid clustering were conducted until the worst off-wall grid stretching in the first 10 cells was less than 1.3 on all clustered walls. Grids for the three blades were generated using the same 1324-block, 1.5 million-cell grid template. A second grid template, without seal cavity, made up of 560 blocks and 0.8 million cells was created for use in several case studies conducted on Blade 1 and discussed in Chapter 4. Blade and endwall surface grids from each template are shown in Figure 2.2. Table 2.1 lists area-averaged and maximum values of first cell y^+ values obtained following solution convergence on the Blade 1 grid with seal cavity.

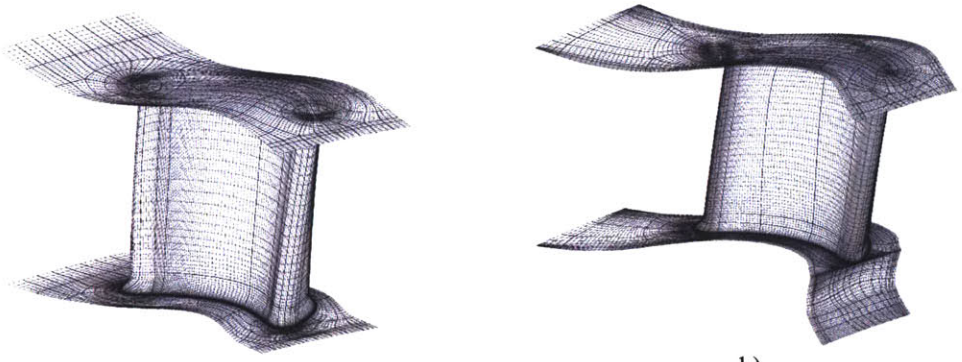

a) b)

Figure 2.2: Blade and endwall surface grids a) without seal cavity and b) with seal cavity

Surface	Average y^+	Maximum y^+
Blade	0.625	1.601
Casing	0.968	2.408
Hub	0.848	1.307
Tip	0.638	1.192

Table 2.1: Area-averaged and maximum values of y^+ for three-dimensional calculation on Blade 1 with seal cavity.

2.4.2 Boundary Conditions

Boundary conditions for three-dimensional stator and rotor simulations were supplied by MHI in the form of total pressure, total temperature, relative inlet flow angle, and outlet pressure values at 0%, 25%, 50%, 75%, and 100% span. The pressure and temperature conditions are listed in Table 2.2, in non-dimensionalized format. For the rotor simulations, 10 000 rpm was used for the wheel speed. Throughout this thesis, all quantities pertaining to the MHI calculations will be non-dimensionalized by mass-averaged stator inlet quantities. In the case of pressure and temperature, the averaged total quantities will be used. The non-dimensionalizing quantity for heat flux plots will be,

$$\overline{\rho}\overline{V}c_p\overline{T}_T$$

and for heat transfer coefficient, the product,

$$\overline{\rho}\overline{V}c_p$$

will be used to form what will be referred to as Stanton number plots. The reader is referred to the nomenclature at the beginning of the thesis for a description of the symbols used in this thesis. Unless otherwise stated, length scales will be non-dimensionalized by the stator inlet span.

Imposing radial equilibrium, axisymmetric profiles for the absolute flow angle were generated by ensuring mass flow matching with that specified by MHI. No inlet boundary layers were included in the nominal profiles.

Geometry	Spanwise Location (%)	$P_T/P_{Tvane\text{-}inlet}$	$T_T/T_{Tvane\text{-}inlet}$	$P/P_{Tvane\text{-}inlet}$
Stator	0	1.0	0.905	0.624
	25	1.0	1.002	0.641
	50	1.0	1.038	0.655
	75	1.0	1.022	0.667
	100	1.0	0.932	0.676
Rotor	0	0.970	0.877	0.435
	25	0.972	0.962	0.433
	50	0.973	0.992	0.433
	75	0.974	0.969	0.432
	100	0.975	0.883	0.432

Table 2.2: Pressure and temperature boundary conditions for stator and rotor main gas path.

Turbulence conditions were not provided by MHI. To determine a consistent set of rotor inlet turbulence quantities, calculations were conducted on the stator vane upstream of the MHI rotor. A value of 10% for the inlet turbulence intensity to the stator was determined to be consistent with the literature [36, 37, 54, 57, 68]. The turbulent length scale was taken as a fraction of the inlet hydraulic diameter,

$$l = KD_H \qquad \text{E 2.1}$$

in which a factor K, of 0.07 was used as suggested in [5]. The stator vane calculation results were then used to generate inlet turbulence quantities for the rotor. Mass-averaged values of

velocity, turbulent kinetic energy (TKE), k, and TKE dissipation rate, ε, were used to construct the turbulence intensity and length scale at the inlet to the rotor as in [5],

$$Tu = \frac{\sqrt{2/3\,\bar{k}}}{\|\bar{U}\|} \qquad \text{E 2.2}$$

$$l = \frac{C_\mu^{3/4}\bar{k}^{3/2}}{\bar{\varepsilon}} \qquad \text{E 2.3}$$

The resulting turbulence intensity, in the absolute frame, was 2.35% and the length scale 0.43% of the stator inlet span. To assess the impact of the choice of inlet turbulence to the stator, an additional stator calculation was conducted using an inlet turbulence intensity of 20% with the same turbulent length scale. This doubling of inlet turbulence intensity resulted in less than twice the level of exit turbulence intensity, 3.66% compared with 2.35% but more than twice the turbulent length scale, 1.0% compared with 0.43% of the stator inlet span. Given that 10% for the stator inlet turbulence intensity was found to be in agreement with the literature and that no turbulence information was available for the rotor inlet, consistency from stator to rotor was given priority over attempting to guess the actual values at the rotor inlet. An inlet turbulence intensity level of 2.35% was thus used for the rotor simulations.

The impact of turbulent length scale was not investigated extensively in this project. However, two-dimensional calculations performed on the midspan Blade 1 geometry showed the primary effect of increasing the non-dimensional turbulent length scale from 0.43% to 1.0% was to increase the heat transfer in the leading edge region. Specifically, stagnation point heat transfer was increased by 12%, and near leading edge suction and pressure side heat transfer were increased by 18% and 10% respectively. As will be shown later, in this project, the leading edge was not a low-durability area. The heat transfer differences in what will be shown to be the life-limiting region (trailing edge) were less than 6% on the pressure side and less than 2% on the suction side. The turbulent length scale of 0.43% obtained from the stator calculation at 10% inlet turbulence intensity was thus used for the remainder of the calculations.

Mass flow, total pressure, and total temperature at the seal cavity inlet were also provided by MHI. For lack of better information, a value of 5% for the turbulence intensity (E 2.2) was chosen for the seal cavity inlet. As in (E 2.1), the length scale was estimated as a fraction of the hydraulic diameter.

In FLUENT, pressure inlet and pressure outlet boundary conditions were used at the main gas path inlet and outlet respectively. Mass-flow inlet boundary conditions were used at the seal cavity inlet. Periodic conditions (no interpolation) were used at the mid-passage interface of what would be the edge of the next computational volume.

The walls were modeled as no-slip and isothermal at a non-dimensional temperature of 0.68. Film and showerhead cooling, although present in the actual MHI blade, were not taken into account in the CFD calculations but were included afterwards during the generation of external convection boundary conditions for the thermal-structural calculations (see Appendix F).

The CFD solution process and methods used to determine case convergence are described in Appendix C.

2.5 Validation of Computational Setup

Benchmark studies were performed on the VKI high-pressure turbine blade geometry used in [18-20, 22, 63]. As shown in Table 2.3, most of the aerothermal parameters in the test case were consistent with those of the midspan MHI blades.

The study included both experimental and computational results. The experiments were conducted using a linear 6-blade cascade. The instrumented blade was constructed of "Macor" glass ceramic while the others were aluminum. 45 platinum thin films were painted on the instrumented blade's surface and used as variable resistance thermometers in the short-duration tests. A film temperature/wall heat flux conversion was obtained from an electrical analogy, simulating conduction in a semi-infinite body as explained in [60, 76]. Additional details concerning the experimental setup are given in [18-20, 22]. The blade geometry, including

	VKI	MHI
$Re_{c,in}$	$8.5x10^5$	$3.73x10^5$
M_{in}	0.25	0.29
M_{ex}	0.92	0.86
Tu_{inlet}[6]	5%	6.3%
T_w/T_t	0.728	0.684

Table 2.3: Midspan aerothermal parameters for VKI and nominal MHI cases.

coordinates, can be found in [22]. These coordinates were used to generate two-dimensional computational grids to be used in FLUENT, see Figure 2.3, as well as with the MIT-developed MISES computational package [24]. MISES is a collection of programs which perform grid

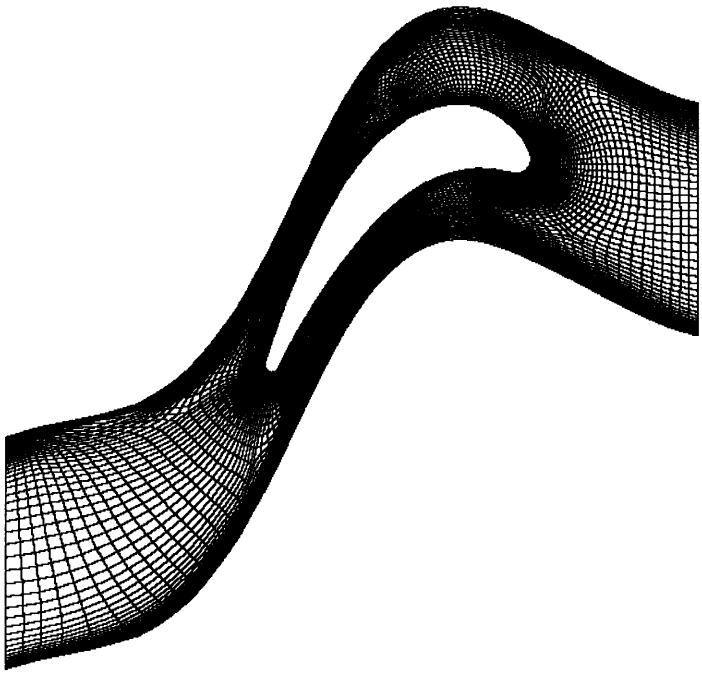

Figure 2.3: Nominal two-dimensional FLUENT grid for VKI test case.

generation and initialization and quasi-three-dimensional streamline curvature flow analysis using an Euler solver in the freestream region and a two-dimensional integral boundary layer routine in the near-wall viscous regions. The version of the code used in this thesis can be used

[6] Here the turbulence intensity for the MHI case is stated in the relative frame. The turbulent kinetic energy is therefore non-dimensionalized by the inlet relative velocity. This formulation is used to make the comparison between the MHI cases and the stationary cascade experiments consistent.

to predict heat transfer to the blade surface based on the analogy between heat transfer and surface friction. A modified version of the Abu-Ghannam-Shaw (AGS) bypass transition model and an e^n, exponential growth natural transition model are used simultaneously to determine the transition location. Either model can be decisive in inducing transition. Since the VKI cases were two-dimensional cascades, the streamline curvature capability of the code was not used here. Additional details concerning the capabilities and uses of MISES can be found in [25].

The aerothermal boundary conditions of [63] were used in both the FLUENT and MISES cases. For the FLUENT cases, the grids were generated so as to yield first cell y^+ values on the order of unity. Area-averaged first cell y^+ values obtained following solution convergence are shown in Table 2.4.

Turbulence Model	**Area-Averaged y^+**
v^2-f	0.4494
2-layer k-ε	0.4894

Table 2.4: Area-averaged y^+ values for FLUENT VKI benchmark cases.

In [63], the results are plotted as heat transfer coefficient vs. non-dimensional surface distance. The heat transfer coefficient is calculated as

$$h = \frac{q}{(T_w - T_T)} \qquad \text{E 2.4}$$

where q is the inferred heat flux from the thin film temperature measurements, T_w the known uniform surface temperature at the start of the short-duration experiment, and T_T, the freestream total temperature.

The experimental and computational results of [63], as well as the results of a MISES and two FLUENT calculations are presented in Figure 2.4. The results from [63] were taken directly from the figure in the reference. In Figure 2.4, on the suction side, MISES estimates transition abruptly and does not recover to the experimental values. On the pressure side, MISES over-

estimates in the trailing edge region where flow acceleration typically has an attenuating effect on heat transfer. The standard 2-layer version of the k-ε model (SKE) does a good job on the pressure side near the leading edge but over-estimates by about 60% near the pressure side trailing edge. On the suction side, the values of heat transfer are clearly over-estimated. Medic and Durbin's v^2-f model is shown to capture both the trends and actual values of heat transfer over the majority of the blade surface [63].

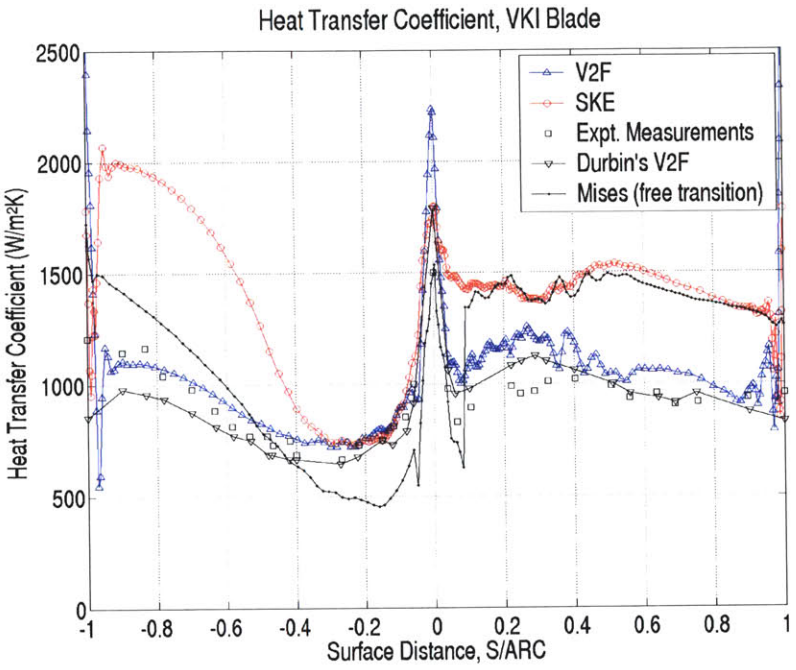

Figure 2.4: Heat transfer results of benchmark studies with VKI Blade.

The v^2-f model used in this thesis does a good job of matching the experiments everywhere but in the leading edge region. Since the heat transfer estimations quickly recover close to the leading edge, this discrepancy was not considered to be a drawback.

Given the similarity between the MHI and VKI cases and the results described above, the combination of flow solver (FLUENT), turbulence model (v^2-f) and grid type was computationally validated for our intended use. The convention used in Figure 2.4 regarding non-dimensional surface distance will be employed throughout the remainder of this thesis with negative values representing the pressure side and positive values, the suction side of the blade.

2.6 Estimation of Life

In Chapters 3 and 4, the results of CFD calculations are used as part of the boundary conditions in the FEM thermal-structural simulations. Before proceeding, a description of the approach used in transferring the CFD-generated boundary conditions to the FEM model and a brief overview of the thermal-structural analyses is appropriate.

Since the CFD and FEM models did not employ the same grid at the blade's external surface the CFD-generated convection conditions were mapped, within ANSYS, onto the blade surface of the structural model shown in Figure 2.5[7]. The shank was not modeled in its entirety. Rather, it was cut above the anchoring location to the turbine disc and a no-displacement boundary condition imposed at the cut surface.

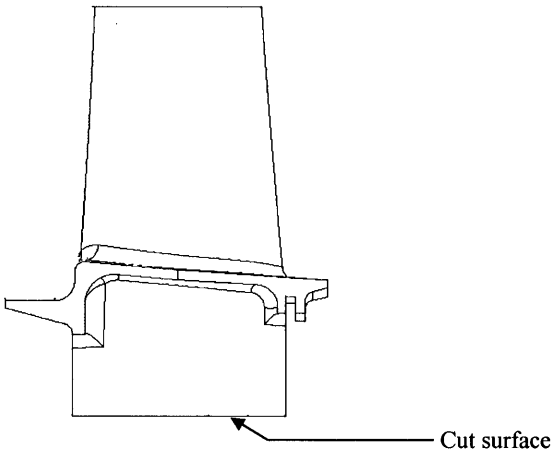

Figure 2.5: Meridional view of structural model.

Despite the necessarily coarser structural grid, the mapping operation captured the major features observed in the CFD calculations as seen in Figure 2.6. In highly curved regions such as the leading edge, lower mapping fidelity was obtained due to differences in the two models' geometries resulting from their different origin (CAD data for FEM and blade section coordinates for CFD) and the differing levels of resolution between the two grids. In the tip

[7] Due to hub and fillet geometry differences, the automated mapping in this region resulted in poor transferability of CFD trends. The mapping in this region was therefore done manually.

region, only the heat transfer coefficient obtained from the CFD calculations was used. The heat transfer driving temperature was modified as outlined in Appendix F to take into account the actual tip geometry and coolant exit effect on tip heat transfer. The internal passage convection boundary conditions were provided by MHI.

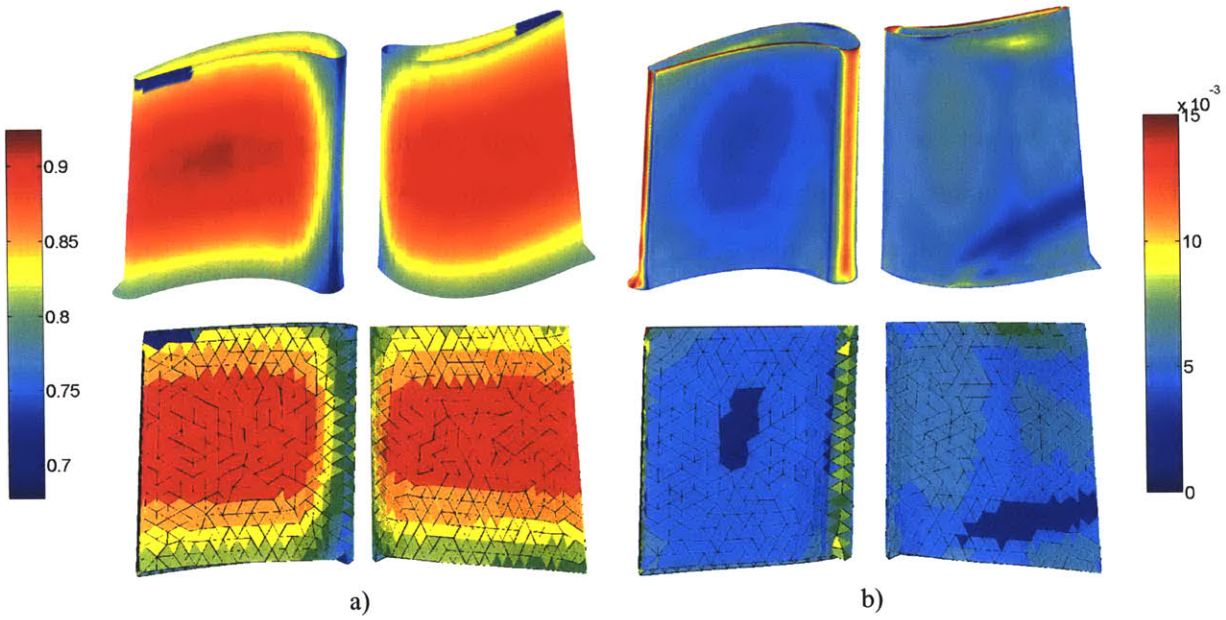

Figure 2.6: Results of mapping operation for a) convection temperature and b) heat transfer coefficient: CFD results (top) vs. FEM mapping results (bottom).[8]

To render the comparison of the blades useful from a designer standpoint, the internal convection conditions, provided for Blade 1 only, were scaled for Blades 2 and 3 so as to ensure identical deterministic maximum metal temperature for all three blades.

In the determination of blade life, equivalent stress and strain values in a volume surrounding the life-limiting location were extracted and averaged. The averaged quantities were then used to account for the effects of low cycle fatigue and creep, two important life-limiting mechanisms in industrial gas turbines [87]. The motivation and computational details of this approach to life estimation and the choice of volume for the stress and strain averaging are described in [53].

---

[8] Note that the colors in the heat transfer coefficient plots are not exactly the same in the CFD plots as in the ANSYS plots. Due to the wide range of heat transfer coefficients, in order to show the trends were captured using the limited color range available in ANSYS, a reduced scale had to be used for these plots. The magnitudes were nevertheless in good agreement.

3. Impact of Blade Design on Heat Transfer and Life

This chapter presents the results of three-dimensional CFD simulations on the three blade geometries. The flow features driving the heat transfer patterns are described first. A detailed description of the heat transfer differences observed between the three blades is then given with focus in the life-limiting region. The life-limiting region, identified based on the first structural calculations on Blade 1, was located at the trailing edge at the bottom of the pin-fin cooling slot corresponding to a spanwise location between 5% and 10% span. Between these spanwise locations, the blade surface within $-1 < S/ARC < -0.8$ and $0.8 < S/ARC < 1$ was defined as the life-limiting region for CFD comparisons and is shown in Figure 3.1[9].

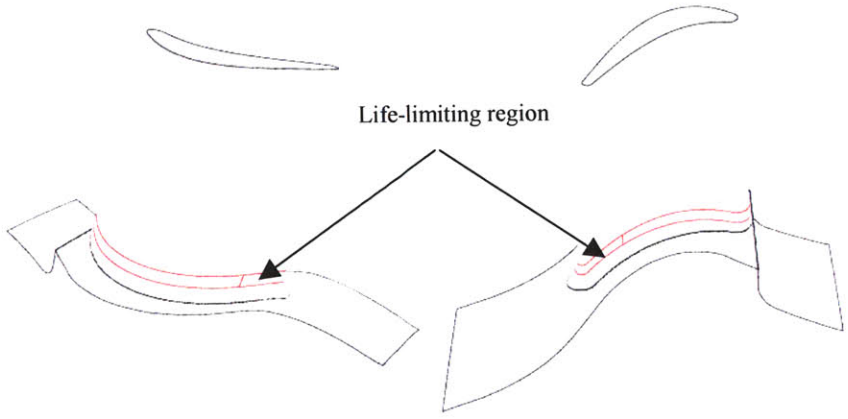

Figure 3.1: Life-limiting region in CFD comparisons.

The third section presents the results of deterministic life calculations for the three geometries. This is followed by probabilistic life estimation results and a discussion regarding the role of external thermal boundary conditions and their variability on the estimation of blade life and its variability for different designs.

[9] Heat transfer differences in the trailing edge circle region ($-1 < S/ARC < -0.95$ and $0.96 < S/ARC < 1$) were not considered due to the presence of the trailing edge slot, the large-scale flow separation, and the likely unsteady behavior of the trailing edge vortices in this region

3.1 Heat Transfer Governing Flow Features

Secondary flows have been shown to play an important role in turbine heat transfer [35, 40, 43], and a brief description of secondary flows in a generic turbine geometry is useful. A more detailed description can be found in [55, 78, 79]. A sketch, taken from [77] is included in Figure 3.2 to assist in visualizing these secondary flows. At the leading edge, a horseshoe vortex is formed near the hub due to the presence of spanwise gradients in relative total pressure and thus inlet normal vorticity. The pressure side leg of the horseshoe vortex typically merges with the passage vortex formed by the generation of streamwise vorticity associated with the turning

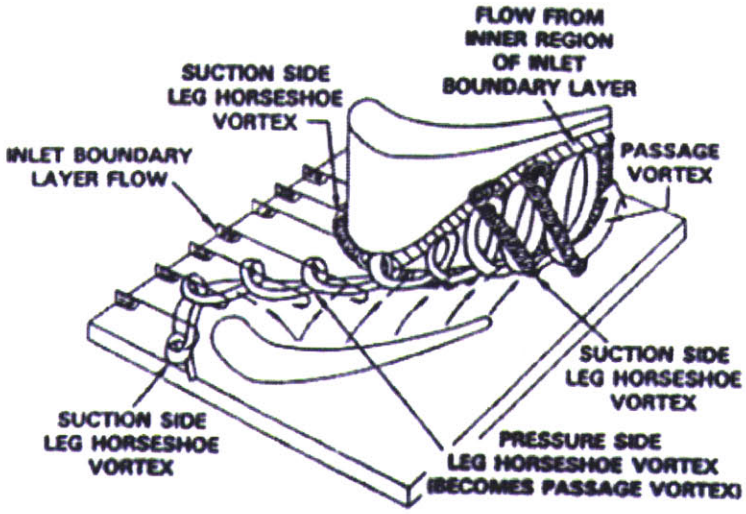

Figure 3.2: Sketch of secondary flows in a typical axial turbine cascade [77].

of flow originally containing circumferential vorticity (i.e. the incoming flow to the turbine). The suction side leg of the horseshoe vortex is typically lifted off the endwall by the incoming passage vortex and in some cases, is wrapped around the passage vortex [78]. In the tip region of an unshrouded turbine, hot flow from the pressure side crosses over the blade tip and forms what is called the tip vortex near the blade suction side. As mentioned in Appendix A2, the horseshoe vortex increased the leading edge hub heat transfer nearly threefold from the upstream hub value [43]. The flow features mentioned above, horseshoe vortex, passage vortex, and tip vortex, were all captured in the simulations.

During the three-dimensional simulations, the specified total temperature of the flow entering the cavity inlet was lower than that in the main gas path near the hub (0.43 vs. 0.88) and the cavity walls were kept isothermal at a non-dimensional temperature of 0.68, the same temperature as the main gas path surfaces. The cavity flow was thus heated by the solid surfaces in the cavity. Due to this flow heating and to a mass flow ratio of 0.1% (cavity to gas path), the relative total temperature of the flow leaving the cavity was comparable to that at the main gas path inlet near the hub. Figure 3.3 shows the relative total temperature in the near-hub passage vortex compared to that in the remainder of the main gas path.

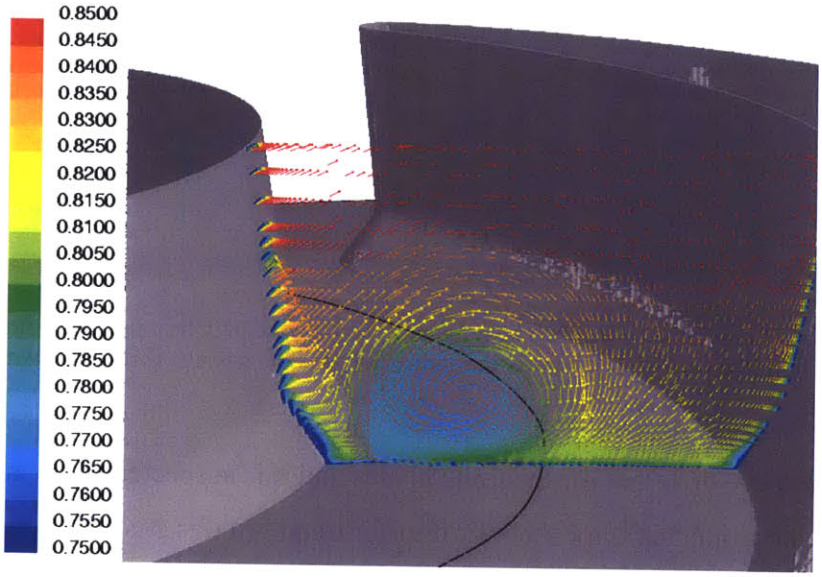

Figure 3.3: Relative velocity vectors colored by non-dimensional relative total temperature on a plane of constant axial position near mid-passage showing the colder hub and cavity flow in the vortex core surrounded by hotter main gas path flow (blades shown from 0 to 25% span).

As shown in Figure 3.4 and as reported in [43], the passage vortex migration and its associated flow impingement-detachment line resulted in large heat transfer gradients on the hub. This was also found to be the case on the blade suction side.

3.2 Heat Transfer Comparison of Nominal Blades

This section describes the observed differences in heat transfer between the three geometries.

At the leading edge, a consistent trend of highest peak heat transfer was observed for Blade 3. Similarly, the peak heat transfer for Blade 2 was consistently lowest. The actual percent differences from nominal are given in Table 3.1. As shown in Table 1.1, the leading edge radius

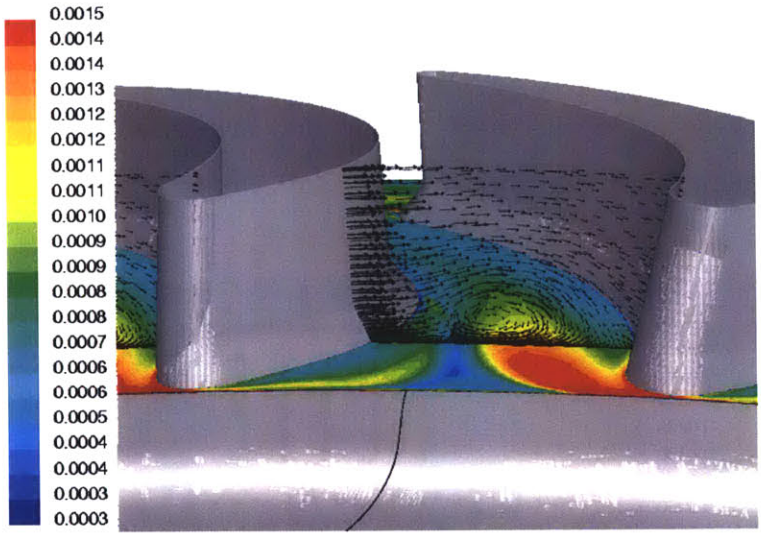

Figure 3.4: Contours of non-dimensional hub heat transfer showing the high heat transfer gradients resulting from the passage vortex impingement-detachment as it migrates through the passage (blades shown from 0 to 25% span).

and wedge angle were different for the three blades and it is suspected these geometric differences may be responsible for the heat transfer trend. In this study, the leading edge did not constitute a life-limiting region.

Spanwise Location	**% Difference in Leading Edge Peak Heat Transfer**	
	Blade 2	**Blade 3**
5% span	-7.0	6.8
10% span	-0.9	3.3
25% span	-2.6	3.6
50% span	-1.4	3.5
75% span	-0.6	1.7
90% span	-0.9	1.0
95% span	-0.7	1.2

Table 3.1: Leading edge peak heat transfer differences from nominal

Away from the leading edge, secondary flow differences were the dominant cause of heat transfer differences in the first 10% span. The higher loading in Blade 3 resulted in stronger pressure gradients, passage vortex, and pressure side to suction side flow migration for that case. As seen in Figure 3.5 a) and Figure 3.6, this resulted in increased impingement heat transfer on the suction side near the hub. The larger vortex in Blade 3, after impacting the suction side

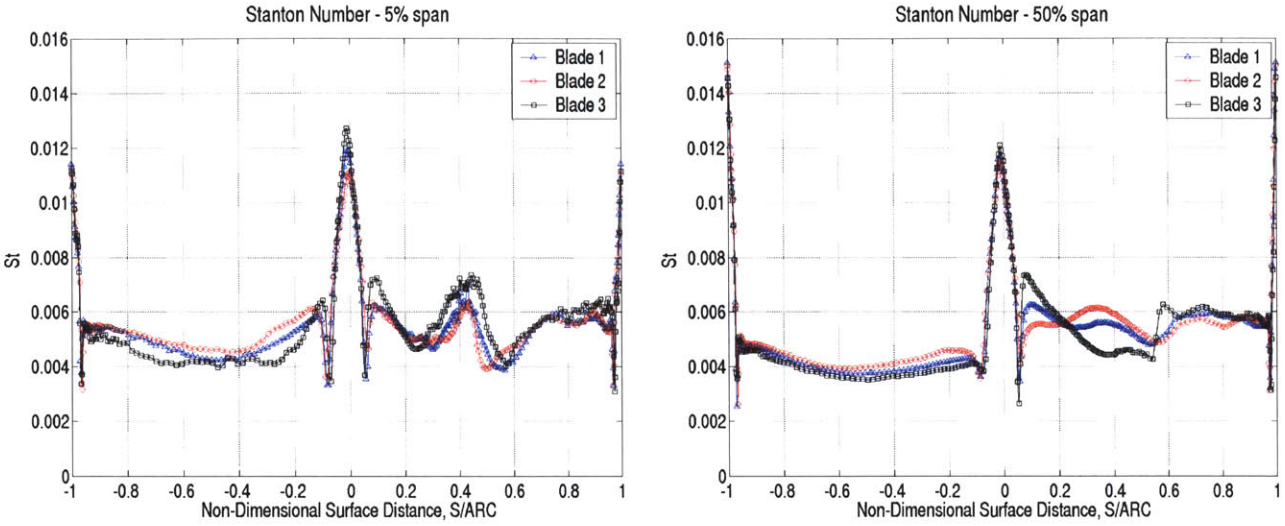

Figure 3.5: Comparison of three-dimensional heat transfer results: a) 5% span, b) 50% span.

earlier in the passage, was pushed further spanwise than in the other two cases resulting in a high heat transfer gradient region located further off the hub as seen in Figure 3.6. On the pressure side, Blade 2 exhibited somewhat higher heat transfer due to its lower pitch/chord ratio confining the passage vortex during its migration downstream and allowing it to more effectively bring hot midspan flow down the blade pressure side.

At 50% span (Figure 3.5 b)), the heat transfer differences were a result of the two-dimensional effects of turbulence intensity and flow acceleration described in Appendix D. The higher flow acceleration of Blade 3 resulted in lower heat transfer in the region between S/ARC = 0.2 and S/ARC = 0.5. After S/ARC = 0.6, at 50% span, the stronger adverse pressure gradient on Blade 3 resulted in a sharper increase in turbulence intensity and heat transfer for that case. Lower pressure side flow acceleration accounted for Blade 2's higher pressure side heat transfer in Figure 3.5 b).

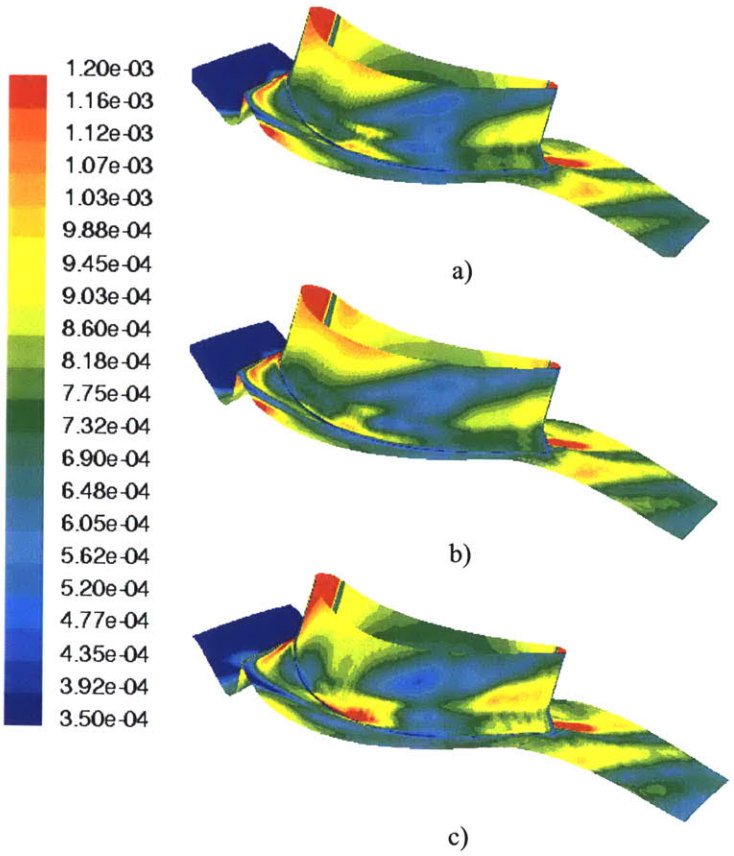

Figure 3.6: Effect of stronger secondary flows on near-hub suction side heat transfer (blades shown from 0 to 25% span): a) Blade 1, b) Blade 2, c) Blade 3.

Turbulence intensity and flow acceleration were again responsible for heat transfer differences at 75% span except in the region past S/ARC = 0.8 on the suction side. Here, as shown in Figure 3.7, Blade 3 exhibited higher heat transfer associated with the rapid diffusion of the tip vortex resulting in a zone of high turbulence as far down as 75% span.

Above 75% span, away from the leading edge, suction side differences in heat transfer were a result of differences in the path of the tip vortex between the three cases. In the case of Blade 2, the smaller pitch to chord ratio caused the tip vortex to remain closer to the blade and persist later into the passage resulting in generally higher heat transfer for this case. For Blade 3, the larger pitch to chord ratio allowed the tip vortex to migrate further off the suction side and diffuse into the passage.

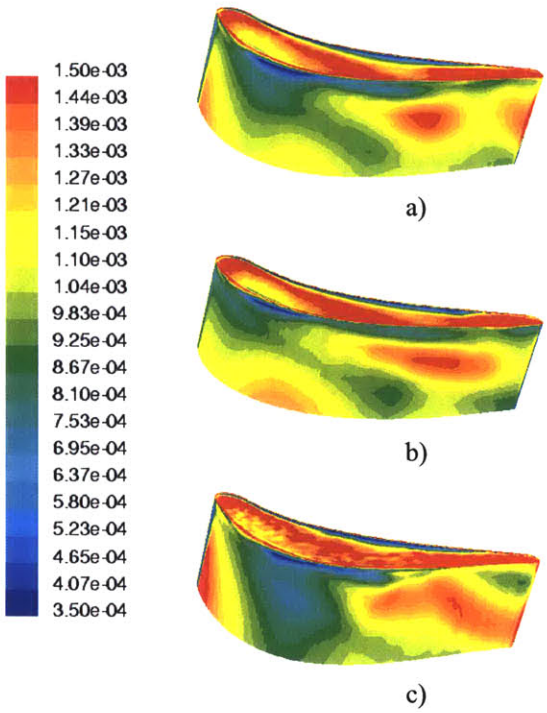

Figure 3.7: Heat flux contours showing effect of tip vortex on near-tip suction side heat transfer (blades shown from 75% to 100% span): a) Blade 1, b) Blade 2, c) Blade 3.

3.2.1 Heat Transfer Comparison in Life-Limiting Region

In the life-limiting region, the calculated heat transfer coefficients for Blades 1 and 2 were in good agreement. The maximum differences at 5% span were 2.4% and 4.6% on the pressure and suction side respectively. The maximum differences at 10% span were below 3.5% on both sides of the blade. The Blade 3 heat transfer coefficient estimates exhibited more deviation from nominal with maximum pressure side differences of 9.4% at both spanwise locations. The differences were greater on the suction side with maximum values of 15% at 5% span and 23.7% at 10% span.

3.3 Comparison of Deterministic Life Estimates

Before performing probabilistic thermal-structural analyses, deterministic calculations were conducted on the three blade geometries. The results were used to assess the impact of external aerothermodynamics on blade life.

The metal temperature distributions obtained from the thermal calculations are shown in Figure 3.8. Although the maximum temperature was the same in all cases, there were differences in the

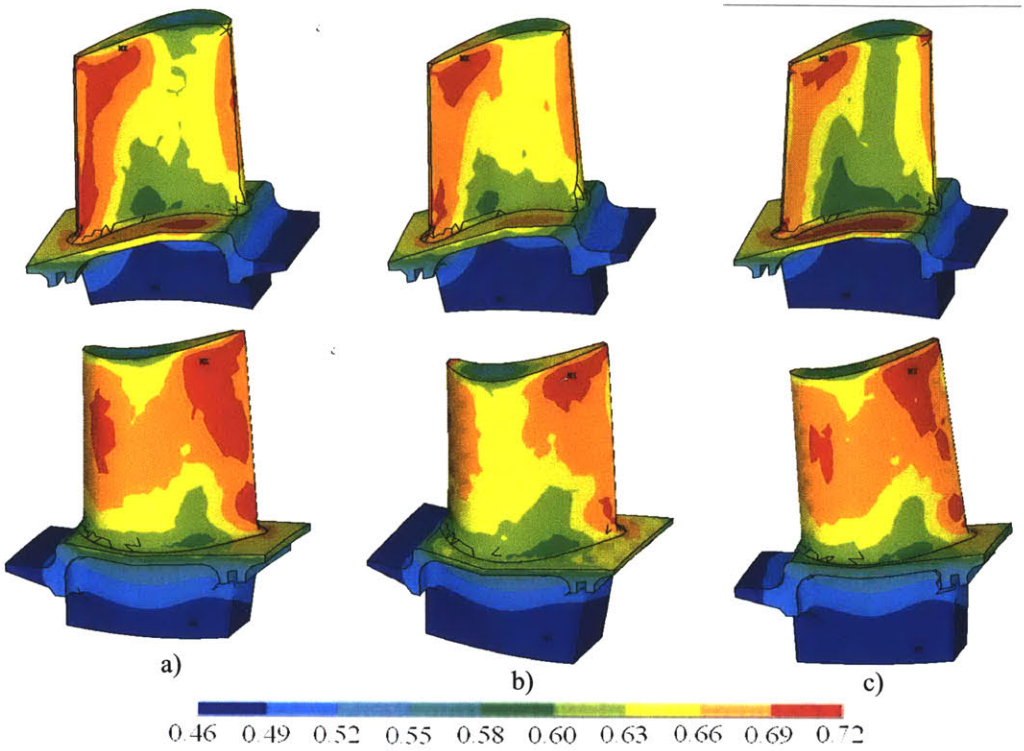

Figure 3.8: Metal temperature distributions on pressure (top) and suction (bottom) side: a) Blade 1, b) Blade 2, c) Blade 3.

distribution of hot zones on both the pressure side and suction side. In the life-limiting region (trailing edge near hub), a hot spot was predicted in all three simulations. For Blade 1, the hot spot was larger on both the suction side and pressure side.

The stress and strain distributions for the three nominal blades were similar and the reader is referred to [53] if they are needed. The location of maximum stress and strain was also the same, the trailing edge at the bottom of the cooling slot. Differences in the average equivalent stress and strain were 0.9% and 20.7% for Blade 2 and –6.3% and 15.5% for Blade 3, compared to Blade 1. The estimated life of Blades 2 and 3 was 34% and 17% lower than that of Blade 1 respectively. As explained in [53], strain played a more important role than stress in the determination of blade life.

Recalling the CFD results presented earlier in this section, in the life-limiting region, the difference in heat transfer coefficient between Blades 1 and 2 was less than 5% everywhere. The differences varied from an under-estimation of 9.4% on the pressure side to an over-estimation of 23.7% on the suction side for Blade 3. Based on these results and their lack of correlation with the life results reported above, it was concluded that the differences in external thermal boundary conditions did not play an important role in the observed deterministic life differences. As explained in [53], these life differences were more likely due to structural variations among the blades.

3.4 Comparison of Probabilistic Life Estimates

Following the deterministic case studies, probabilistic thermal-structural analyses were conducted on the three nominal geometries [53]. During these simulations, seven noise parameters were allowed to vary. The variations were set according to the normal distribution parameters provided by MHI and shown in Table 3.2. The variability imposed on the convection conditions (internal and external temperatures and heat transfer coefficients) was global. For example, during a probabilistic simulation, for a particular calculation, the heat transfer coefficient over the entire blade surface was scaled by the same factor. For the temperatures, the variability was imposed using an offset factor of mean zero and variability according to Table 3.2, hence the dimensional specification of variability. No local variation was modeled for any of the noise parameters.

Noise Parameter	Variability
External Heat Transfer Coefficient	$0.2*CFD/\ \Phi^{-1}(0.9)$
External Convection Temperature	$30/\Phi^{-1}(0.9)$ K
Internal Heat Transfer Coefficient	$0.2*CFD/\Phi^{-1}(0.9)$
Internal Convection Temperature	$30/\Phi^{-1}(0.9)$ K
TBC Thickness	$0.1*Mean/\Phi^{-1}(0.9)$
TBC Conductivity	$0.1*Mean/\Phi^{-1}(0.9)$
Metal Conductivity	$0.1*Mean/\Phi^{-1}(0.9)$

Table 3.2: Noise parameter variability used in the probabilistic thermal-structural analyses ($\Phi^{-1}(0.9)$ is used to represent the 90^{th} percentile of a cumulative probability distribution).

To generate a sufficient population from which to base reliable probabilistic conclusions, 1000 simulations were conducted for each blade. The goals of the study were to (1) identify the noise parameters that drive blade life variability and (2) identify any differences in blade life variability among the three designs.

The results of the probabilistic simulations are shown in Table 3.3 listing the mean and standard deviation for the estimated life of each blade. Blade life distributions are shown in Figure 3.9. As was the case in the deterministic results of Section 3.2.2 summarized in Table 3.3, Blade 2 was found to have lowest mean life and Blade 1 highest. There were minor changes in blade life variability, in an absolute sense and as discussed in [53], based on considerations of coefficients of variation and further statistical analyses, the Blade 1 design was determined to be more robust to variability.

	Blade Life Results		
	Deterministic	**Mean**	**Standard Deviation**
Blade 1	1.024	1	0.054
Blade 2	0.676	0.736	0.057
Blade 3	0.847	0.851	0.070

Table 3.3: Deterministic, mean, and standard deviation of blade life for three nominal blades (normalized by mean life of Blade 1).

The non-parametric correlation coefficients[10] of all noise parameters with respect to blade life

[10] Correlation coefficients are used as a measure of relation between one variable and another. For example, in our case, the relation between variability in each of the noise parameters and that in blade life was sought. Contrary to parametric correlation coefficients, non-parametric correlation coefficients do not require the assumption of a particular distribution for either the input or the output. The correlation coefficients shown in Table 3.4 were calculated as

$$correlation\_coefficient = 1 - \frac{6\Sigma d^2}{n(n^2-1)}$$

where n is the number of samples and d is the difference between the rank order of the input parameter and that of the output parameter for all samples in the probabilistic study. Values of correlation coefficients can range from –1 to 1. A value of zero indicates no correlation, an absolute value of 1, strong correlation, and a negative sign indicating opposite correlation.

were calculated [53] and are listed in Table 3.4. In all cases, the external heat transfer coefficient and convection temperature (shaded gray in Table 3.4) exhibited weak to moderate correlation

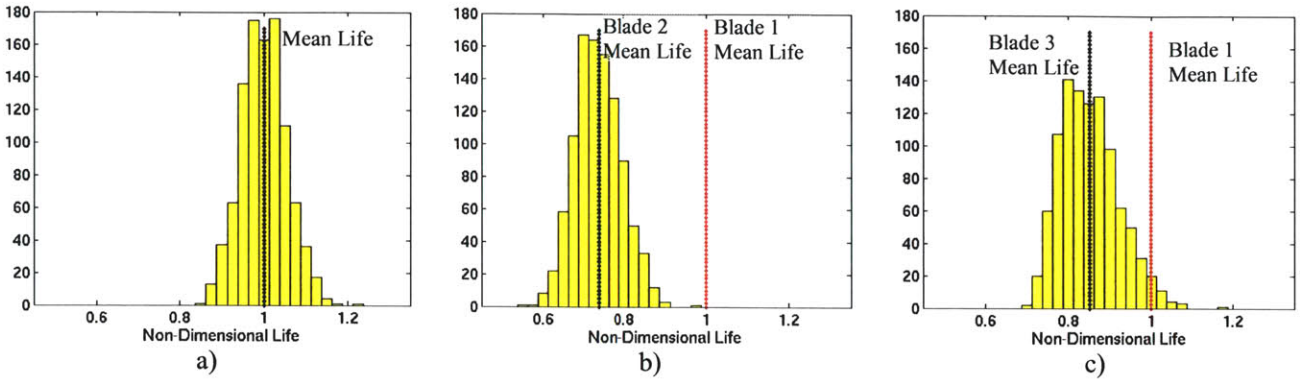

Figure 3.9: Blade life distributions for three nominal blades: a) Blade 1, b) Blade 2, c) Blade 3. The vertical axis represents the number of occurrences in the probabilistic simulations.

with respect to life. Again, this is consistent with the findings from the deterministic case studies in Section 3.2.2 showing that the external thermal boundary conditions played a minor role in blade life estimation. In contrast, for all three blades, variability in internal convection temperature (shaded blue in Table 3.4) was found to be the key driver of blade life variability with correlation coefficients near -0.8.

Noise Parameter	Life Correlation Coefficients		
	Blade 1	Blade 2	Blade 3
External Heat Transfer Coefficient	-0.274	-0.230	-0.219
External Convection Temperature	-0.323	-0.227	-0.223
Internal Heat Transfer Coefficient	0.267	0.337	0.231
Internal Convection Temperature	-0.800	-0.816	-0.884
TBC Thickness	0.101	0.069	0.068
TBC Conductivity	-0.081	-0.068	-0.054
Metal Conductivity	0.001	-0.018	0.020

Table 3.4: Blade life correlation coefficients for three nominal blades.

Given our modeling assumptions and approach for calculation of life, the results of this chapter can be summarized as follows:

- Blade-to-blade differences in local external thermal boundary conditions have a minor impact on blade-to-blade estimated life differences.

- Consistent with the first point, global noise in the external thermal boundary conditions has a weak to moderate impact on blade life variability.

- Among the noise parameters investigated, variability in the internal cooling temperature is the main driver of life variability.

4. Impact of Modeling Approximations on Heat Transfer and Life

As observed in Chapter 3, external heat transfer variability had a relatively weak impact on blade life. This result suggests that modeling assumptions could be made to reduce the computational costs without significantly affecting blade life estimates. To investigate the life impact of such modeling assumptions, several case studies were conducted in which flow and /or geometric modifications were made to the baseline studies of Chapter 3. Specific features considered and their impact on life are listed in Table 4.1[11].

Section	Feature Investigated	Difference in Life (from reference case)
4.1	Two-dimensional vs. three-dimensional flow	< 0.8%
4.2.1	Seal cavity	2.6%
4.2.2	Seal mass flow rate	< 1%
4.2.3	Inlet boundary layers	0.8%
H1	Root fillet geometry	< 0.3%
H2	Inlet boundary layers without seal cavity	2.0%

Table 4.1: Summary of life impact of various modeling approximations.

4.1 Two-Dimensional Flow

4.1.1 Description of Study

To assess the impact of simplified modeling on blade life estimation, the results of two-dimensional CFD simulations at 5%, 10%, 25%, 50%, 75%, and 95% span were used to generate a three-dimensional boundary condition file to be used in the thermal structural calculations. Although the two-dimensional simulations could not capture the effects of secondary flows, the heat transfer levels in the life-limiting region were well approximated (~ 10% to 15% difference). The study resulted in a 1% difference in blade life compared with that obtained

[11] The life difference is given in an absolute sense. The reader is referred to the appropriate section for a description of the reference case for each study since it varied depending on the feature investigated.

using boundary conditions from three-dimensional CFD simulations. The results of the study showed that, given our models and approach for calculating life, provided the life-limiting region is the same using two- and three-dimensional CFD data, 10% - 15% differences in heat transfer to the life-limiting region have a minimal impact on blade life and heat transfer differences (as high as 40%) away from the life-limiting region have no effect on the estimated life.

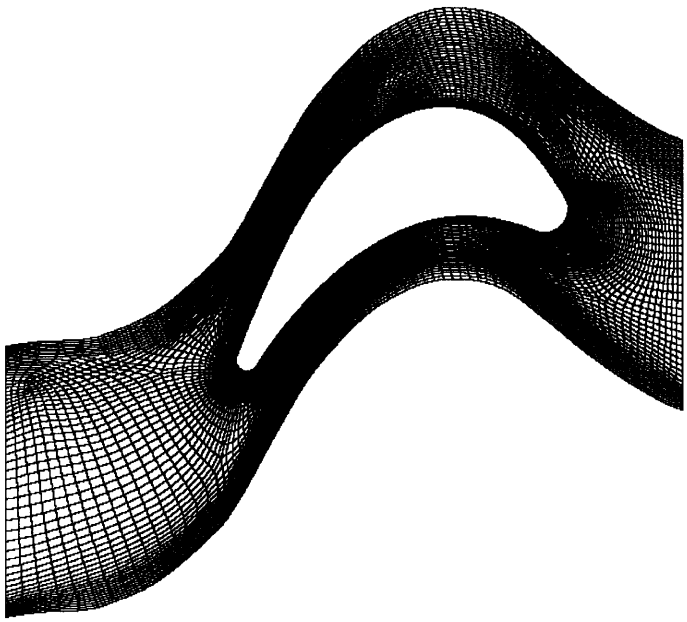

Figure 4.1: Two-dimensional, 5% span grid for Blade 1

The two-dimensional grids were generated by taking constant-span cuts along the three-dimensional blade and projecting them onto a plane normal to the spanwise direction. Figure 4.1 shows the grid generated for the 5% span two-dimensional calculation on Blade 1. The grids at all other spanwise locations for all three blades were of identical topology and wall resolution. Although calculations were conducted at several spanwise locations, the trends at all locations were similar and only the 50% span results will be discussed here.

The inlet conditions (total pressure, total temperature, and flow angle) for the two-dimensional cases were constructed from those used in an already completed three-dimensional case without cavity. Since spanwise redistribution was predicted in the three-dimensional case, mass-averaged quantities existing 10% chord upstream of the LE at the same spanwise location as the

two-dimensional case under consideration were used to construct inlet conditions for the two-dimensional cases. The quantities conserved in the averaging process were mass,

$$\int_{\theta_1}^{\theta_2} \rho u_x r d\theta = \dot{m}' \qquad \text{E 4.1}$$

axial momentum,

$$\int_{\theta_1}^{\theta_2} \left(\rho u_x^2 + p\right) r d\theta = \dot{m}' \overline{u}_x + \overline{p} r \left(\theta_2 - \theta_1\right) \qquad \text{E 4.2}$$

tangential momentum,

$$\int_{\theta_1}^{\theta_2} \rho u_x u_y r d\theta = \dot{m}' \overline{u}_y \qquad \text{E 4.3}$$

and energy

$$\int_{\theta_1}^{\theta_2} \rho u_x T_T r d\theta = \dot{m}' \overline{T}_T \qquad \text{E 4.4}$$

where r denotes the radial position of the two-dimensional case to be conducted and the overbar represents the averaged quantities used in the specification of inlet quantities in the two-dimensional cases (total pressure, total temperature, flow angle). The other symbols are described in the nomenclature. E 4.5 to E 4.7, and isentropic flow relations were then used to allow specification of the inlet static and total pressure.

$$\frac{\dot{m}'}{r\left(\theta_2 - \theta_1\right)} = \overline{p}_T \sqrt{\frac{\gamma}{R\overline{T}_T}} \frac{\overline{M}_x}{\left(1 + \frac{(\gamma - 1)}{2} \overline{M}^2\right)^{\frac{(\gamma+1)}{2(\gamma-1)}}} \qquad \text{E 4.5}$$

$$\overline{M} = \frac{\sqrt{\overline{u}_x^2 + \overline{u}_y^2}}{\sqrt{R\gamma\left(\overline{T}_T - \frac{\left(\overline{u}_x^2 + \overline{u}_y^2\right)}{2c_p}\right)}} \qquad \text{E 4.6}$$

$$\overline{M}_x = \frac{\overline{u}_x}{\sqrt{R\gamma\left(\overline{T}_T - \frac{\left(\overline{u}_x^2 + \overline{u}_y^2\right)}{2c_p}\right)}} \qquad \text{E 4.7}$$

The constant inlet turbulence quantities used in the three-dimensional calculations were used in all two-dimensional cases.

4.1.2 Global Heat Transfer Observations

The results of the two-dimensional simulations at 50% span are plotted in Figure 4.2. The computed heat transfer for all three blades is generally higher on the suction side than the pressure side.

A zone of high acceleration on the leading edge circle (S/ARC = -0.08 to S/ARC = 0.08) followed by an adverse pressure gradient resulted in large changes in heat transfer near the leading edge. At some locations (pressure side at 10%, 25%, and 50% span for all three blades, suction side at 5% and 10% span for Blade 3, and pressure side at 5% span for Blade 1), this adverse pressure gradient was found to cause flow separation and reattachment at the point of tangency between the leading edge circle and the rest of the blade surface on either the suction side or pressure side. The adverse pressure gradient and small separation bubbles were found to have an impact on the heat transfer downstream.

Between S/ARC ~ 0.35 and S/ARC ~ 0.45, appreciable heat transfer differences between the three blades were seen at all spanwise locations. As will be explained later, this was a result of differences in flow acceleration.

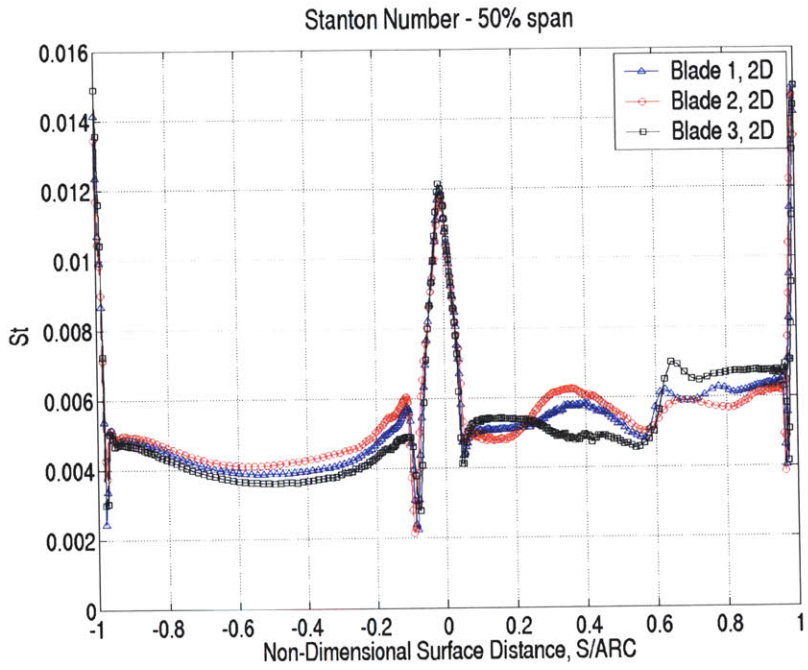

Figure 4.2: Comparison of two-dimensional heat transfer results at 50% span.

Finally, we can see the effects of an adverse pressure gradient on the suction side near the trailing edge (S/ARC ~ 0.6 to trailing edge). This location corresponds to the uncovered section of the blade suction side. The adverse pressure gradient increased the near-wall turbulence intensity which, as will be described in Section 4.1.4, augmented the heat transfer to the wall.

4.1.3 Heat Transfer Differences and Trends

Consistent with the results presented in Chapter 3, the stagnation heat transfer was higher for Blade 3 than for the other two blades at all spanwise locations. The average percent difference in leading edge peak heat transfer between Blade 3 and Blades 1 and 2 was 2% and 3.3% respectively.

On the pressure side, near the leading edge, the heat transfer for Blade 2 was highest and that for Blade 3, lowest. These local differences are attributed to the effect of a stronger near-leading edge adverse pressure gradient in the case of Blade 2 resulting in higher values of near-wall

turbulence intensity. The situation is reversed on the suction side where the heat transfer for Blade 3 is highest and that for Blade 2 lowest.

In the pressure side trailing edge region, the predicted differences in heat transfer diminished due to the turbulence attenuating effect of flow acceleration in this area.

On the suction side, the flow in Blade 3 experiences higher acceleration over a longer portion of the airfoil. This results in a consistent decrease in heat transfer until S/ARC ~ 0.6. In the case of Blade 1 and Blade 2, the high acceleration region is shorter resulting in a region where the attenuating effect of acceleration is dominated by the heat transfer enhancing effect of turbulence intensity. As in E 2.2, the turbulence intensity depends on the turbulent kinetic energy, an increasing quantity through the passage, as well as on the inverse of the flow velocity.

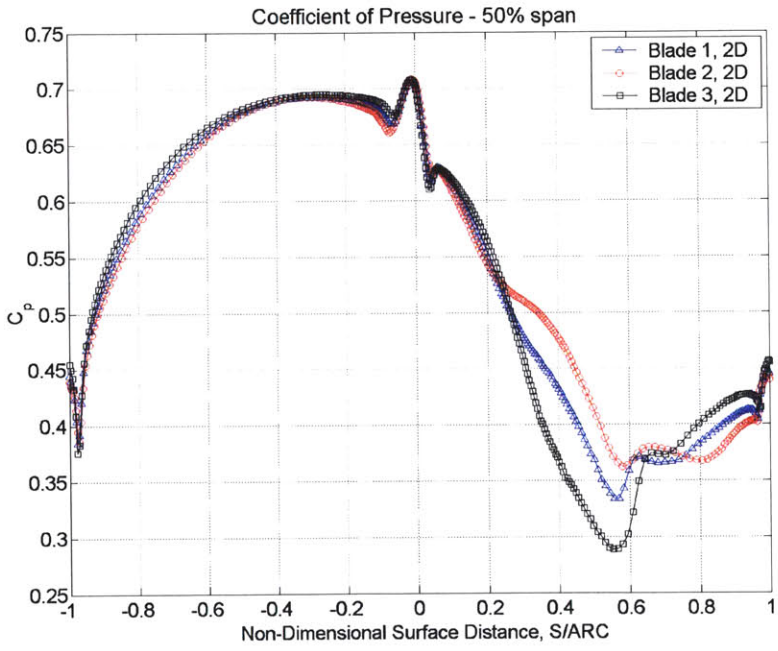

Figure 4.3: Two-dimensional pressure distribution at 50% span.

Still on the suction side, near the trailing edge (S/ARC ~ 0.6 and on), Blade 3 heat transfer estimates are again highest and those of Blade 2, lowest. As mentioned earlier in this section, the adverse pressure gradient in this region results in a sharp increase in near-wall turbulence intensity for all three blades. Since all three blades were designed to yield the same work, the

higher pitch to chord ratio of Blade 3 necessitates higher loading and, as can be seen in Figure 4.3, the adverse pressure gradient near S/ARC = 0.6 is more prominent for Blade 3 than for the other two blades. The resulting larger increase in turbulence intensity lead to the higher Blade 3 heat transfer here.

4.1.4 Comparison of Two- and Three-Dimensional CFD Results

Heat transfer comparisons between two- and three-dimensional simulations were focused in the life-limiting region.

On the pressure side, it was found that two-dimensional calculations under- estimated the three-dimensional heat transfer for cases with and without the seal cavity. The under-estimation was approximately 15% at 5% span and 10% at 10% span. Figure 4.4 shows the results for Blade 1 at 5% span in the pressure side life-limiting region. The results for the other blades were similar and are not shown. The difference between two- and three-dimensional results was due to the

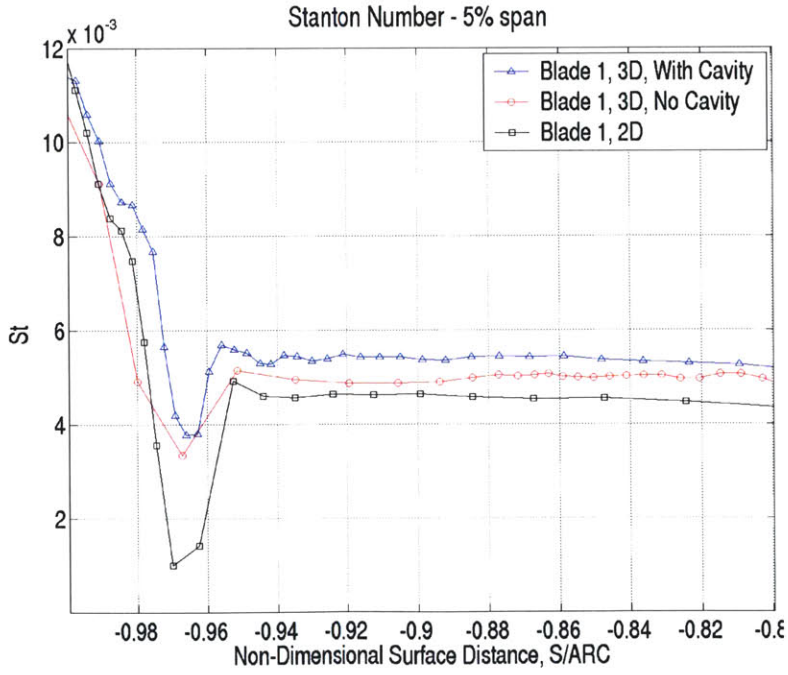

Figure 4.4: Two- and three-dimensional heat transfer results in pressure side life-limiting region of Blade 1 (5% span).

pressure side spanwise spreading of the inlet total temperature profile in the three-dimensional calculations, a flow feature not captured in the two-dimensional calculations.

On the suction side, although absolute magnitudes of heat transfer coefficient were relatively well-matched, as shown in Figure 4.5, the trends were less consistent than on the pressure side with two-dimensional calculations over-estimating three-dimensional ones at some spanwise

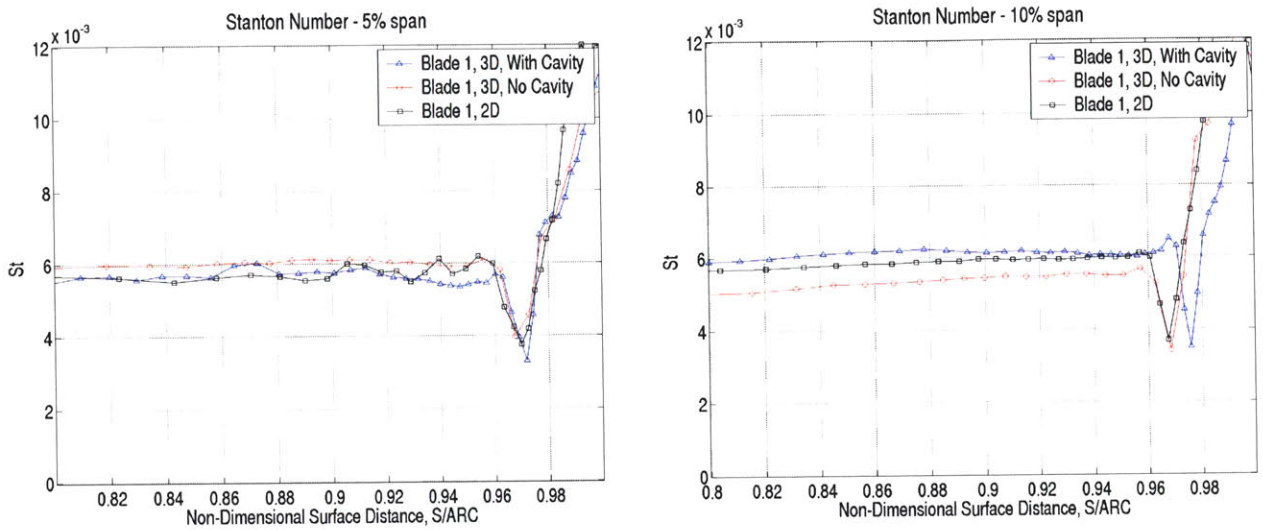

Figure 4.5: Two- and three-dimensional heat transfer results in the suction side trailing edge region of Blade 1: a) 5% span , b) 10% span .

location and under-estimating them at another. The lack of consistency observed on the suction side is a result of the different secondary flow patterns in the cases with and without the seal cavity as well as the localized nature of these flow features. Since the two-dimensional calculations do not capture any secondary flow effects, it is not unreasonable to expect them to underestimate the heat loads at one location and overestimate them at another.

As shown in Figure 4.6, over the rest of the blade surface (i.e. away from the life-limiting region), the two-dimensional calculations estimated the heat load to the blade with varying levels of accuracy due to their inability to capture secondary flow effects.

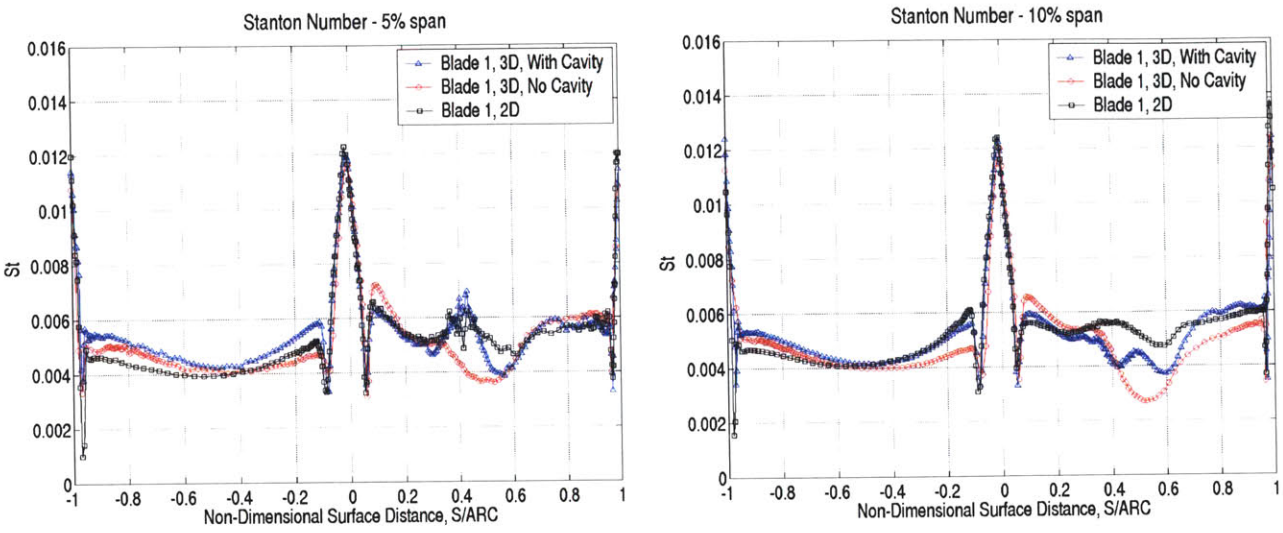

Figure 4.6: Two- and three-dimensional near-hub heat transfer comparison: a) 5% span, b) 10% span.

4.1.6 Thermal – Structural Analyses

Given the limitations associated with the mapping of the CFD data unto the structural model and the previously reported weak correlation between external thermal conditions and blade life, the thermal-structural calculations based on two-dimensional CFD data were expected to yield blade life estimates in reasonable agreement with those obtained using three-dimensional CFD data. Due to computational restrictions, the comparative FEM simulations were performed on the Blade 1 geometry only. The FEM calculation using three-dimensional CFD data employed the boundary conditions of the nominal Blade 1 case. The results of the FEM calculations are summarized as follows:

- As shown in Figure 4.7, except for the lower heat transfer region resulting from the migration of the passage vortex on the suction side, the model employing two-dimensional CFD data had a similar suction side metal temperature distribution as that using three-dimensional CFD data. Similar agreement was observed on the pressure side.

- The location of maximum blade temperature shifted from blade tip leading edge to approximately 90% span on the suction side, close to the trailing edge.

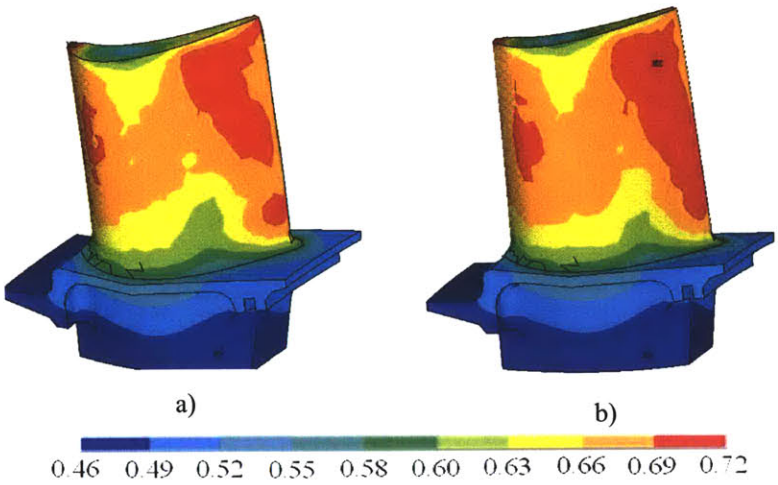

Figure 4.7: Suction side metal temperature distributions: a) Using three-dimensional CFD boundary conditions, b) Using two-dimensional CFD boundary conditions.

- Similar distributions of stress and strain in the blade were obtained for the two simulations as shown in Figure 4.8 and Figure 4.9.

- The location of maximum stress and strain remained unchanged at the bottom of the trailing edge cooling slot

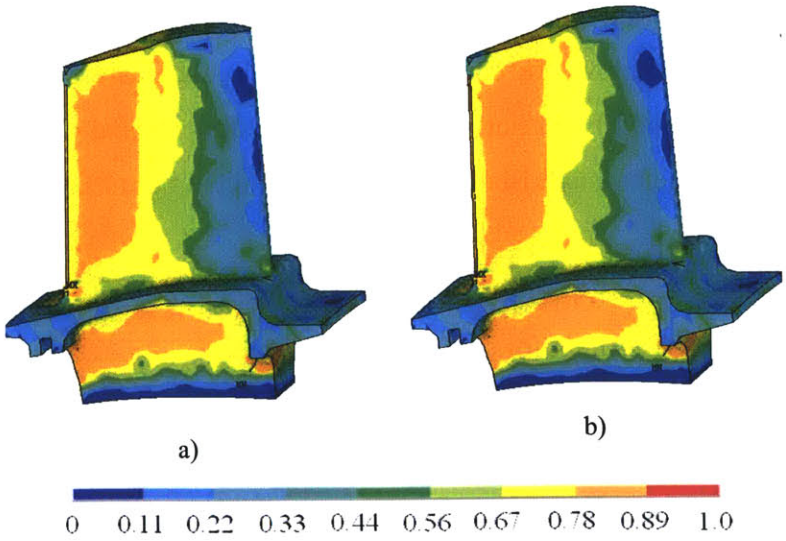

Figure 4.8: Pressure side stress distribution: a) Using three-dimensional CFD boundary conditions, b) Using two-dimensional CFD boundary conditions.

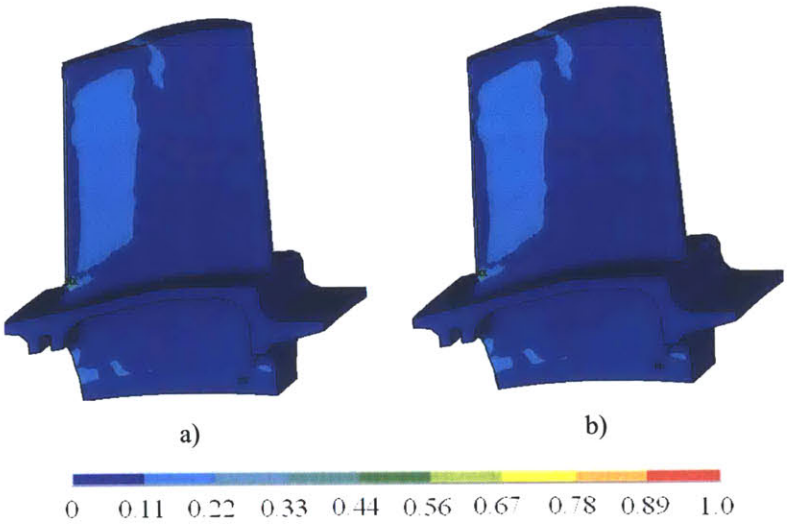

Figure 4.9: Pressure side strain distribution: a) Using three-dimensional CFD boundary conditions, b) Using two-dimensional CFD boundary conditions.

- The average equivalent stress and strain levels in the life-limiting region were decreased by 0.08% and 0.17% respectively when comparing the values obtained from two-dimensional CFD boundary conditions to those using three-dimensional CFD boundary conditions.

- These small changes in average equivalent stress and strain resulted in a blade life increase of less than 0.8% when using two-dimensional CFD boundary conditions

In the comparison of results from two- and three-dimensional calculation, flow and heat transfer patterns bear little similarity, particularly near the hub where secondary flows have a dominant effect on three-dimensional heat transfer. The results of the simplified modeling study show that, heat transfer differences as high as 10% - 15% in the life-limiting region and as high as 40% elsewhere on the blade result in minimal differences in estimated blade life. Thus, for the geometries, models, and approach considered in this project, two-dimensional calculations can be used to reliably estimate blade life.

4.2 Impact of Geometric and Flow Modeling on Blade Life Estimation

Several case studies were conducted to assess the impact of geometric and flow features on heat transfer and blade life. All calculations were conducted on the Blade 1 geometry. Although some geometric features were varied in the CFD case studies, due to time and computational restrictions, the baseline Blade 1 geometry was maintained in the thermal-structural part of all case studies. Therefore, the life impact of features such as the fillet geometry and the seal cavity were only assessed from an external heat transfer perspective. The wall friction and heat transfer boundary conditions used in the comparison of the three blades were used in all cases. For the FEM simulations, the internal cooling mass flow rate was kept at the nominal value for Blade 1.

The results of the case studies will all be presented in a similar fashion. First, a description of the study including any geometric or boundary condition modifications from Blade 1 will be given. This will be followed by an overall comparison of the results and a quantitative heat transfer comparison in the life-limiting region. Each case study will end with the presentation of life estimation results and a conclusion regarding the impact of the study's feature on blade life.

4.2.1 Effect of Seal Cavity

The seal cavity was found to increase the suction side heat transfer particularly at the point of secondary flow impingement and in the life-limiting region. Augmentations as high as 14% were obtained in the latter resulting in an estimated life reduction of 2.6%.

4.2.1.1 Description of Study

The seal cavity is a common feature in high pressure turbines. Typically, some form of seal within the cavity coupled with a positive pressure difference is used to prevent hot gas ingestion into the cavity and the machine's core. The pressure difference results in a small but appreciable flow crossing the seal, entering the cavity and mixing with the main gas path flow. Since different future designs may or may not have the same type of stator-rotor interface, its effect on the heat transfer, particularly in the life-limiting region, was of interest.

Figure 4.10 shows two-dimensional projections of a 50% pitch cut through the two flow domains investigated. Boundary conditions at the main gas path inlet and outlet for both cases were the same and equal to those used in the comparison of the three nominal blades. The inlet conditions to the seal cavity inlet were given in Section 2.4.2.

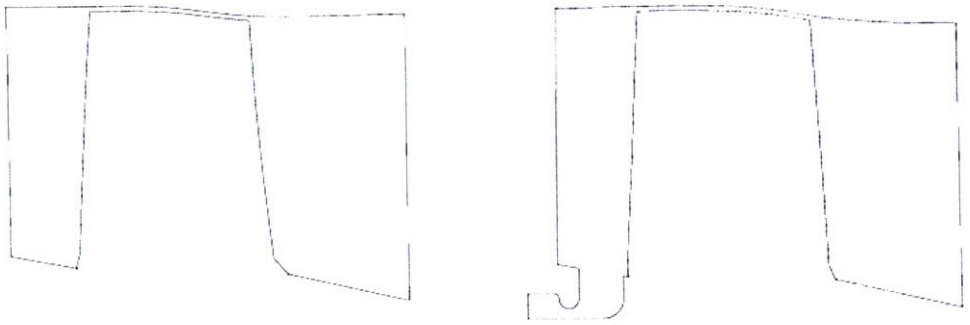

a) b)

Figure 4.10: Two-dimensional 50% pitch CFD domain projections showing geometry a) without and b) with seal cavity.

4.2.1.2 Overall Heat Transfer Comparison

As shown in Table 4.2, the leading edge peak heat transfer in the case without cavity was consistently lower than that with cavity. This was due to main gas path flow recirculation in the cavity which brought hotter near-midspan flow in the hub region at stagnation.

Near the leading edge (from S/ARC = -0.4 to S/ARC = 0.2), adverse pressure gradients and flow separation dominated the differences in heat transfer. On the pressure side, a small separation bubble was predicted for the blade with cavity at 5%, 10%, and 25% span. The associated

Spanwise Location	Difference in Leading Edge Peak Heat Transfer
5%	- 2.6%
10%	- 2.7%
25%	- 1.2%

Table 4.2: Effect of seal cavity on leading edge peak heat transfer.

increase in near-wall turbulence intensity resulted in higher heat transfer for this case as seen in Figure 4.11 a) through c). On the suction side, separation was predicted for the case without cavity at 5% and 10% span. At 25%, there was no separation. The heat transfer results on the suction side near the leading edge are consistent with these observations.

Further downstream (S/ARC < -0.4), on the pressure side, heat transfer differences were small, the maximum difference of 11% occurring at 5% span near S/ARC = 0.9. The cavity did not

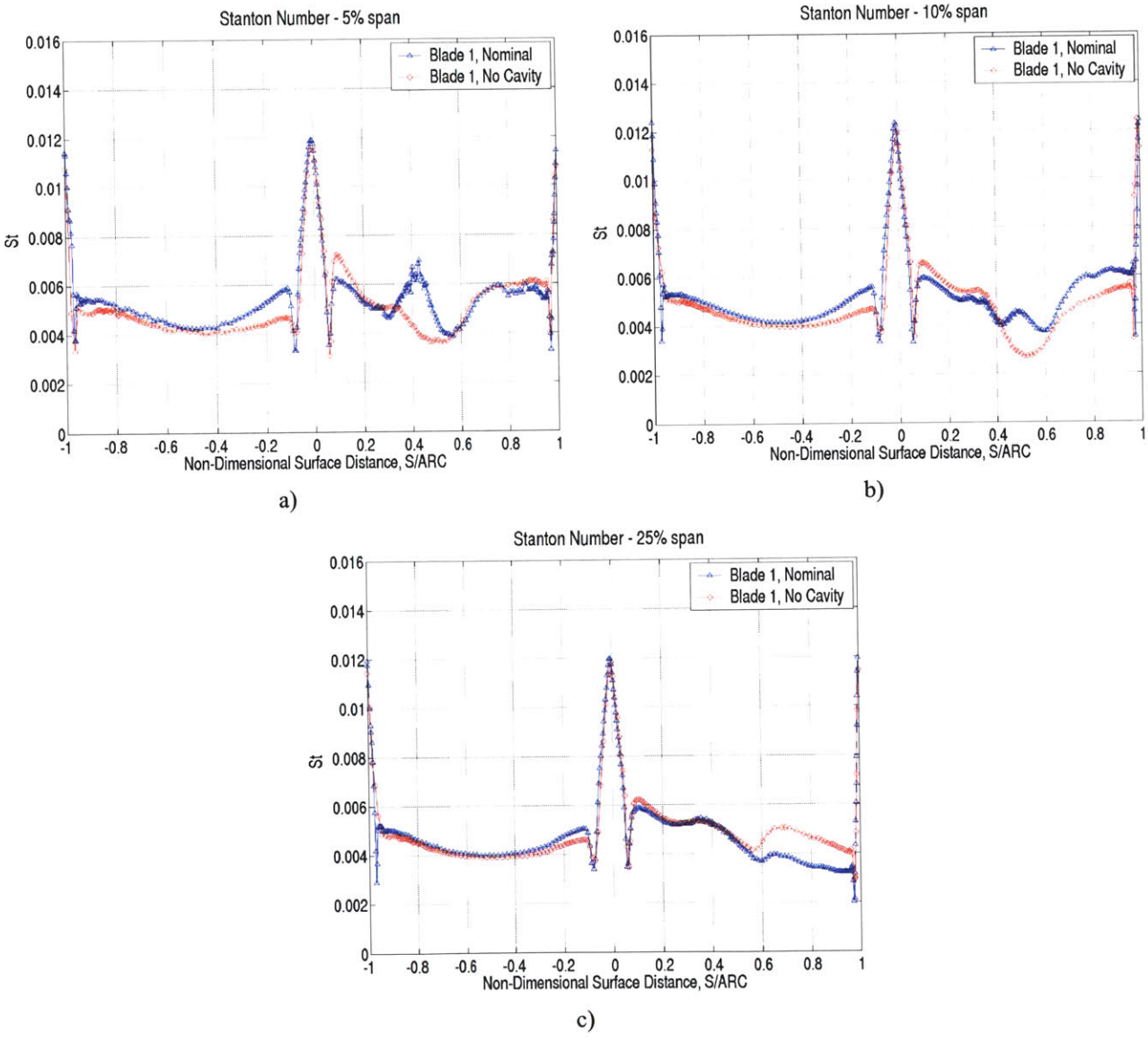

Figure 4.11: Effect of seal cavity on heat transfer: a) 5% span, b) 10% span, c) 25% span.

appear to play an important role on pressure side heat transfer away from the leading edge. On the suction side, stronger secondary flows in the case with cavity resulted in maximum heat transfer differences of 43%, 38%, and 35% at 5%, 10%, and 25% span respectively. In both cases, the suction side was marked by a low heat transfer zone migrating spanwise through the passage. The flow exiting the seal cavity strengthened and expanded the pressure side horseshoe-passage vortex structure. The result was more pronounced suction side impingement as well as higher relative total temperatures in the near hub region as the vortex entrained flow from further spanwise to impinge on the suction surface as shown in Figure 4.12. At 50% span, the effects of the seal cavity were no longer apparent.

4.2.1.3 Heat Transfer Comparison in Life-Limiting Region

At 5% span, the heat transfer for the case without cavity was estimated everywhere lower than that with cavity. The maximum difference on pressure side and suction side was of 11%. At 10% span, the pressure side differences were lower with a maximum difference of 5.5%. The suction side difference in heat transfer, a result of the passage vortex migrating further away from the hub in the case with cavity, was 14% in the life-limiting region.

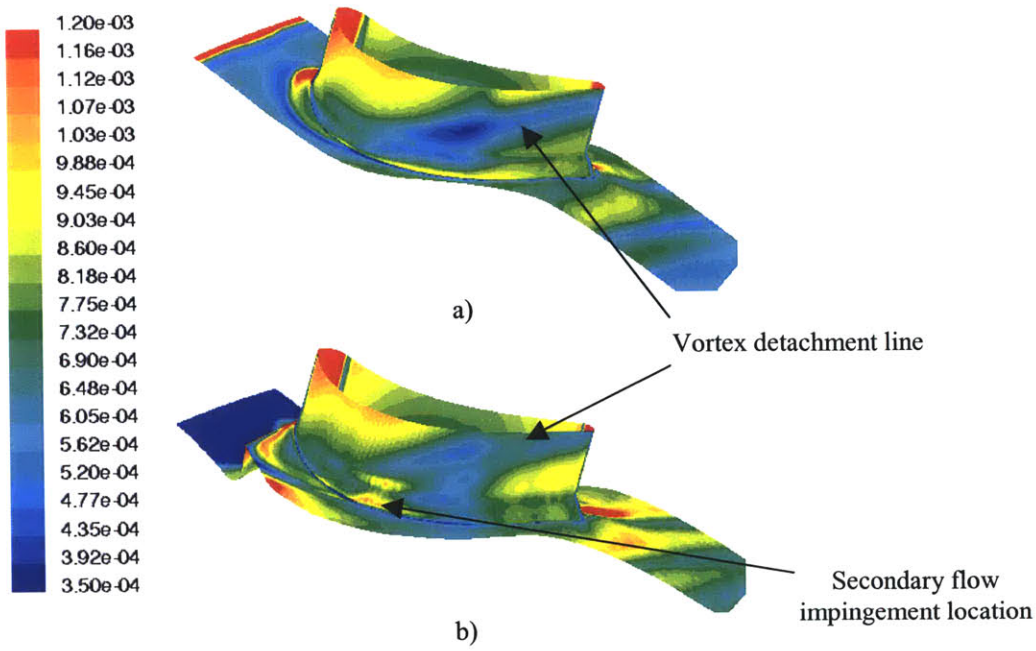

Figure 4.12: Heat transfer enhancing effect of seal cavity on suction side near-hub heat flux pattern (blades shown from 0 to 25% span): a) without and b) with seal cavity

In summary, the seal cavity increased leading edge heat transfer due to flow recirculation within the cavity, had little impact on the pressure side heat transfer, and generally augmented suction side heat transfer due to stronger secondary flows. The suction side regions most affected by these secondary flows were the impingement location of the near-hub migrating flow and the life-limiting region.

4.2.1.4 Effect of Seal Cavity on Blade Life

The blade surface metal temperature distributions were similar and are shown in Figure 4.13. The stress and strain distributions were also very similar with the cooling slot region being more heavily strained than the remainder of the blade in both cases.

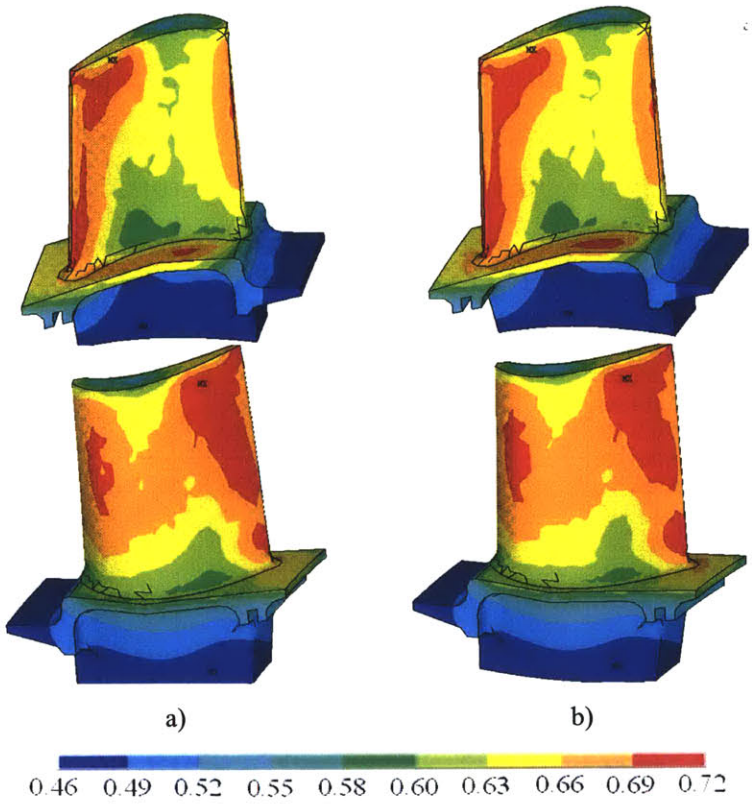

Figure 4.13: Metal temperature distributions on pressure (top) and suction (bottom) side: a) without seal cavity, b) with seal cavity

The location of maximum stress and strain was the same as in the nominal comparisons described in the previous section. The average equivalent stress level was the same in both cases

considered here. The average equivalent strain however was lower by 1.17% in the case without cavity.

The difference in strain resulted in an augmentation of estimated blade life of 2.6% without the seal cavity. It was thus concluded that the 10% – 15% underestimation of heat transfer when not considering the cavity had a small but non-negligible impact on life. Considering the heat transfer and life differences reported in Chapter 3, the results of this study again point at a greater dependence of life on structure than external heat transfer differences.

4.2.2 Effect of Seal Flow

4.2.2.1 Description of Study

The effect of the seal cavity, at nominal seal flow, was the subject of the previous section. The inlet mass flow to the cavity was a small proportion of the main gas path flow (< 0.1%) and a question was whether it was the presence of the cavity or the seal flow that was more important. MHI supplied a range of realistic seal mass flows for the geometry considered, from 0.02% to 0.6% of the main gas path flow. Two simulations were conducted to assess the impact of this range of seal flow. The first was performed with a blocked seal cavity inlet eliminating all seal flow. Due to convergence difficulties at six times nominal seal flow, the high seal flow case was conducted with one half of the specified maximum. In the plots to follow, this case is referred to as Blade 1, Nominal, Hi Seal Flow2. All other boundary conditions were maintained as in the nominal cases.

Results of the study showed that the nominal seal flow provided little in the form of cooling away from the leading edge. Increased seal flow was found to increase the heat transfer to the life-limiting region by as much as 17% yet result in a negligible increase in estimated blade life.

4.2.2.2 Overall Heat Transfer Comparison

Table 4.3 lists the differences in leading edge peak heat transfer from the case with nominal seal

flow. The results confirm that seal flow leaving the cavity cooled the blade leading edge as high as 10% span with maximum cooling occurring closest to the hub.

The flow features and their location in the simulations with nominal and no cavity flow were almost identical. As seen in Figure 4.14, heat transfer differences between these two cases were small (less than 8% everywhere) and localized. There was thus little effect of the nominal seal flow on blade heat transfer.

Spanwise Location	Difference in Leading Edge Peak Heat Transfer	
	No Seal Flow	Hi Seal Flow
5% span	3.8%	-14.6%
10% span	0.7%	-3.2%
25% span	0.1%	-0.03%

Table 4.3: Effect of seal flow on leading edge peak heat transfer.

On the pressure side, a separation bubble followed by flow reattachment and high turbulence resulted in heat transfer increases of 28.2% and 12.5% at S/ARC = -0.11 in Figure 4.14 a) and b) in the case with higher seal flow. Still on the pressure side, between S/ARC ~ -0.7 and S/ARC ~

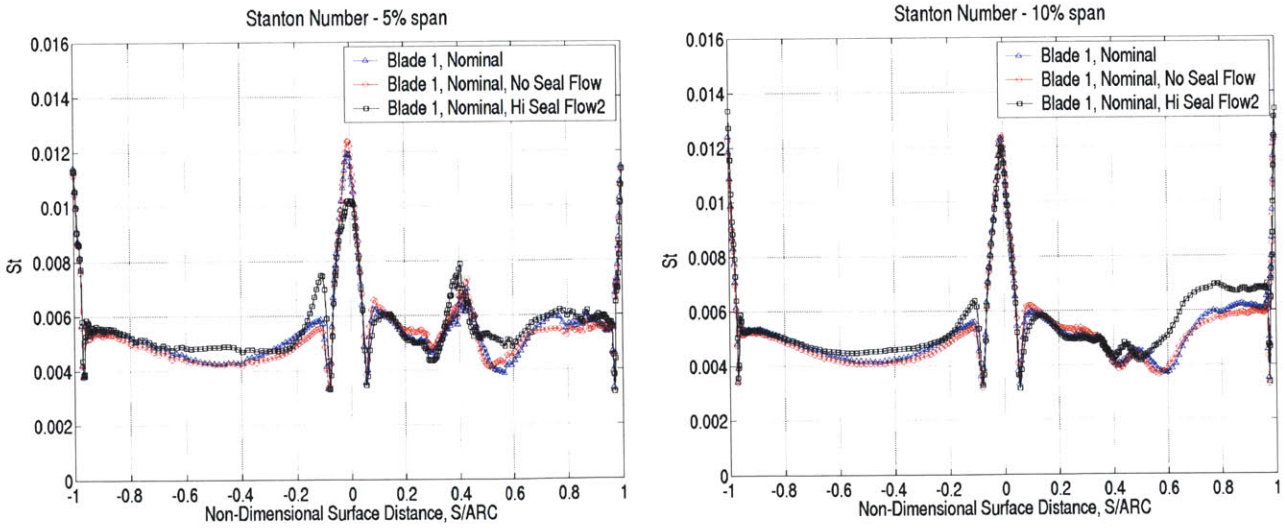

a) b)

Figure 4.14: Effect of seal flow on heat transfer: a) 5% span, b) 10% span.

-0.3, higher heat transfer was obtained for higher seal flow due to stronger secondary flows bringing hot flow down the pressure side towards the hub.

On the suction side, heat transfer differences were consistent with the presence of stronger secondary flows in the case with high seal flow. This case exhibited a stronger pressure side to suction side flow migration associated with larger passage vortex and the corresponding increased suction side impingement heat transfer is shown in Figure 4.14 a) and Figure 4.15. The larger vortex, situated further off the hub, resulted in hot fluid being entrained from the midspan region to the suction side in the latter part of the passage (S/ARC > 0.4 at 10% span). The impact of the increased seal flow was constrained to the first 25% span.

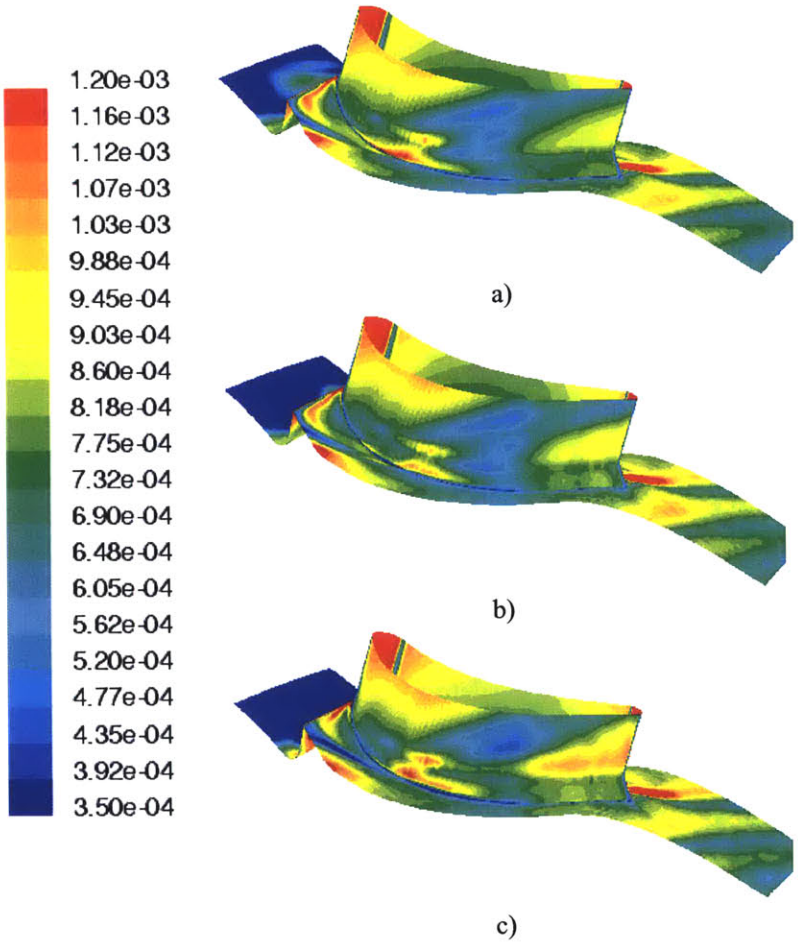

Figure 4.15: Three-dimensional Stanton number contours showing effect of seal flow on heat transfer (blades shown from 0 to 25% span): a) no seal flow, b) nominal seal flow, c) hi seal flow (bottom).

4.2.2.3 Heat Transfer Comparison in Life-Limiting Region

The case with no seal flow resulted in lower heat transfer in the life-limiting region, the differences being less than 3% on the pressure side and less than 6.3% and 5% at 5% and 10% span respectively on the suction side. For the case with high seal flow, differences of less than 2.4% were obtained on the pressure side. On the suction side, the maximum differences from nominal were of 8.5% and 17% at 5% and 10% span respectively.

4.2.2.4 Effect of Seal Flow on Blade Life

The blade metal temperature distributions obtained from the FEM thermal solution are shown in Figure 4.16. The distributions are similar and a hot spot was predicted in the life-limiting region in all cases.

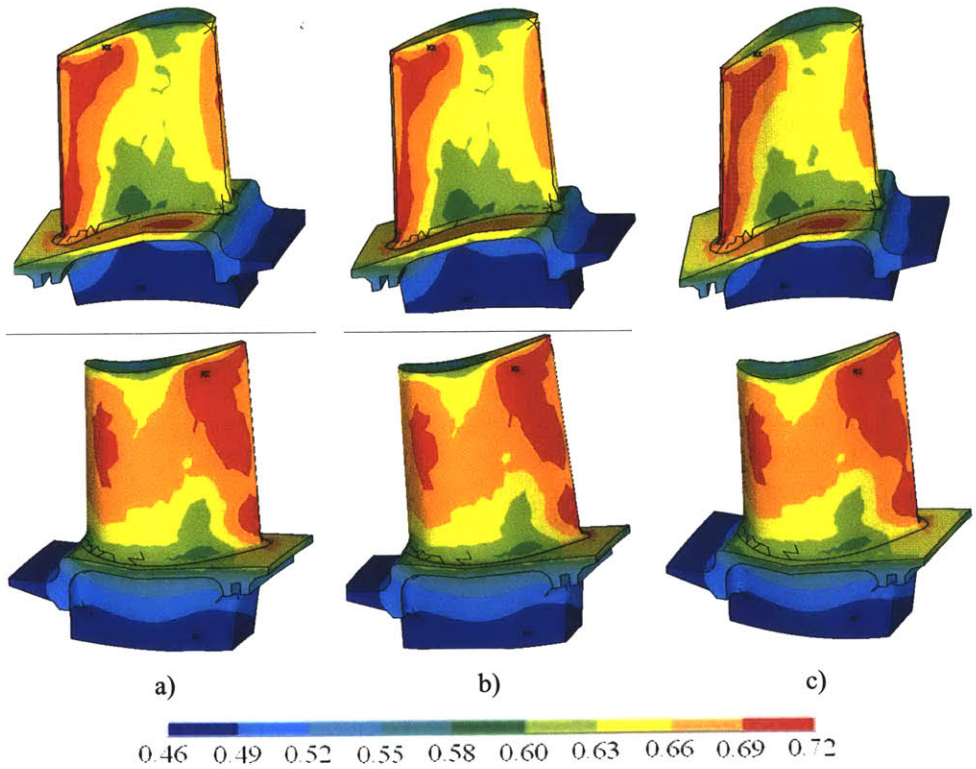

Figure 4.16: Metal temperature distributions on pressure (top) and suction (bottom) side: a) nominal seal flow, b) no seal flow, c) high seal flow.

As in the previous case study, the stress and strain distributions were similar and the location of maximum stress and strain remained the same. The average equivalent stress differences from nominal were negligible at 0.03% and –0.02% of the nominal value for the no seal flow and hi seal flow cases respectively. Average equivalent strain differences of –0.55% and –0.31% relative to nominal were calculated. The lower strain condition in the no seal flow case yielded a 1% increase in blade life and that in the high seal flow case, a negligible increase of 0.7%.

Recalling the CFD results, the impact of the nominal seal flow on heat transfer to the life-limiting region was shown to be small and a negligible impact on life was expected. In contrast, the high seal flow condition was expected to result in decreased life due to the higher heat transfer to the life-limiting region in this case. The results of this study reinforce the fact that external heat transfer plays a minor role in the determination of life and point at limitations in the mapping of the CFD data in the three-dimensional life-limiting region.

4.2.3 Effect of Inlet Boundary Layer with Seal Cavity

4.2.3.1 Description of Study

Endwall boundary layers were not included in the nominal MHI inlet profile. To estimate the heat transfer and life impact of the inlet boundary layer, an additional profile was generated based on the nominal inlet profile and the results of a simulation conducted on the MHI stator. The stator exit circumferentially-averaged total pressure profile was extracted and the near-wall portions were used in generating the new rotor inlet profile. The edges of the boundary layer were determined to be at 6.7% span at the hub and 97.9% span at the casing. Radial equilibrium was maintained in the generation of the new profile. In the freestream region, the total pressure was scaled from the nominal profile values to maintain the same total mass flow to the rotor. The total temperature was maintained as in the nominal profile. Boundary conditions for the seal cavity remained the same as for the nominal blades.

The addition of inlet boundary layers in this case study resulted in similar heat transfer patterns as in the case with inlet boundary layers without cavity in Appendix H2. Due to the already

strong secondary flows in the presence of the seal cavity however, the heat transfer augmentations on the suction side were less prominent in this case. Blade life was actually estimated higher for the case with boundary layers.

4.2.3.2 Overall Heat Transfer Comparison

The inclusion of a hub boundary layer resulted in increased leading edge peak heat transfer as shown in Table 4.4. This was caused by increased cavity flow recirculation entraining hot flow from the main gaspath towards the leading edge-hub junction.

The 61% increase in suction side heat transfer in Figure 4.17 a), was the result of enhanced flow impingement from stronger secondary flows in the case with boundary layer.

Spanwise Location	Difference in Leading Edge Peak Heat Transfer
5% span	2.9%
10% span	1.9%
25% span	1.3%

Table 4.4: Effect of inlet boundary layer with seal cavity on leading edge heat peak transfer.

Over the remainder of the suction surface, the differences were a result of a spanwise shifting of the vortex's migration path up the suction side as shown by the heat flux contours in Figure 4.18. Also shown in Figure 4.18 b) is the heat transfer enhancing effect of hot midspan flow being entrained by the lifting vortex and impinging on the suction side near the trailing edge.

Pressure side differences in this case study were negligible past S/ARC = 0.2 at all spanwise locations. This was due to the presence of strong secondary flows, even without the inlet boundary layers, in the case with cavity. The localized differences near the leading edge at 5% and 10% span were due to higher turbulence intensity associated with flow re-attachment following the larger separation bubble in the case with boundary layers.

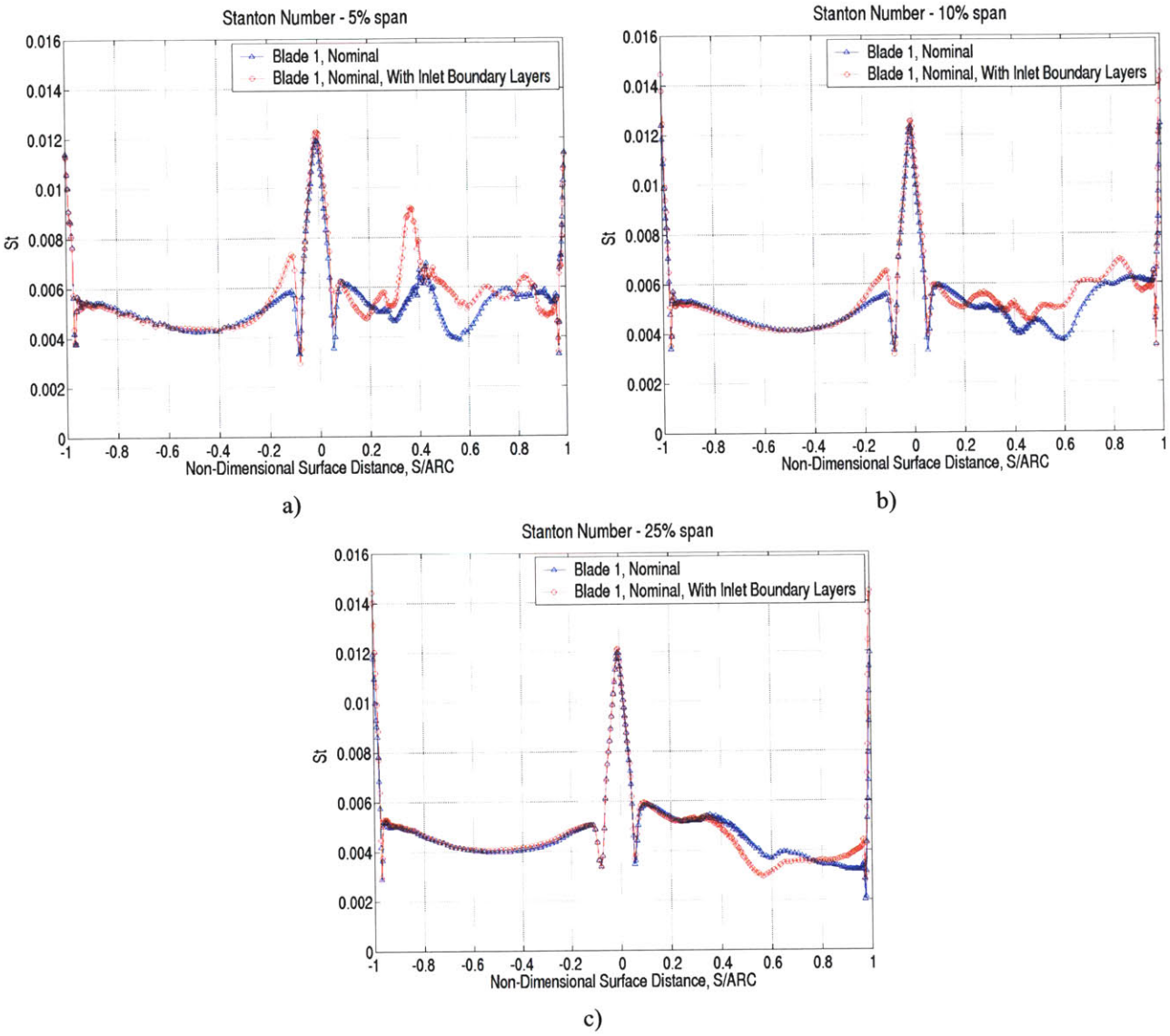

Figure 4.17: Effect of inlet boundary layer with seal cavity on heat transfer: a) 5% span, b) 10% span, c) 25% span.

Above midspan, the casing boundary layer had a similar impact on suction side heat transfer as it did in the case without seal cavity in Appendix H2, decreasing it at 75% span due to colder casing flow migrating down the suction side and increasing it at 90% and 95% span due to secondary flow impingement. The similarity between these results and those in Appendix H2 is not surprising given the effects of the seal cavity documented in section 4.2.1 were shown to be negligible above 25% span.

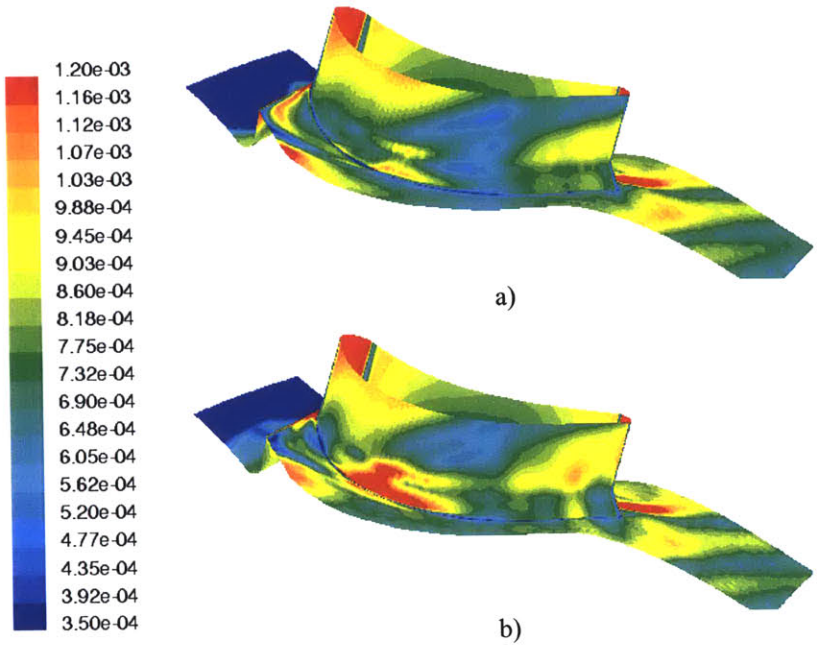

Figure 4.18: Heat flux contours showing effect of secondary flow impingement on suction side heat transfer (blades shown from 0 to 25% span): a) without boundary layer, b) with boundary layer.

4.2.3.3 Heat Transfer Comparison in Life-Limiting Region

In the life-limiting region, pressure side differences in heat transfer were negligibly small with maximum differences of less than 2.2% at 5% and 10% span. On the suction side, heat transfer variations of ±15% were predicted at 5% span. At 10% span, the variations were smaller at -7.1% and +11.4%.

In summary, inlet boundary layers had a similar impact on blade heat transfer with or without seal cavity. However, since the presence of the cavity by itself resulted in stronger secondary flows, the heat transfer enhancing effect of inlet boundary layers was less substantial in the presence of the cavity.

4.2.3.4 Effect of Inlet Boundary Layer with Cavity on Blade Life

Plots of the metal temperature distribution for these two cases are shown in Figure 4.19. The life-limiting region remained a hot spot as in all other case studies and again, the higher

spanwise path of the passage vortex in the case with boundary layers was captured in the FEM calculations.

The stress and strain distributions were once again very similar and the location of maximum stress and strain was consistent with that reported in the other case studies. Average equivalent stress was increased by 0.03% while the average equivalent strain was decreased by 0.45% in the case with boundary layers. This loading condition resulted in an increase in estimated blade life of 0.8%. The over- and under-estimations of the nominal heat transfer in the suction side life-limiting region presented in Section 4.2.3.3 were deemed responsible for the life increase reported here.

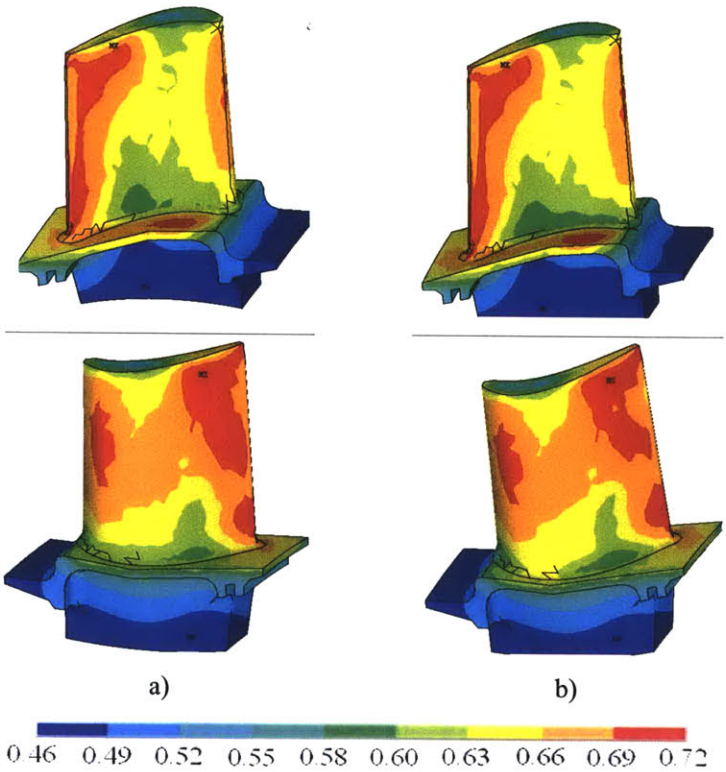

Figure 4.19: Metal temperature distributions on pressure (top) and suction (bottom) side: a) without boundary layer, b) with boundary layer.

Similar case studies investigating the effect of root fillet geometry and inlet boundary layers without the seal cavity are included in Appendix H. The results of these studies, summarized in Table 4.1 were consistent with those presented in this chapter in that differences in external heat transfer due to modeling approximations had a minor impact on life.

5. Concluding Remarks

5.1 Summary and Conclusions

Three different blade geometries plus several modified versions of a baseline geometry were used in a computational study aimed at identifying the impact of aerothermal modeling on turbine blade life.

The CFD part of a computational framework for the end-to-end calculation of blade life was established. Guidelines for the generation of grids appropriate for high-fidelity heat transfer simulations were outlined and used in the development of general turbine grid templates. A survey of available turbulence models was conducted and the v^2-f model selected as best satisfying the modeling and computational needs of the project.

The choice of solver, grid resolution, and turbulence model was verified computationally with benchmark two-dimensional CFD simulations on a high pressure turbine geometry for which past experimental and computational results were available.

Three-dimensional CFD simulations were used to characterize the three-dimensional flow features affecting the blade heat transfer distribution, particularly in the life-limiting region. Secondary flows were shown to be the major players in setting suction side blade heat loads particularly near the suction side shoulder. In the life-limiting region, differences in heat transfer were found to be a result of differences in the strength of these secondary flows. In this region, heat transfer differences between Blades 1 and 2 were less than 5%. For Blade 3, under-estimates of 9.4% were observed on the pressure side and over-estimates of 15% to 24% on the suction side. Based on results of deterministic life calculations conducted in a parallel study [53], it was concluded that blade-to-blade differences in heat transfer played a negligible role in the calculated life differences between the three designs. Rather, as explained in [53], structural differences appeared to be responsible for the 34% and 17% differences in life of Blades 2 and 3 respectively.

Following the deterministic studies, the impact of variability in external convection conditions on blade life sensitivity was identified. The external heat transfer coefficient and convection temperature were shown to exhibit only weak to moderate correlation with blade life variability, the key driver being variability in the internal cooling temperature. Minor differences in absolute variability were found between the designs and as discussed in [53], the Blade 1 design was deemed more robust to variability.

Results of two-dimensional CFD studies on three blade geometries were used to assess the suitability of such calculations for life estimation. Since secondary flows were not captured in these simulations, heat transfer differences (from three-dimensional results) as large as 40% were obtained at the suction side impingement location and as high as 10% – 15% in the life-limiting region. Despite these differences, the results of the two-dimensional studies were used to construct boundary conditions for thermal-structural analyses and proved sufficient to estimate the blade life based on three-dimensional CFD to within 1%. Additional three-dimensional CFD studies were conducted on the Blade 1 geometry to identify the impact of geometric and flow features on external heat transfer and blade life. The features investigated were, the seal cavity, the seal cavity flow, the root fillet geometry, and inlet boundary layers with and without seal cavity. The studies' main conclusions were:

- The seal cavity was found to increase the strength of secondary flows, shift the path of the passage vortex further from the endwall on the suction side, and increase heat transfer below the vortex's path resulting in a 2.6% reduction in life.

- The nominal seal flow was found to provide negligible cooling to the blade. Increased seal flow resulted in pressure side heat transfer differences less than 5% and suction side augmentations as high as 17%. Life calculations for this case showed a negligible increase in life of 0.7% from nominal.

- Inlet boundary layers resulted in a 0.8% increase in blade life. This result pointed at a negative relationship between the cavity and inlet boundary layers.

- The root fillet geometry had negligible impact on blade heat transfer and life.

- The addition of inlet boundary layers to the geometry without cavity resulted in stronger secondary flows, increased heat transfer to the suction side life-limiting region, and a reduction in estimated blade life of 2%.

In summary, in all of the case studies but that of the fillet, the feature under investigation was shown to have an appreciable impact (> ~10%) on heat transfer in the life-limiting region. Similar differences in life were not obtained.

Consolidating the results of all studies conducted in this project, it was concluded that (1) blade-to-blade life differences in designs intended to yield the same work in the same aerothermal environment are primarily structure-driven, (2) differences in external thermal loads due to operational variability, modeling error and/or uncertainty play a minor role in life estimate differences, and (3) so long as the life-limiting region remains the same, simplified CFD studies can be used for reliable estimations of blade life.

5.2 Recommendations for Future Work

In light of the conclusions above, some areas of improvement and future work include:

- The results of the current study could be used in the development of simple design tools for the assessment of the life impact of decisions made early in the design process. Such tools would likely be tailored to every OEM given their nominal baseline design practices. At the time of writing, the first steps in the development of such design tools had been initiated.

- Comparison of thermal, structural, and life results of this study with those from a study using boundary conditions from CFD simulations on a geometry based on the actual CAD model. This would improve the mappability of the CFD results to the thermal model and result in a better transfer of heat transfer trends to the life-limiting region.

- Reduced order study in near-hub trailing edge region. In this study, only a section of the blade would be modeled. A refined FEM grid would be employed and the loads from the current calculations (both thermal and structural) would be employed as boundary conditions. The greater model fidelity and grid resolution in this study would be used to verify the findings of the current study with regards to the drivers of variability and reported weak correlation of external thermal conditions and blade life. Alternatively, given that the life-limiting region is now known, more parameters could be included in the probabilistic study such as detailed cooling slot geometric features. The results of such a study could be used to guide future designs of the life-limiting area.

Appendices

A. Literature Surveys on Grid Generation and Turbulence Modeling for High-Fidelity Heat Transfer Simulations

A1 Gridding Requirements and Selection of Grid Generator

A literature survey was conducted to identify the grid characteristics for high fidelity heat transfer simulations in turbine geometries. A general guideline applicable to the generation of high-fidelity heat transfer grids was defined and the results of the survey were used in the selection of an appropriate grid generator.

Three major grid types, structured, unstructured, and hybrid, are currently in routine use in the analysis of turbomachinery flows [33, 34, 43, 44, 46, 47, 65]. An examination of the literature [27] indicates no consistently preferable grid type for heat transfer applications. Before the results of the literature survey are presented, a brief description of each type is useful.

Structured grids employ regularly ordered hexahedral cells to fill the computational domain (i.e. cells are connected to one another in a pre-specified manner). Single- and multi-block arrangements can be used. Single-block grids treat the computational domain as one volume. These grids are relatively easy to generate but offer little geometric flexibility due to the cell pattern that must be maintained to respect the cell ordering. In multi-block schemes, greater geometric flexibility is achieved by splitting the computational domain into smaller, more conveniently meshed volumes, each of which is meshed with hexahedral elements. The resulting grid consists of conveniently chosen (unstructured) blocks, filled with regularly ordered (structured) cells. A two-dimensional cross-section of a representative multi-block structured grid is shown in Figure A 1. Though not shown here, the third dimension of the grid would be constructed by projecting the surface grid (shown in figure) towards the reader.

For unstructured grids, the surfaces of the computational domain are first meshed using triangular elements. Tetrahedral elements are then grown from these surface meshes until the computational domain is filled. Although there is an increased level of geometric flexibility in the use of unstructured grids, a major drawback is that (compared with hexahedral elements) tetrahedrons do not tolerate high cell aspect ratios. In tetrahedral cells, high aspect ratio translates into high cell skewness which delays, and in severe cases, prevents solution convergence. Thus, by construction, unstructured grids require considerably more cells than structured grids to capture near-wall gradients.

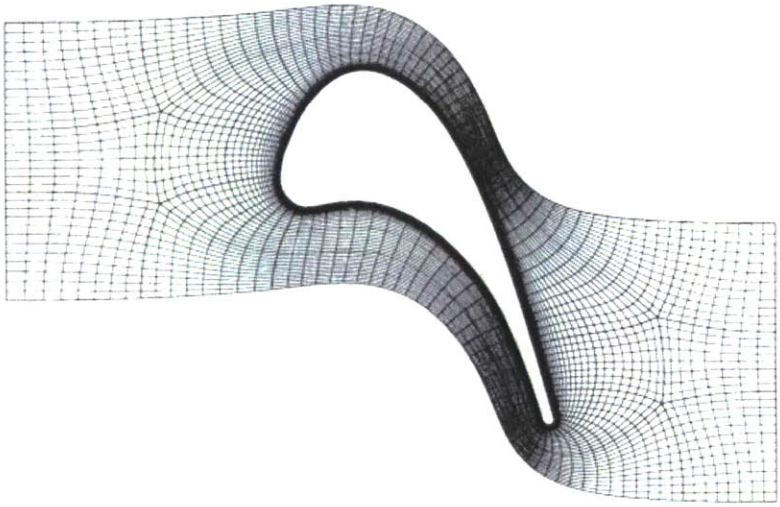

Figure A 1:Two-dimensional cross-section of typical multi-block structured grid [33].

Hybrid grids employ a combination of structured and unstructured approaches. Regions adjacent to solid boundaries such as blade surfaces and endwalls are meshed using blocks of hexahedral or triangular prism elements up to a specified distance from the surface. These cell types can tolerate higher aspect ratios than tetrahedrons, allowing a more efficient capture of near-wall gradients compared with a fully unstructured approach. A layer of transitional elements (quadrangular- or triangular-based pyramids) is then grown on the last layer of prismatic elements in order to interface with the geometrically flexible tetrahedral elements, which are used to fill the remainder of the computational volume.

A1.1 Literature Survey Results

A1.1.1 Near-Wall Grid Resolution

Wall functions offer the potential for significant time savings (30-40% fewer cells in computational grid). However, their use is discouraged for heat transfer predictions [21, 28, 56]. Unlike pressure, temperature varies across the boundary layer and it is these temperature gradients that govern the near-wall heat transfer. In the wall function approach, semi-empirical formulas are used to bridge a region between the wall and the boundary layer outside the viscous sub-layer. As explained in [21], wall functions are not applicable in situations departing from those assumed during their construction, for example, severe pressure gradients, swirling flow, and three-dimensionality in the near-wall region. For turbomachinery simulations, these flow conditions are routinely encountered. In Appendix A2.1 the importance of three-dimensional secondary flows in setting up heat transfer distributions on turbine blades and endwalls will be discussed. Additionally, use of wall functions has resulted in overly diffuse representations of the secondary flows and associated loss cores with the radial extent of the latter being overestimated by about 40% of the experimentally obtained value [46]. Computations on a grid with viscous sub-layer resolution resulted in better agreement with experiments [46]. Based on the results of these studies and the turbulence modeling and grid generation guidelines in [21], wall functions were deemed inappropriate for our intended simulations.

A1.1.2 Near-Wall Grid Stretching

Boyle and Giel [16], established the importance of proper near-wall meshing by comparing the effects of increased streamwise and spanwise grid resolution on blade heat transfer. Table A 1 shows the characteristics of the various grids used in their study[12]. Figure A 2

---

[12] C-type grids were used by Boyle and Giel. The name comes from the fact that the grid adopts a C-shape the close part of the "C" located at the leading edge of the airfoil and the open part forming two parallel grid blocks that extend past the blade trailing edge to the end of the computational domain. For such grids, streamwise cells surround the blade and extend out into the wake. Pitchwise cells extend perpendicular from the blade surface and make up each leg of the "C". Spanwise cells extend from hub to tip.

Grid ID	A	B	C	D	E
Streamwise # of points	214	145	145	145	145
Pitchwise # of points	43	43	43	43	43
Spanwise # of points	43	43	65	65	65
First cell y^+	2.3	2.3	1.2	2.3	2.3

Table A 1: Grid characteristics in grid convergence study [16]

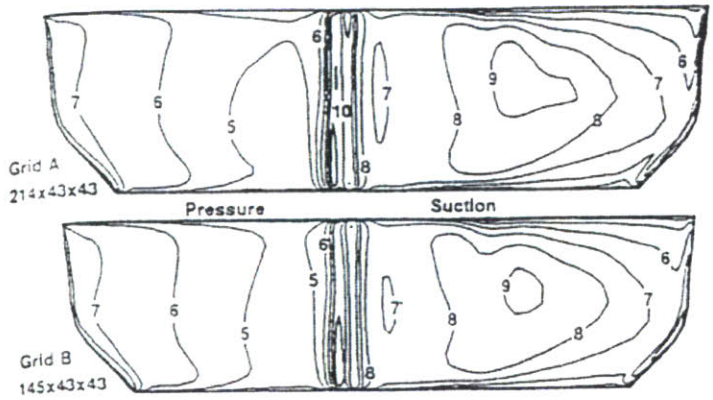

Figure A 2: Effect of streamwise grid density on Stanton number (St x 1000) [16]

shows the effect of varying the streamwise grid density. The Stanton number contours and levels for the two grids are similar even though grid A used almost 40% more streamwise points on the blade surface than grid B (146 vs. 105). Similar agreement was obtained when assessing the effect of non-dimensional first cell height (y^+) as shown in Figure A 3. The

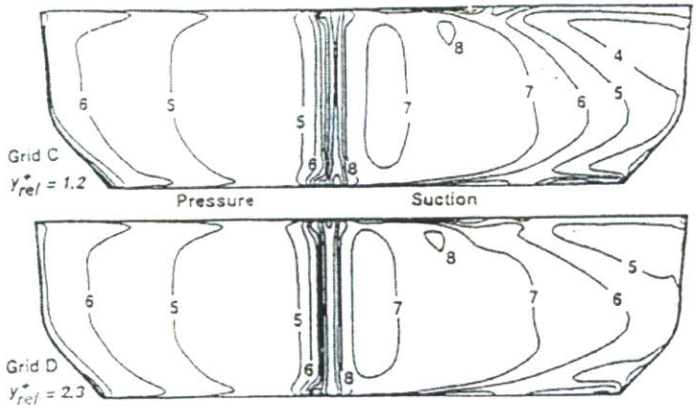

Figure A 3: Effect of first cell y^+ on Stanton number (St x 1000) [16].

effect of varying the spanwise cell stretching (number of spanwise points) is shown in Figure A 4. Differences of 20% to 28% in suction side Stanton number were found above midspan in the aft section of the blade. There is close agreement however, in surface pressure distributions for the same two grids, as illustrated in Figure A 5, indicating the very different sensitivities of heat transfer and pressure; requirements for grid-independent heat transfer simulations are more stringent than those for computations of pressure. More specifically, not

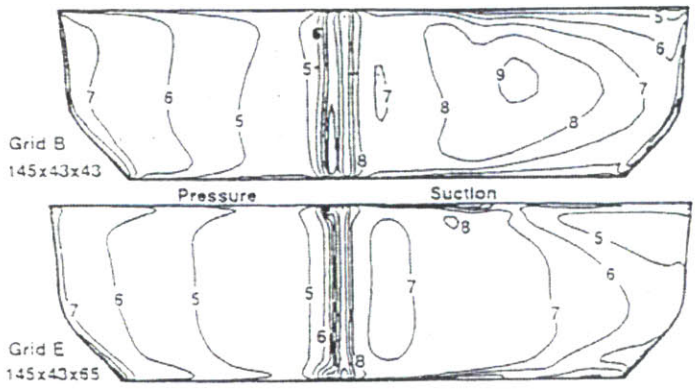

Figure A 4: Effect of spanwise cell stretching on Stanton number (St x 1000) [16].

only must the first cell non-dimensional wall distance be of order unity on both the blade surface and endwalls, but the spanwise stretching ratio, defined as the ratio of the spanwise dimension of one cell compared to that of the adjacent cell, must be maintained at a moderate level, in this case 1.3 for grid E, as opposed to 1.6 for grid B.

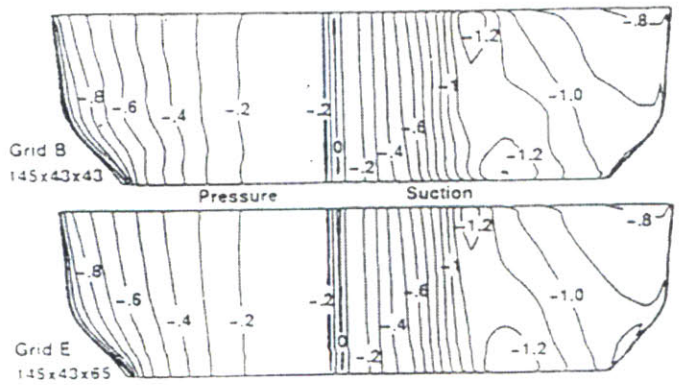

Figure A 5: Effect of spanwise cell stretching on surface pressure coefficient [16].

A1.1.3 Overall Grid Size

Hildebrandt and Fottner investigated the effects of grid density on the ability of numerical simulations to capture the major features of secondary flows and losses [46]. The simulations in [46] were conducted on a linear turbine blade cascade.

In Appendix A2.1 secondary flows will be shown to be responsible for localized heat transfer coefficient gradients in regions identified as critical for durability. Two computational grids, details of which are given in Table A 2, were used in the comparison [46]. For the fine grid calculations, values of y^+ on the solid surfaces (endwalls and blade pressure and suction side) varied between 0.6 and 1.3 whereas for the coarse grid, the range was from 12 to 60, consistent with the use of wall-functions.

	Total # of Grid Points	# of Grid Points in Spanwise Plane	# of Grid Points in Spanwise Direction (half span)
Coarse Grid	303 000	8 200	37
Fine Grid	1 138 000	11 700	97

Table A 2: Grid point distribution used in [46].

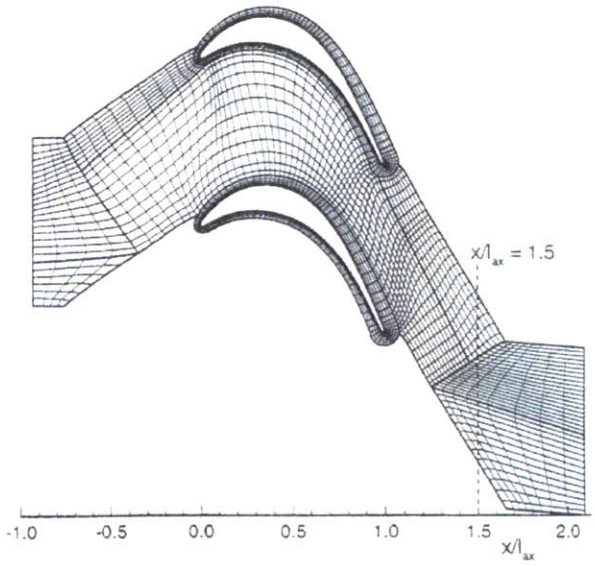

Figure A 6: Two-dimensional cross-section of multi-block grid used in [46] (every other grid point removed for figure clarity).

Computations of pitchwise-averaged loss coefficients on a plane perpendicular to the axial direction (see Figure A 6 labeled x/l_{ax}=1.5) were compared with experimental values. The calculations conducted on the coarse grid gave a loss peak ~25% further up in the spanwise direction and a larger loss core region (~25% span) compared to that obtained from experiments (~20% span). The fine grid calculations captured the radial location of the loss peak as well as the radial spread of the loss core.

Figure A 7 shows contours of local loss coefficient on the same axial plane used to obtain the pitchwise-averaged loss. As is typical of RANS-based calculations [38], the loss levels were

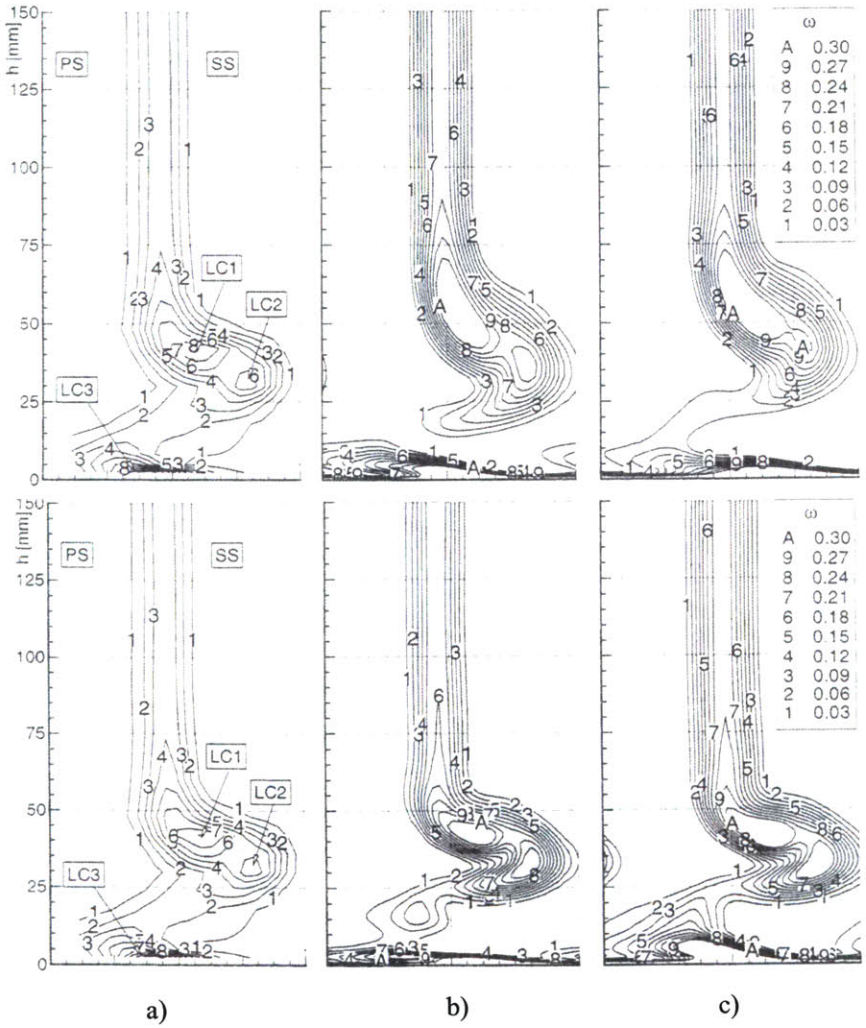

Figure A 7: Effect of grid density on predicted loss coefficient contours: a) experimental data, b) k-ε, coarse grid (top), k-ε, fine grid (bottom), c) k-ω, coarse grid (top), k-ω, fine grid (bottom)[46].

over-estimated on both grids. However, the shape and extent of the loss cores obtained with the fine grid were less diffusive and closer to those obtained experimentally.

Given the results discussed in the previous two sections, namely the requirement for grid resolution down to the wall and a low cell stretching ratio, a computational grid of approximately 10^6 cells is consistent with the requirements for high-fidelity heat transfer simulations.

A1.1.4 Other General Heat Transfer Grid Generation Guidelines

General recommendations for heat transfer grid generation, based on the sources consulted, are listed below. The recommendations provide a guideline for the generation of high-fidelity heat transfer grids.

- A first cell non-dimensional wall distance (y^+) on the order of unity should be used [21, 33, 43, 48, 61, 73].
- Given a maximum first cell non-dimensional wall distance ($y^+_{max} < 2$), a low near-wall cell stretching ratio is better than a reduced first cell y^+ value [46].
- Grid cell stretching values, especially in the high-gradient viscous regions, should be kept between roughly 0.8 and 1.25 to ensure grid smoothness and numerical capture of near-wall gradients [16, 33, 65].
- Grids intended for heat transfer simulations should have on the order of 25-40 grid points within the boundary layers [56].
- 50-100 grid points in the spanwise direction are recommended for half-span simulations intended to accurately represent vortex cores and secondary flows [27, 46].
- Full span grids at least 1 to 2 million cells per blade row should be used for high-fidelity simulation of secondary flow and heat transfer [23, 34, 46, 65].
- In addition to grid resolution and smoothness, grid cell orthogonality (low cell skewness), particularly in the high cell aspect ratio near-wall regions, should be considered because it accelerates solution convergence [46, 65].

A1.2 Additional Grid Considerations for Current Study

Other important considerations for the current investigations were computational efficiency, grid parametrization, and grid reusability. These additional constraints stemmed from the fact that a number of three-dimensional simulations were planned.

It was mentioned in Appendix A1 that the geometric flexibility gained from fully unstructured tetrahedral grids comes at the price of additional grid cells. Hexahedral elements can tolerate much higher aspect ratios than tetrahedral elements before adversely affecting the numerical solution because high aspect ratio directly translates into high skewness for tetrahedral elements. Hexahedral elements are therefore better suited for the efficient gridding of the boundary layers and faster solution convergence.

Rather than develop a new grid for every CFD case considered (approximately 1-2 weeks), an approach was sought that would allow the development of a grid template for a generic turbine rotor blade to which subsequent minor modifications could be made according to the specific geometric characteristics of the blade in question. Such modifications would typically be accomplished in days.

A1.3 Selection of Grid Type and Grid Generator

Highly orthogonal (low cell skewness) structured grids are known to yield less diffusive solutions than unstructured grids [46]. Additionally, the higher tolerance of structured grids to large aspect ratios results in fewer grid cells and hence faster convergence than with unstructured schemes. A structured grid approach was thus adopted. Three types of single-block structured grids are in routine use in turbomachinery CFD applications. Each has strengths and weaknesses.

H-grids are relatively easy to generate, allow simple control of grid density, and allow for easy imposition of periodicity. However, the leading and trailing edges are usually poorly

represented and are often the sites of high skew elements which can cause large truncation errors and even prevent solution convergence [52].

O-grids provide good resolution of the leading and trailing edges as well as the growing boundary layer on the blade surface. Used on their own (i.e. not as part of a multi-block arrangement) however, they result in highly skewed elements near the inlet, outlet, and periodic boundaries, of turbomachinery computational volumes.

C-grids offer good leading edge and wake resolution by construction but become highly skewed near the inlet and periodic boundaries. These grids are more appropriate for far-field simulation of wings and airfoil sections.

To exploit the strengths of these single-block variations of structured grids while minimizing their weaknesses, multi-block structured grids can be generated. The multi-block approach capitalizes on the geometric flexibility of unstructured grids by utilizing an unstructured volume decomposition followed by the structured gridding of the resulting blocks. A simple example is the construction of an O-grid around the blade followed by an H-grid built around the resulting "cylinder". This scheme allows for good boundary layer resolution everywhere around the blade and ensures low skewness levels at the inlet and outlet of the computational domain as well as easy imposition of periodicity. More elaborate multi-block schemes can be generated for situations in which high geometric fidelity is required. Based on their known higher accuracy [46], and their ability to efficiently discretize near-wall regions, a grid generator capable of generating hexahedral elements in a multi-block structured grid was sought.

Grid quality, grid generation time, as well as grid reusability were all considerations during the comparison of three grid generation packages (GridPro[13], Gridgen®[14], and TrueGrid®[15]). All three were capable of generating high-quality multi-block structured grids consistent with

---

[13] GridPro, Program Development Company LLC, 300 Hamilton Avenue, Suite 409, White Plains, NY 10601
[14] Gridgen®, Pointwise, Inc., 213 S. Jennings Ave., Fort Worth, Texas 76104-1107
[15] TrueGrid®, XYZ Scientific Applications, Inc., 1324 Concannon Blvd., Livermore, CA 94550

the requirements found in the literature. However, the level of automation and grid reusability provided by the topology-based approach used in the GridPro grid generator was determined to best satisfy the needs of the project.

A2 Turbulence Modeling Requirements and Selection of Turbulence Model

In recent years, Navier-Stokes solvers have been used to predict heat transfer in problems of external convection, jet impingement, jets in cross-flows (for film cooling), and elaborate internal convection cooling [28, 80] the first of which applies for the work presented here.

A literature survey was conducted to determine a suitable approach for the modeling of turbulence in the turbine environment. The four-equation v^2-f model (see Appendix B) was chosen as best satisfying the needs of the project. During the survey, the v^2-f model was compared against several variants of the two-equation k-ε and k-ω models. Due to their added computational cost and the fact that they have not yet been shown to be a consistently superior approach, Reynolds Stress Models were not considered in the comparison. Similarly DNS and LES did not constitute valid alternatives due to their prohibitively high demand on computational resources. Most of the models compared were either directly available in FLUENT 6 or could be implemented using User-Defined Functions [5].

With regards to turbine heat transfer, important phenomena include, (1) the formation and evolution of secondary flows, (2) the near-wall behavior of turbulent quantities and their relation to heat transfer, and (3) boundary layer transition. Models must be capable of capturing these phenomena in situations involving compressible flows.

A2.1 Formation and Evolution of Secondary Flows

Secondary flows are responsible for the transport of hot fluid to locations such as the blade-endwall junction, the endwalls within the passage and the near-hub suction side shoulder [43]. The resulting combination of strong cross-flows and high-temperature fluid leads to high heat transfer rates and surface temperature gradients in these regions [43, 80].

The formation of the horseshoe vortex at the leading edge of a turbine blade cascade was shown to be responsible for a tripling of the local hub Stanton number from that existing 5% of a chord length upstream [43]. Such gradients in heat transfer coefficient result in localized thermal loads at the leading edge-endwall junction. These experimental results were obtained from a low speed (M_{in} = 0.02), linear cascade at low inlet free-stream turbulence (0.7%).

Based on this information, it was argued [43] that high-fidelity predictions of the flow field associated with the horseshoe and passage vortices were necessary for the prediction of local heat transfer distributions. The turbulence model should thus be capable of capturing the leading edge horseshoe vortex roll-up.

The ability of three turbulence models to predict the location of the horseshoe vortex formation was assessed from simulations for a nozzle guide vane cascade [43]. The models compared were the v^2-f and two versions of the realizable k-ε, one with wall functions and the other without (two-layer formulation). Figure A 8 shows previously obtained

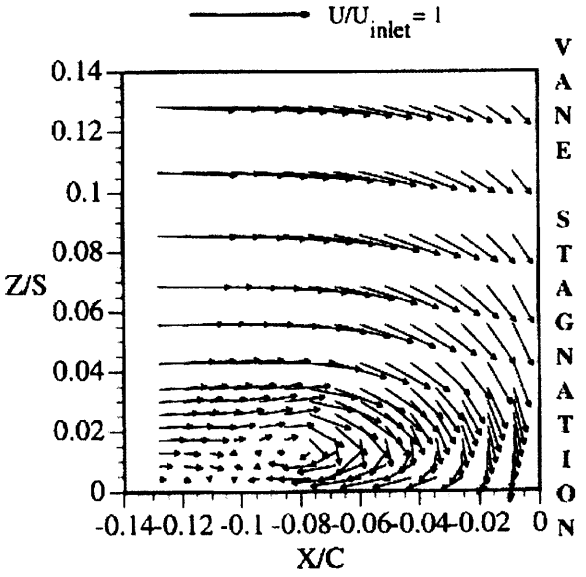

Figure A 8: Experimentally obtained horseshoe vortex rollup in vane stagnation plane [49].

experimental results for the horseshoe vortex roll-up at the leading edge of a vane cascade. The results are presented as velocity vectors in a plane perpendicular to the vane at the

stagnation location [49]. Figure A 9 shows the velocity vector distributions, on the same plane as that used for the experimental results, obtained from calculations with the different turbulence models.

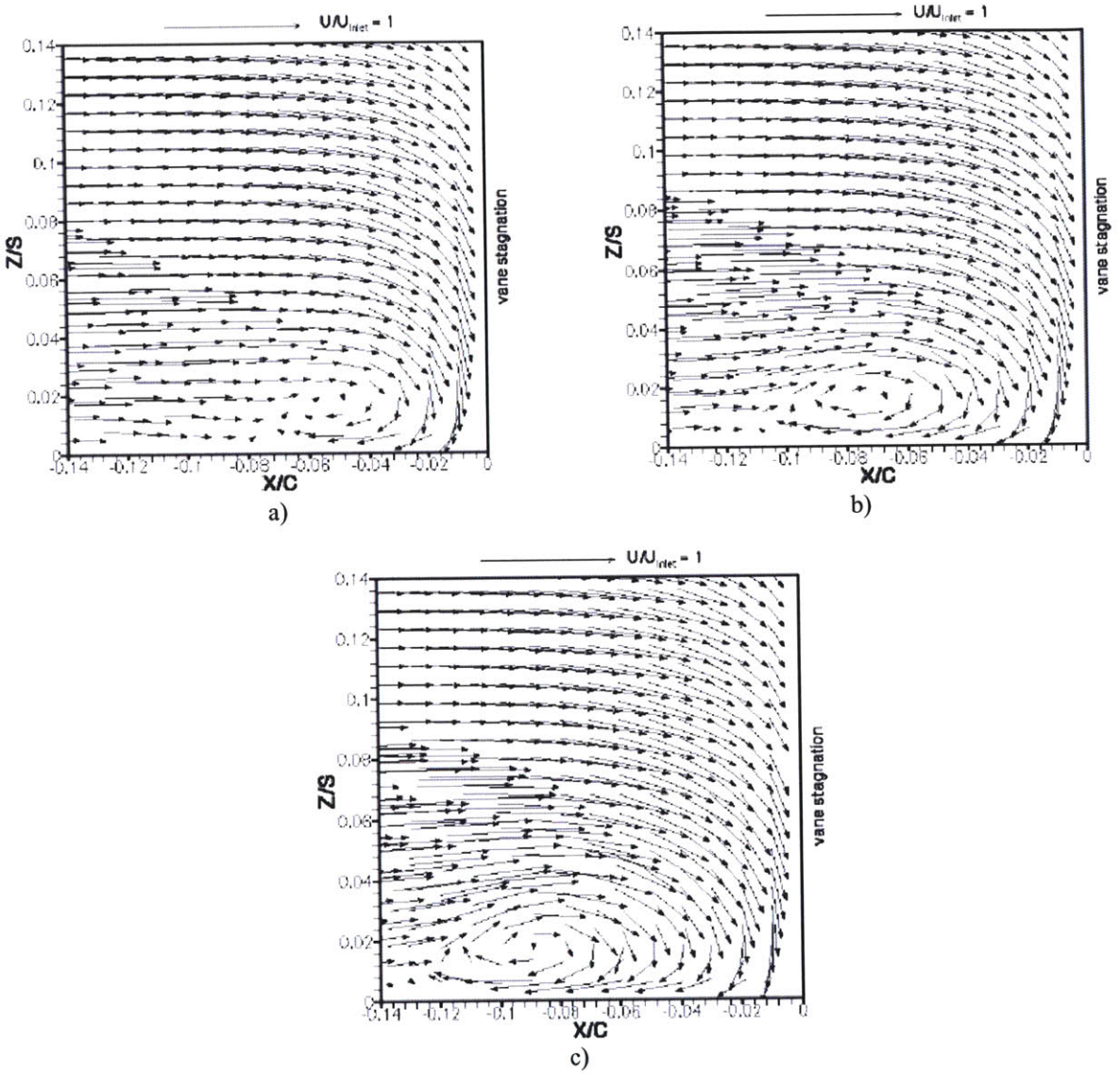

Figure A 9: CFD prediction of horseshoe vortex roll-up in vane stagnation plane using three different turbulence models: a) RKE with wall functions, b) two-layer RKE, c) v^2-f. [43]

Table A 3 shows that the two-layer realizable k-ε model and the v^2-f model capture the location of the leading edge vortex formation better than the standard realizable k-ε model.

	Experiment	RKE (WF)	% Difference	RKE (2-layer)	% Difference	v^2-f	% Difference
Spanwise (z/s)	0.015	0.016	6.7	0.016	6.7	0.016	6.7
Axial (x/c)	0.083	0.05	-39.8	0.076	-8.4	0.088	6.0

Table A 3: Leading edge horseshoe vortex roll-up comparison using two RKE models and one v^2-f turbulence model.

The magnitude of the local velocities associated with the leading edge vortex represents the strength of the leading edge vortex and its ability to carry hot freestream fluid to the blade-endwall junction. As seen by comparing Figure A 8 and Figure A 9, better local velocity agreement between the computations and the experiments was obtained with the v^2-f and two-layer realizable k-ε models than with the standard realizable k-ε model. These results suggest the use of turbulence models that employ grid resolution down to the wall, as opposed to wall functions, for high-fidelity secondary flow predictions, consistent with the findings of Appendix A1.

The effect of secondary flows on heat transfer coefficient distributions is not confined to the near-leading edge region. Figure A 10 demonstrates the heat transfer coefficient distribution

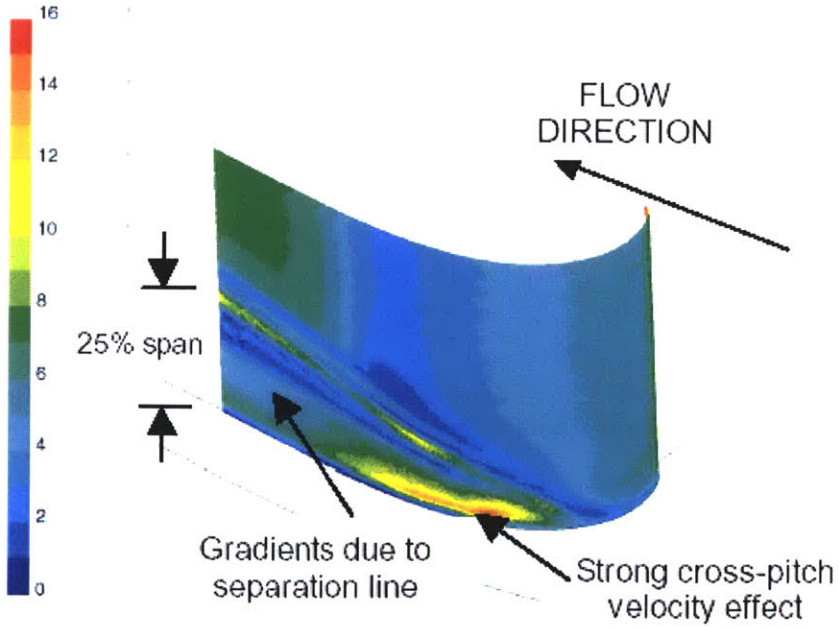

Figure A 10: Effect of secondary flows on rotor suction side Stanton number distribution (St x 1000) [43].

obtained from computations with the v^2-f model on a linear cascade geometry [12]. As indicated in the figure, there is a region of high Stanton number gradients associated with the separation of the passage vortex past the suction side shoulder between the hub and 25% span. Also captured in the simulation was the high heat transfer region at the suction side shoulder resulting from the impingement of the pressure side leg of the horseshoe vortex.

A2.2 Near-Wall Modeling of Turbulent Quantities

It has been shown by a number of investigators that two-equation turbulence models over-estimate leading edge heat transfer coefficients [33, 56, 63]. Over-estimations of nearly 100% for the standard k-ω model were obtained in [63]. Two versions of the k-ε (Launder-Sharma and Chien) and two versions of the k-ω model (standard and transition version) were also shown to over-estimate leading edge heat transfer by nearly 100% [56]. This shortcoming of most two-equation turbulence models is commonly called the "stagnation point anomaly" [8, 30].

The over-estimation is thought to be the result of too high a calculated level of turbulent kinetic energy (TKE) production in the stagnation region [63]. In standard two-equation models, the TKE production (see variable P in Appendix B) is dependent on the square of the magnitude of the strain rate tensor. As the flow approaches the stagnation region of a turbine blade, strain rates normal to the blade surface grow rapidly resulting in high levels of estimated TKE production. Strain rates within turbine passages, away from the leading edge, can also be large enough to cause the problem [63]. The root-cause of the issue is not the presence of the leading edge but the strong dependence of the TKE production on local strain rates [63].

To reduce estimated levels of TKE production, some investigators added a time-scale bound in the definition of the eddy viscosity as

$$\mu_t = C_\mu \rho u^2 T \qquad \text{EA 1}$$

where u^2 is the turbulent velocity scale, C_μ is a model constant, ρ is the density of the fluid, and T is the turbulent time scale [63]. The bound on the time scale is derived from the condition that the eigenvalues of the Reynolds stress tensor should be non-negative. This modification caps the production of TKE in standard two-equation models.

As seen in Figure A 11, in a heat transfer study on a high pressure turbine blade geometry, the Stanton number predictions obtained with the time scale-bound turbulence models are closer to the experimental measurements than those obtained with the standard (unmodified) turbulence models. This was particularly so in the case of the time scale-bound k-ω model where the leading edge Stanton number was estimated to within 7% of the experimentally obtained value. However, pressure side Stanton number levels near the leading edge were still over-estimated by 40% for the modified k-ε and k-ω models and gradients in Stanton number were not well captured in this region. In Figure A 11, the v^2-f model, which incorporates similar upper bounds on the turbulent time scale in its standard formulation, is shown to estimate the stagnation point Stanton number to within 20% of the experimental value and to capture the changes in Stanton number away from the leading edge. This last point is particularly noticeable on the suction side where the other models fail to capture the dip in Stanton number.

The turbulent kinetic energy, k, is related to the turbulence intensity, Tu, as [63]

$$Tu = \sqrt{2k/3} \Big/ \|U\| \qquad \text{EA 2}$$

where $\|U\|$ represents the magnitude of the local mean velocity. Figure A 12 shows distributions of Tu throughout the blade passage for the 5 models considered in [63]. Both time scale-bound models, as well as the v^2-f model, predicted similar distributions of Tu throughout the passage, consistent with experiments [66, 67]. The standard k-ω and k-ε models estimated an increase in Tu levels in the passage resulting in estimated TKE levels on the order of 30 times those obtained with the time scale-bound and v^2-f models. Given the apparent link between over-estimated TKE levels and over-estimations in heat transfer

coefficient, the results of [63] give support for the use of limiters on the TKE production such as used in the modified two-equation and v^2-f models.

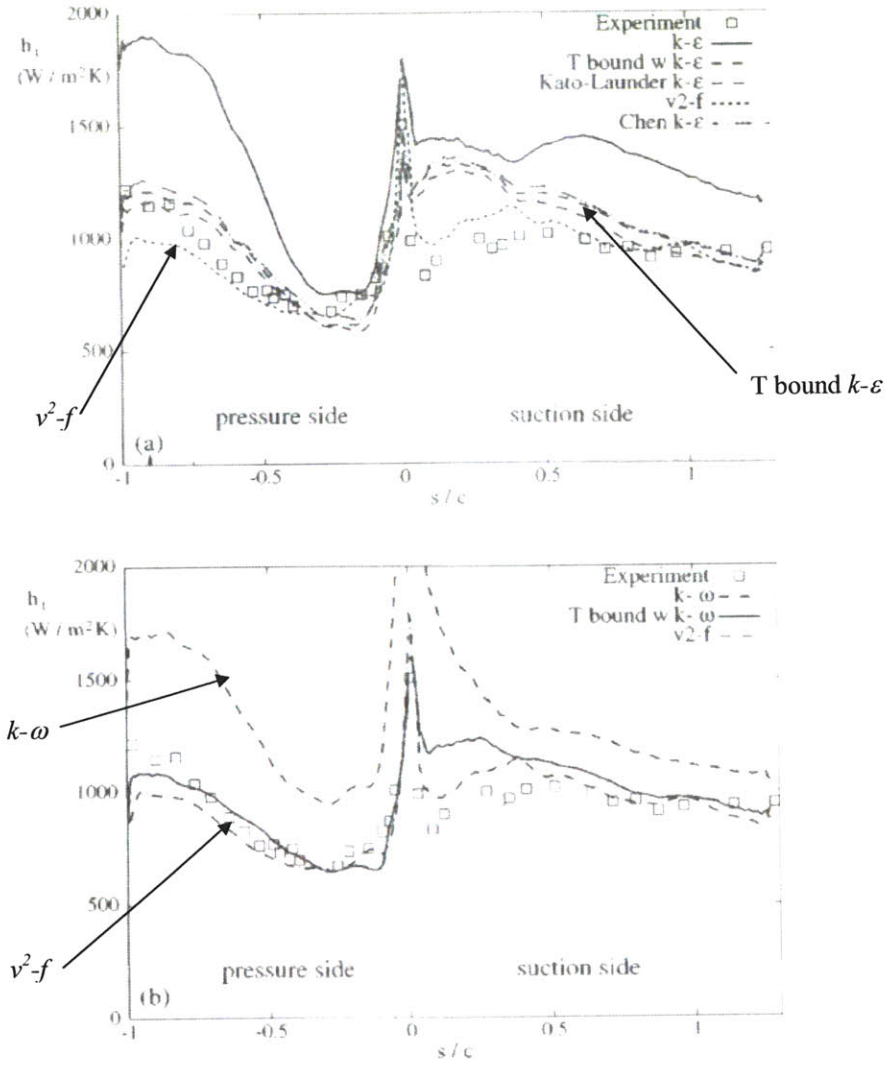

Figure A 11: Two-dimensional heat transfer comparison between experiments and predictions with standard two-equation models, time-scale bound two-equation models, and the standard v^2-f model on a VKI blade geometry [63].

Also important in the modeling of near-wall flow physics is the simulation of the anisotropic behavior of turbulent quantities in this region. The relative success of the v^2-f model in estimating the pitchwise-averaged Stanton number distribution on the vane endwall [43] was attributed to this model's ability to simulate turbulence anisotropy. As the flow approaches an obstacle such as the leading edge of a turbine blade, models incorporating turbulence anisotropy account for the presence of this obstacle by scaling (reducing) the eddy viscosity.

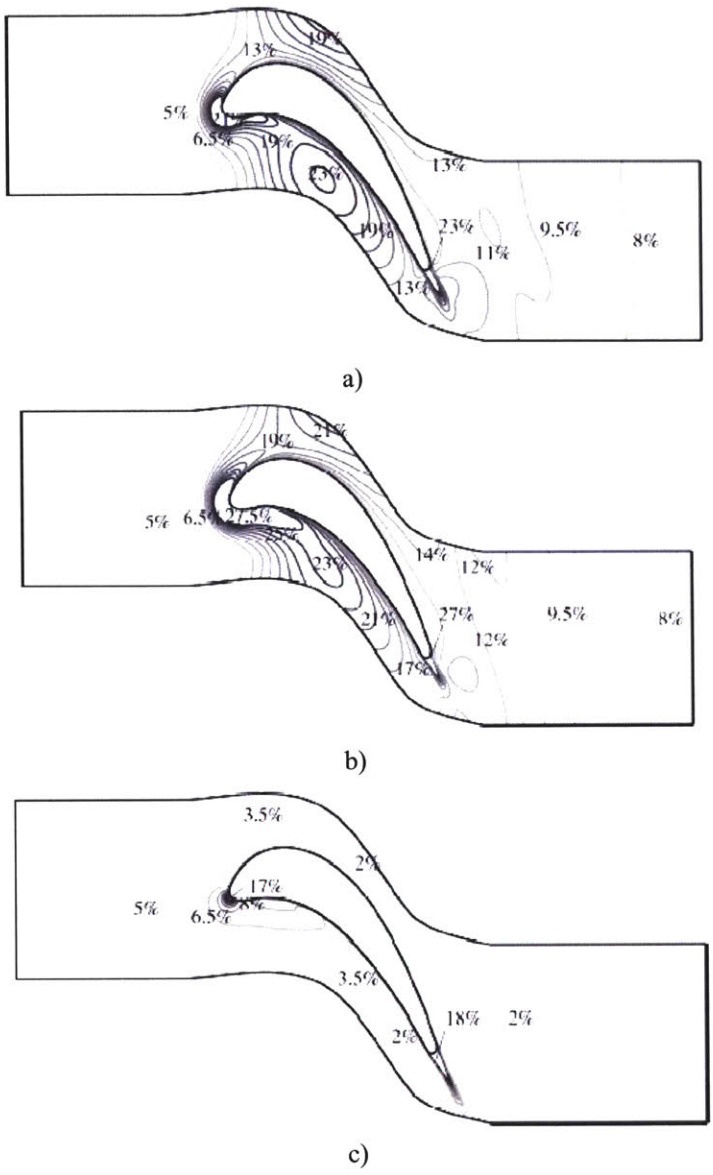

Figure A 12: Effect of limiting TKE production on turbulence intensity distribution: a) standard k-ε model, b) standard k-ω model, c) time scale-bound k-ε model [63].

As seen in Appendix B, a reduction in eddy viscosity results in a reduced level of TKE production which, as mentioned earlier, leads to lower estimated heat transfer coefficients. Low Reynolds number variants of the k-ε model use an empirically determined damping function in the eddy viscosity equation (EA 1) to account for this near-wall reduction in turbulent viscosity. In the v^2-f model, $\overline{v^2}$ is a scalar velocity scale, tending to $\overline{u_n u_n}$ (the average of the square of the wall-normal component of the fluctuating velocity) near any

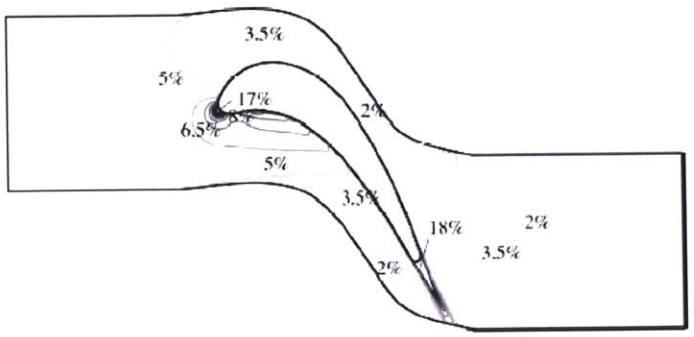

d)

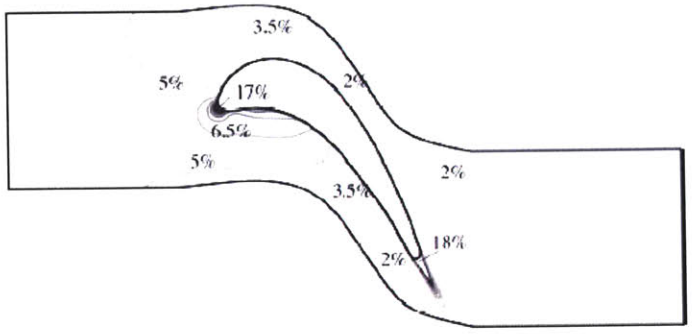

e)

Figure A 12 (continued): Effect of limiting TKE production on turbulence intensity distribution: d) time scale-bound k-ω model, e) v^2-f model [63].

solid wall. This velocity scale provides an estimate of turbulence anisotropy near solid boundaries. (In this thesis, the over-bar on the velocity scale, v, is not used when referring to the v^2-f model.) As seen in Figure A 13, the v^2-f model is more effective at capturing the lower rate of increase in endwall heat transfer in the early part of the passage compared with both of the realizable k-ε models. Similar to the results obtained with the realizable k-ε models, the rate of increase in endwall heat transfer was shown to be over-estimated in calculations employing the RNG (Renormalization Group) variant of the k-ε model in [42].

A2.3 Simulation of Boundary Layer Transition

Boundary layer transition in high-pressure turbines generally occurs as bypass transition during which turbulent spots are directly produced in the boundary layer by the influence of freestream turbulence [62].

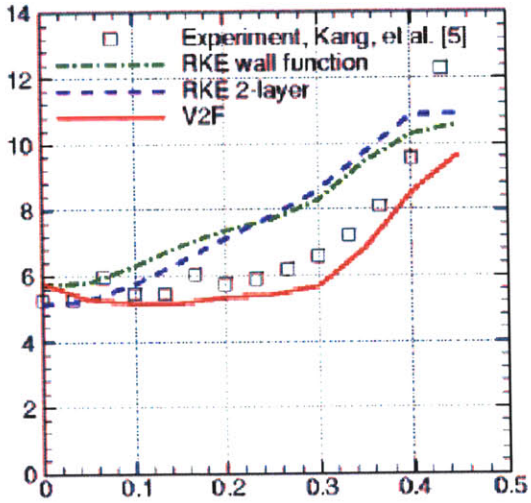

Figure A 13: Comparison of various turbulence model in capturing rate of increase in pitchwise-averaged endwall heat transfer: St x 1000 vs. Non-dimensional axial distance [43]

Since heat transfer coefficients can triple following transition [62], transition location as well as pre- and post-transition heat transfer levels are important in the estimation of thermal loads imposed on turbine blades. The v^2-f model, as implemented in FLUENT 6, does not include an explicit transition model. Nevertheless, as illustrated in Figure A 14, in [43], the v^2-f

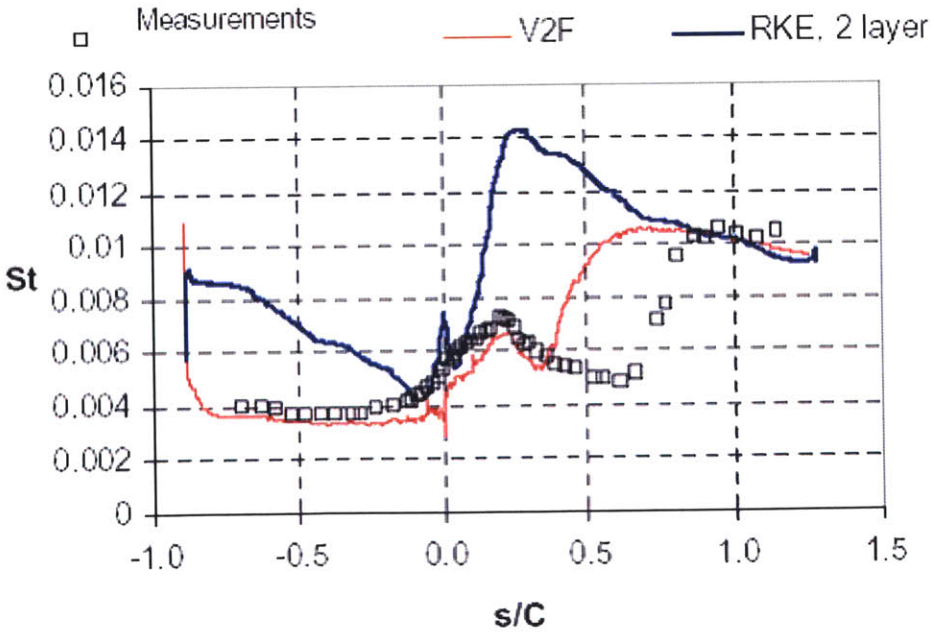

Figure A 14: Comparison of midspan transition prediction using RKE and v^2-f turbulence models [43]

model provided a better estimate of the location of transition than the realizable k-ε model. Further, although the transition location was estimated too early within the blade passage, the pre- and post-transition Stanton number levels were well recovered.

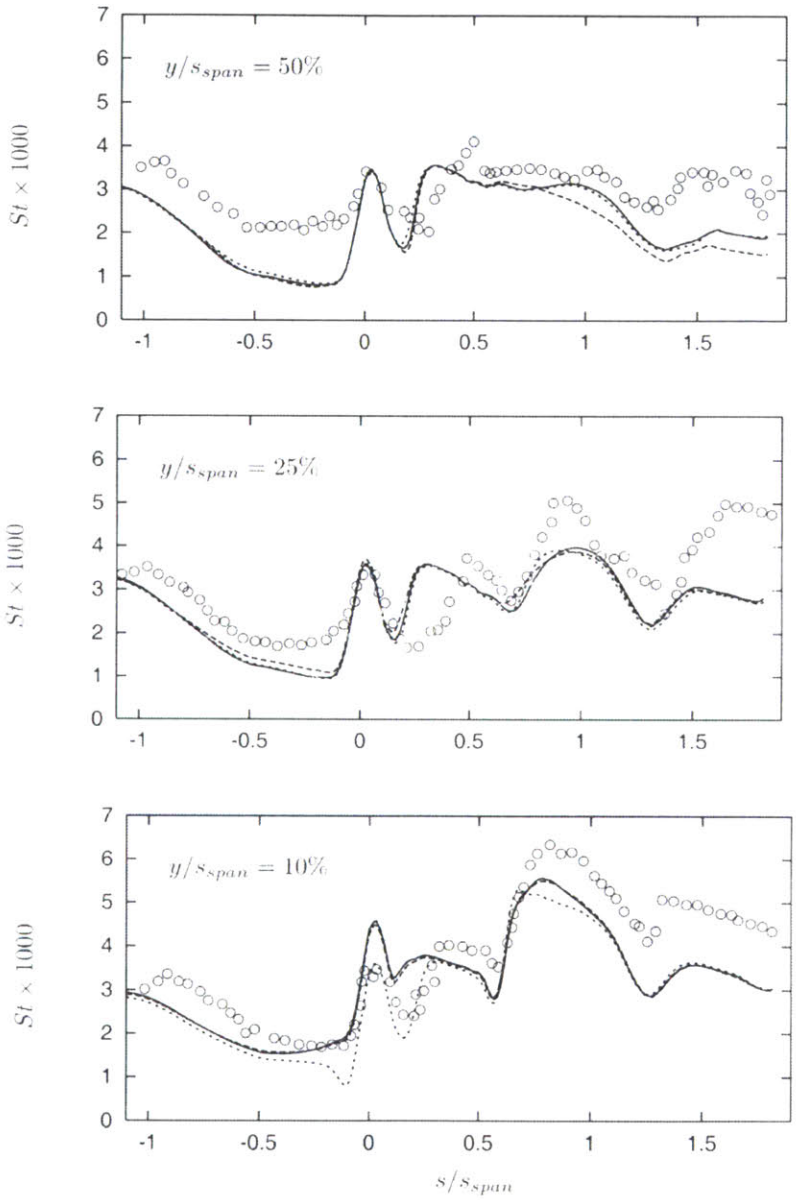

Figure A 15: Stanton number distribution at various spanwise locations in a transonic turbine cascade using the v^2-f model. The solid line and large dashes show results obtained on grids with 52 and 40 spanwise points respectively with a turbulent boundary layer profile imposed on the endwalls at the inlet ($\delta/C_x = 0.24$, where $*$ is the boundary layer thickness and C_x is the axial chord of the blade). The short dashes correspond to the results obtained using the same inlet boundary layer velocity profile but with lower turbulence intensity (uniform inlet Tu = 0.25%). The open circles represent measurements [48]

Another piece of data is shown in Figure A 15. The v^2-f model captured the location of boundary layer transition on a transonic turbine cascade to within about 6% of the total non-dimensional suction surface length [48].

In [59], an argument was made for the use of the v^2-f model for turbomachinery flows in which transition occurred based on LES results in [89], which suggested that the turbulence fluctuation in the wall-normal direction played an important role in the evolution of transition. This wall-normal turbulence fluctuation is the quantity modeled by $\overline{v^2}$ in the v^2-f model.

In [56], the evolution of heat transfer through a subsonic cascade was found to be well simulated by the standard k-ω, transition k-ω and Chien's low Reynolds number k-ε model for the first 80% of the pressure surface length. However, as seen in Figure A 16, a sharp increase in heat flux, not seen in the experiments, was estimated by the same three models in the pressure side trailing edge region. Similar to results obtained in [63], on the suction side, all three models failed to capture the laminar region and associated dip in heat flux downstream of the suction surface stagnation region. The Launder-Sharma low Reynolds number k-ε model captured the laminar region but over-estimated the peak heat flux by about 100% following transition. This model also failed to recover post-transition heat flux levels, the discrepancy between calculation and experiment being on the order of 25%.

As seen in Figure A 17, in the near-hub region, the SST k-ω model was shown to capture both transition location and length but underestimate post-transition suction side Stanton number levels by 26% [10]. Further off the endwall, at 25% span, the transition location was also well captured but pre-transition Stanton numbers were under-estimated by 32%. At 50% span, the model did not capture the sharp transition seen in the experiments and consistently under-estimated the Stanton number values by about 20% to 35 %. As suggested in [20], these under-estimations may be due to the use of an ad-hoc modification in the estimate for TKE production.

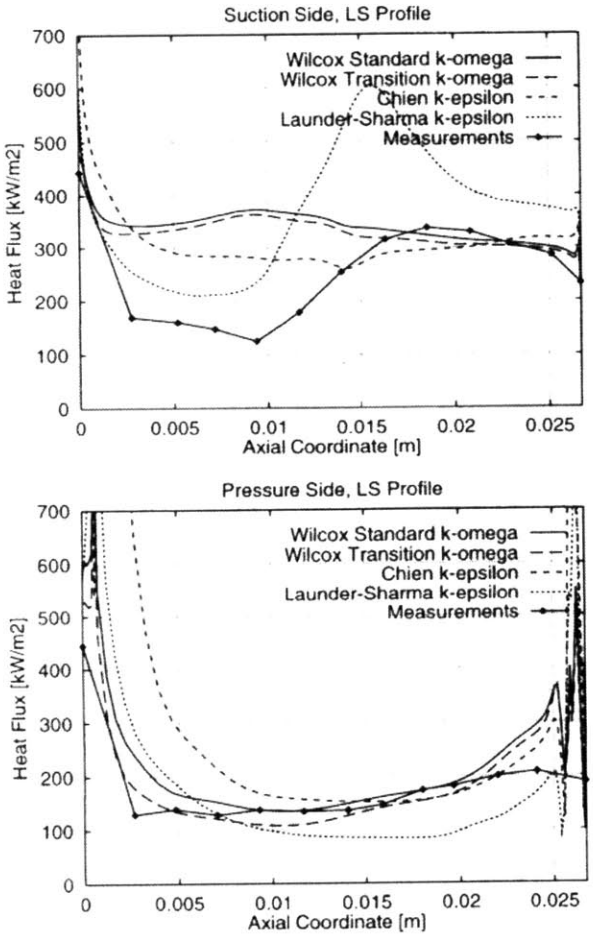

Figure A 16: Heat flux distributions obtained with various turbulence models in a two-dimensional rotor simulation [56]

However, this ad-hoc modification was shown to successfully reduce stagnation region and pressure side Stanton numbers to levels in closer agreement with experimental values as depicted in Figure A 17 and Figure A 18. Therefore, neither of the SST k-ω models employed in this study were capable of capturing the heat transfer levels throughout the entire computational domain but rather, each performed better in a specific region.

In [61], three different low Reynolds number k-ε models were used in simulations for two nozzle guide vane geometries. Chien's model was shown to fail in capturing transition location and associated heat transfer coefficients. The Fan-Lakshminarayana-Barnett (FLB) model captured the suction side transition location and length for both vanes. However the

model failed to capture the gradual increase in heat transfer coefficient towards the pressure side trailing edge. Instead a slow decrease in the first half of the passage followed by a sharp

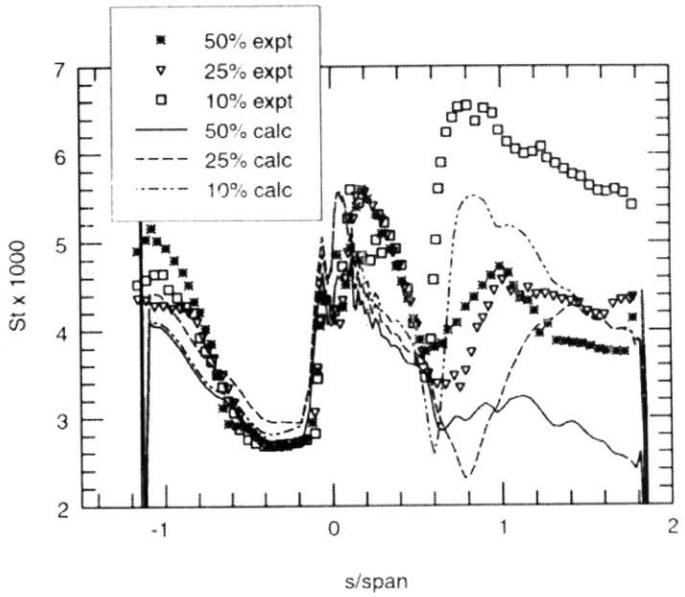

Figure A 17: Stanton number distribution obtained with the modified SST k-ω model at three spanwise locations [33]

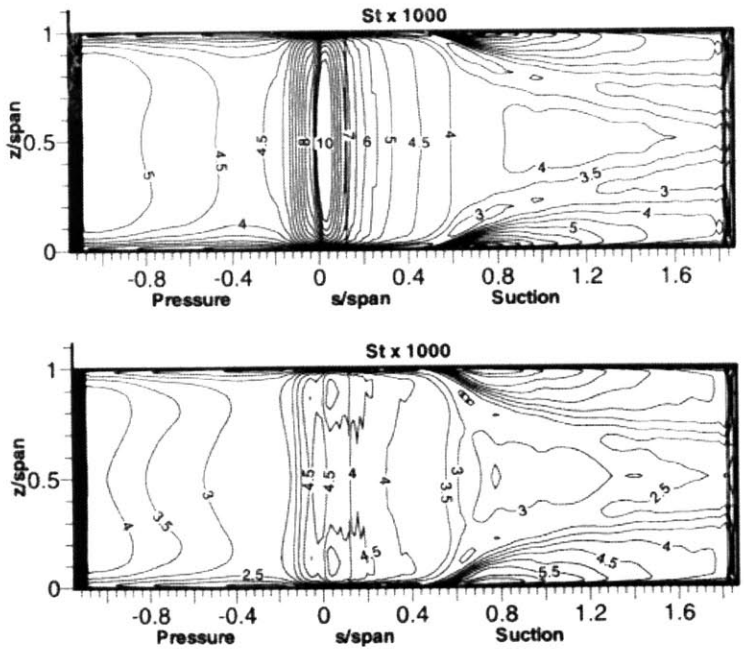

Figure A 18: Stanton number distributions obtained using the SST k-ω model in its un-modified (top) and modified forms (bottom) [33].

increase in the last 20-25% was predicted. For one of the vanes considered, as shown in Figure A 19, the Lam-Bremhorst model was shown to predict earlier transition than the FLB model on the suction side although it captured the gradual pressure side increase in heat transfer accurately. Therefore, among the models investigated in [61], a consistently superior choice was not apparent.

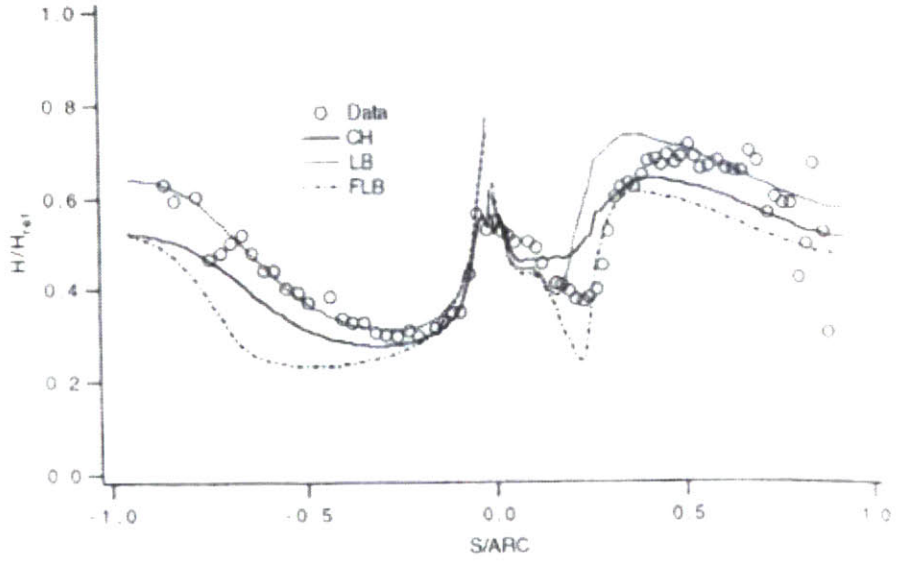

Figure A 19: Two-dimensional nozzle guide vane heat transfer distribution obtained using three different low Reynolds number k-ε models: CH = Chien model, LB = Lam-Bremhorst Model, FLB = Fan-Lakshminarayana-Barnett model [61]

A2.4 Applicability for Compressible Flows

Since the cases considered in this project involve flows approaching sonic conditions, the turbulence model employed should be applicable to compressible flows. Except for [43], all studies compared in the literature survey were conducted in compressible flow situations.

Both [48] and [63] involved heat transfer studies using the v^2-f model for flows well into the transonic regime. The success of the v^2-f model in capturing heat transfer levels in these flow conditions was shown in Figure A 11 [63]. This is further illustrated by comparing endwall heat transfer contours with those obtained from experiments in Figure A 20. Except for a

small region near the pressure side leading edge, the Stanton number levels and contours were well estimated [48].

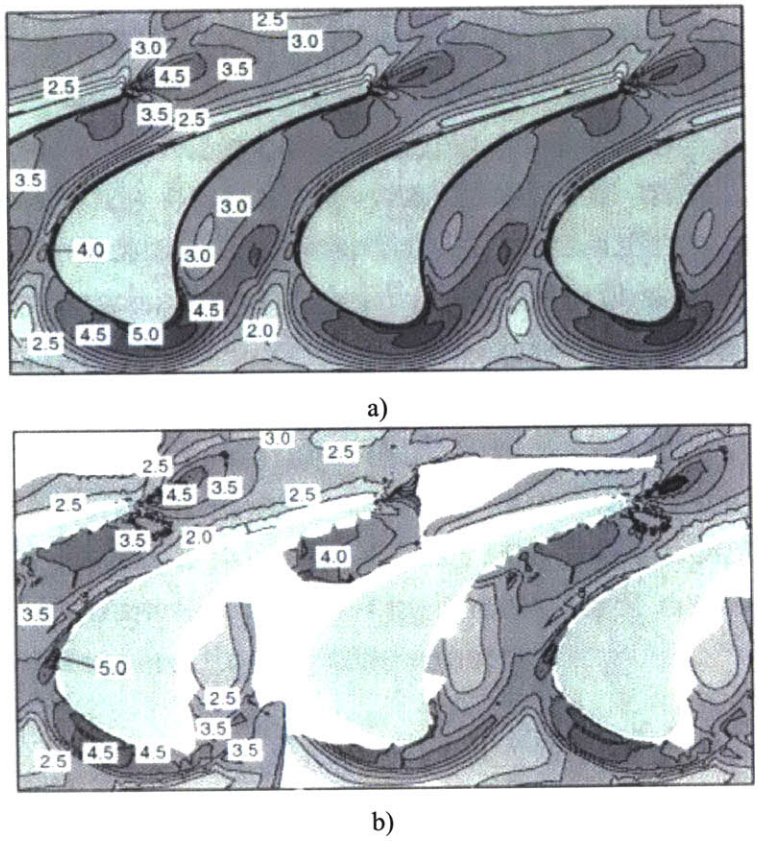

Figure A 20: Stanton number contours obtained from a) computations with the v^2-f turbulence model and b) experiments in transonic flow conditions (St x 1000) [48]

A2.5 Conclusions Concerning Turbulence Model Selection

From the comparative studies, the v^2-f turbulence model was deemed to best meet the needs of the project. The model was shown to be generally superior to the other RANS-based models considered in this study in capturing the relevant flow phenomena including formation and evolution of secondary flow structures in regions susceptible to low durability, near-wall anisotropic behavior of turbulence quantities and their relation to heat transfer coefficient distributions, and boundary layer transition. Its applicability for compressible flows was demonstrated by its capability to describe heat transfer and boundary layer

transition in transonic simulations [48, 63]. The v^2-f model, as implemented in FLUENT 6, was therefore chosen for turbulence modeling in this project.

B. Equations and Constants for v2-f Turbulence Model

(as implemented in FLUENT 6[6, 8, 29, 64])

B1 Equations:

$$\frac{\partial}{\partial t}(\rho k)+\frac{\partial}{\partial x_i}(\rho k u_i)=P-\rho\varepsilon+\frac{\partial}{\partial x_j}\left[\left(\mu+\frac{\mu_t}{\sigma_k}\right)\frac{\partial k}{\partial x_j}\right]+S_k \qquad \text{EA1}$$

$$\frac{\partial}{\partial t}(\rho\varepsilon)+\frac{\partial}{\partial x_i}(\rho\varepsilon u_i)=\frac{C'_{\varepsilon 1}P-C_{\varepsilon 2}\rho\varepsilon}{T}+\frac{\partial}{\partial x_j}\left[\left(\mu+\frac{\mu_t}{\sigma_\varepsilon}\right)\frac{\partial \varepsilon}{\partial x_j}\right]+S_\varepsilon \qquad \text{EA2}$$

$$\frac{\partial}{\partial t}\left(\rho\overline{\upsilon^2}\right)+\frac{\partial}{\partial x_i}\left(\rho\overline{\upsilon^2}u_i\right)=\rho k f-\rho\overline{\upsilon^2}\frac{\varepsilon}{k}+\frac{\partial}{\partial x_j}\left[\left(\mu+\frac{\mu_t}{\sigma_k}\right)\frac{\partial\overline{\upsilon^2}}{\partial x_j}\right]+S_{\overline{\upsilon^2}} \qquad \text{EA3}$$

$$f-L^2\frac{\partial^2 f}{\partial x_j^2}=(C_1-1)\frac{\frac{2}{3}-\overline{\upsilon^2}/k}{T}+C_2\frac{P}{\rho k}+\frac{5\overline{\upsilon^2}/k}{T}+S_f \qquad \text{EA4}$$

where

$$P=2\mu_t S^2 \qquad \text{EA5}$$

$$S^2=S_{ij}S_{ij} \qquad \text{EA6}$$

$$S_{ij}=\frac{1}{2}\left(\frac{\partial u_i}{\partial x_j}+\frac{\partial u_j}{\partial x_i}\right) \qquad \text{EA7}$$

$$\mu_t=\rho C_\mu\overline{\upsilon^2}T \qquad \text{EA8}$$

T and L are turbulent time and length scales defined as,

$$T' = \max\left[\frac{k}{\varepsilon}, 6\sqrt{\frac{\nu}{\varepsilon}}\right] \qquad \text{EA9}$$

$$T = \min\left[T', \frac{\alpha}{\sqrt{3}}\frac{k^{3/2}}{\upsilon^2 C_\mu \sqrt{2S^2}}\right] \qquad \text{EA10}$$

$$L' = \min\left[\frac{k^{3/2}}{\varepsilon}, \frac{1}{\sqrt{3}}\frac{k^{3/2}}{\upsilon^2 C_\mu \sqrt{2S^2}}\right] \qquad \text{EA11}$$

$$L = C_L \max\left[L', C_\eta\left(\frac{\nu^3}{\varepsilon}\right)^{1/4}\right] \qquad \text{EA12}$$

where $\nu = \left(\mu/\rho\right)$ is the kinematic viscosity.

$\alpha, C_1, C_2 C_{\varepsilon 1}, C_{\varepsilon 1}', C_{\varepsilon 2}, C_\eta, C_\mu, C_L$ are model constant. σ_k and σ_ε are the turbulent Prandtl numbers for k and ε respectively and $S_k, S_\varepsilon, S_{\overline{\upsilon^2}}, S_f$ are optional user-defined source terms.

B2 Constants (default values):

$$\alpha = 0.6,\ C_1 = 1.4,\ C_2 = 0.3,\ C_{\varepsilon 1} = 1.4,\ C_{\varepsilon 2} = 1.9,\ C_\eta = 70$$

$$C_\mu = 0.22,\ C_L = 0.23,\ \sigma_k = 1,\ \sigma_\varepsilon = 1.3,\ C_{\varepsilon 1}' = C_{\varepsilon 1}\left(1 + 0.045\sqrt{k/\upsilon^2}\right)$$

C. CFD Solution Process and Case Convergence

All simulations were performed assuming steady conditions. To accelerate case convergence and dampen unsteady effects, an implicit scheme with the default multigrid and under-relaxation parameters was used. The calculations were performed with second-order spatial accuracy.

To alleviate convergence difficulties, three-dimensional cases were initialized and allowed to do 1500 iterations at one quarter of the full wheel speed. During this time a value of 1 was used for the Courant number. Although steady calculations were conducted, an internal time step is used in FLUENT to "march" the solution to convergence. The Courant number controls the size of the time-step taken in every iteration of the calculation. A high value results in longer iterations but faster solution convergence. However, early in the solution process, when gradients can be large, a lower value for the Courant number is recommended to prevent solution divergence. A value of 1 was found to be a good starting point for both two- and three-dimensional cases.

After the first 1500 iterations, wheel speed and Courant number changes were made in the three-dimensional cases according to the schedule in Table C 1.

In most cases, the Courant number was kept constant at 5 until solution convergence. In the rare event of residual stagnation during solution convergence, a further increase in Courant number to as high as 8 was made in an attempt to further decrease the residuals.

Iteration Range	Wheel Speed	Courant Number
1500 – 2000	50%	2
2000 – 2100	75%	3
2100 – 2200	100%	4
2200 +	100%	5

Table C 1: Three-dimensional CFD wheel speed and Courant number schedule.

For the two-dimensional cases, convergence difficulties were rarely encountered and the full wheel speed, translational in this case, could be used from the start with a similar ramping procedure for the Courant number as used in the three-dimensional cases. Between 2500 and 3000 iterations, the Courant number was further increased to 8 until solution convergence.

FLUENT's solution residuals were monitored for case convergence. In three dimensions, when using the v^2-f turbulence model, the following nine residuals are monitored: continuity, x-velocity, y-velocity, z-velocity, energy, turbulent kinetic energy (k), turbulent kinetic energy dissipation rate (ε), velocity variance scale (v^2), and the elliptic relaxation function (f). Inlet and outlet mass flows, total heat transfer to the blade, and heat transfer at spanwise cuts at 10%, 50%, and 90% span were also monitored for solution convergence.

Three-dimensional cases were stopped when all of the following conditions were met:

- All residuals less than 10^{-3}.
- Average mass flow difference from inlet to outlet (including cavity if applicable) less than 0.1% of inlet mass flow.
- Maximum inlet mass flow oscillations less than 0.1% of steady value.
- Maximum exit mass flow oscillations less than 0.5% of steady value.
- Maximum total heat transfer to blade oscillations less than 2% of steady value.
- Maximum heat transfer oscillations at 50% and 90% span less than 2% of steady value.

Requiring maximum heat transfer oscillations to be less than 2% the steady value at 10% span was impossible in 6 of a total of 16 calculations conducted during this project. The steady value was defined as the mean value of the signal monitored during the last 1000 iterations.

D. Effect of Turbulence Intensity on Blade Heat Transfer

To explain heat transfer differences between the three blades, several local quantities were monitored at three locations in the midspan simulations. The locations of interest, shown schematically in Figure D 1 were S/ARC = - 0.4 on the pressure side, S/ARC = 0.4, and S/ARC = 0.72 on the suction side. The quantities monitored included the local isentropic Mach number to assess effects of compressibility [75], shear stress and local skin friction coefficient to test the trends against the analogy between skin friction and heat transfer, the heat transfer driving temperature difference, $(T_{aw} - T_w)$, and the boundary layer turbulence intensity (Figure D 2). The last is included because of its absence in the skin friction analogy and its apparent heat transfer enhancing effect reported in previous studies [9-11, 85].

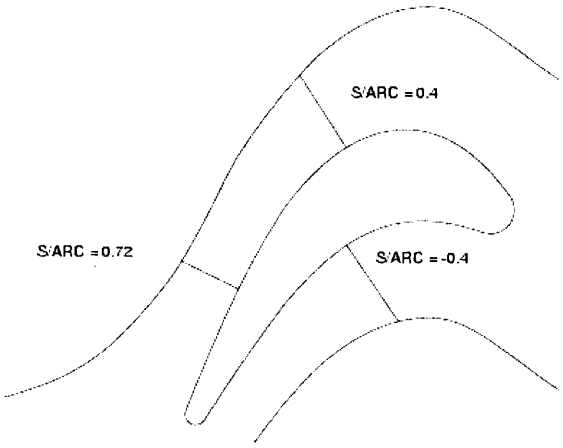

Figure D 1: Blade locations for two-dimensional heat transfer comparison.

As seen in Figure D 2 and Table D 1, at the three locations of interest, only the blade-to-blade trends in near wall turbulence intensity were consistent with the heat transfer differences. Normalized shear stress and normalized heat flux were obtained by dividing by the vane inlet dynamic head and inlet energy flux respectively. The actual values are irrelevant here; the trends were the objective.

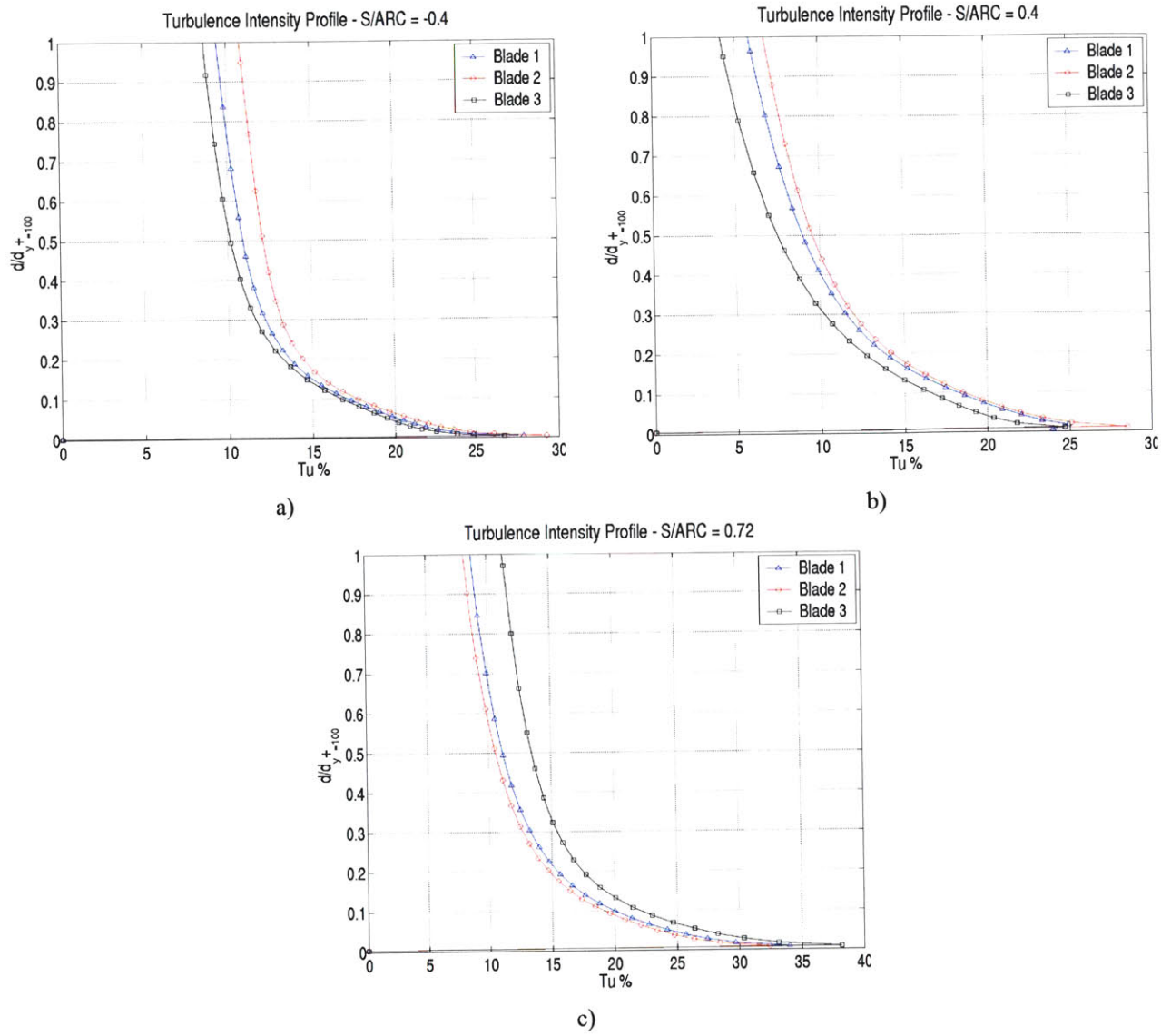

Figure D 2: Two-dimensional, near-wall turbulence intensity distributions at 50% span: a) S/ARC = -0.4, b) S/ARC = 0.4, c) S/ARC = 0.72.

To verify the observed impact of turbulence intensity on heat transfer, additional midspan calculations at different rotor inlet turbulence intensities were conducted and compared against the nominal cases and past flat plate experimental work

In Figure D 3, the heat transfer results of a calculation using 10% inlet turbulence intensity are compared with those obtained using the nominal value of 2.35%. As seen in the figure, the heat transfer effect of such a change is considerable particularly in the stagnation region and on the pressure side. The heat transfer increase is less prominent on the suction side

which is consistent with the previously observed attenuating effect of flow acceleration on turbulence intensity in the three-dimensional stator calculations.

	Normalized Shear Stress	C_f (x 1000)	M_{is}	Normalized Driving Temperature Difference	Normalized Heat Flux (x 1000)
S/ARC = - 0.4					
Blade 1	0.0119	8.343	0.21	0.2437	0.955
Blade 2	0.0127	8.222	0.22	0.2441	1.031
Blade 3	0.0107	8.825	0.19	0.2437	0.882
Correlation	+	–	+	NONE	
S/ARC = 0.4					
Blade 1	0.0729	4.410	0.88	0.2364	1.375
Blade 2	0.0660	4.560	0.79	0.2383	1.465
Blade 3	0.0786	4.140	1.03	0.2339	1.150
Correlation	–	+	–	+	
S/ARC = 0.72					
Blade 1	0.0731	3.795	1.05	0.2339	1.391
Blade 2	0.0746	3.920	1.03	0.2347	1.375
Blade 3	0.0660	3.640	1.03	0.2342	1.517
Correlation	–	–	NONE	NONE	

Table D 1: Trends in quantities monitored for interpretation of two-dimensional heat transfer results.

The impact of turbulence intensity on heat transfer was verified against experimental results. The experiment is described in [10] and the results are plotted in Figure D 4. The flat plate transition location was shown to shift upstream with increasing turbulence intensity. Two-dimensional midspan cases were performed at inlet turbulence intensities of 2.1%, 3.0% and 6.1%. Due to convergence difficulties at inlet turbulence intensities lower than 2%, not all of the cases in [10] could be replicated in the two-dimensional blade calculations[16]. Figure D 5 shows the results obtained on the suction side. The pressure side results are not shown since transition always occurred at the leading edge independent of the level of turbulence intensity. This was due to the presence of a small separation bubble near the leading edge after which the flow reattached in a turbulent state.

[16] Inlet turbulence intensity is quoted using the relative inlet velocity in the denominator of E 2.2.

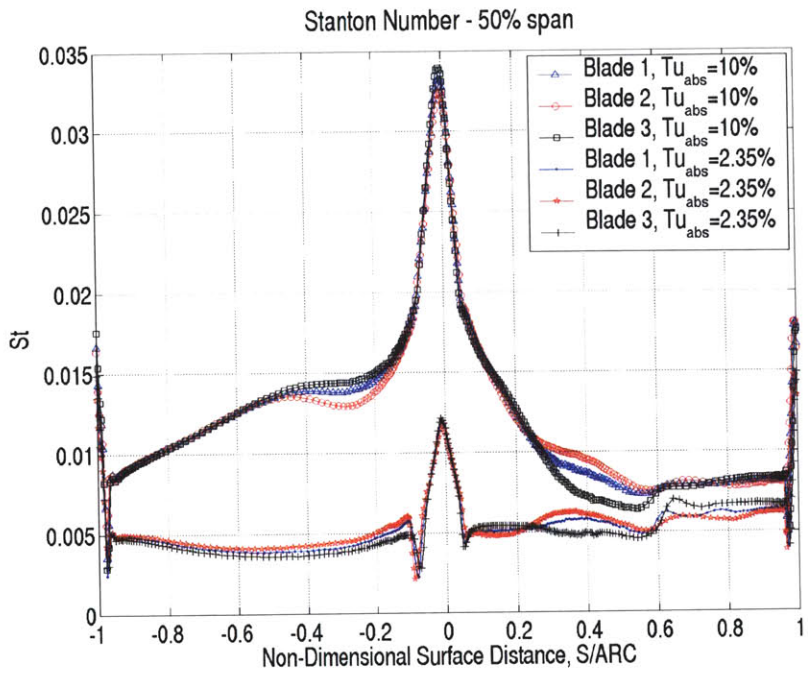

Figure D 3: Effect of inlet turbulence intensity on two-dimensional, 50% span heat transfer.

In Figure D 5, in agreement with Blair's findings in [10], the transition was predicted to occur further upstream and less sharply with increasing inlet turbulence intensity. Good agreement for the transition location as well as pre- and post-transition heat transfer was obtained at 2% turbulence intensity, despite the differences in geometry. Note that the v^2-f

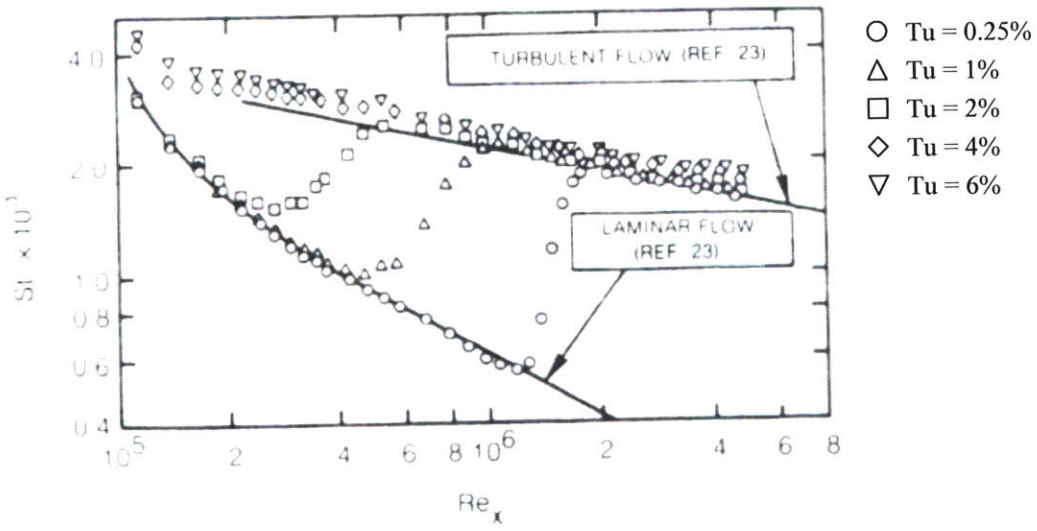

Figure D 4: Effect of turbulence intensity on flat plate heat transfer and transition location [10].

model does not incorporate any transition model but mimicked the phenomenon accurately. Transition was not observed in the nominal MHI cases described earlier since an inlet turbulence intensity based on absolute velocity of 2.35% corresponds to an equivalent value based on relative velocity of 6.3%.

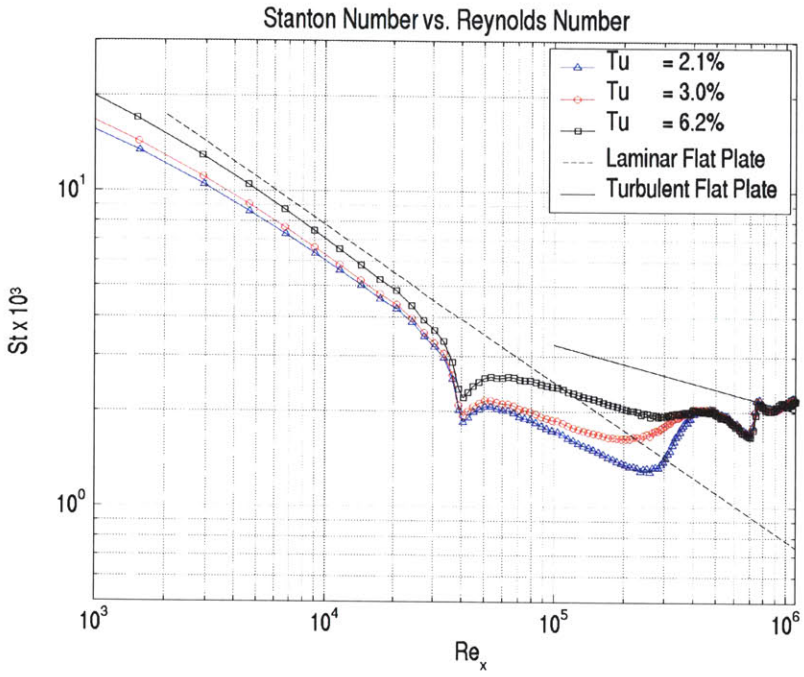

Figure D 5: Effect of freestream turbulence on calculated, 50% span, two-dimensional, suction side heat transfer.

Given this agreement with experimental data in both trends and actual values, the trends observed in the three nominal cases were deemed representative and turbulence intensity was concluded to be a major player in the determination of heat loads on turbine geometries.

E. Calculation of Convection Boundary Conditions

E1 Comparison of Available Methods

This section describes and provides a motivation for the approach used to obtain the heat transfer coefficient throughout this thesis. The preferred approach in the case of a turbine blade with internal cooling is the solution of the conjugate heat transfer problem in which the

external convection, including film cooling, internal convection, and solid conduction problems are solved simultaneously. However, the computational cost of such an approach was deemed impractical for the purposes of this project.

An alternative approach is the so-called 2-Calculation method. This approach, as the name implies, is based on two CFD simulations, one with the domain boundaries assumed adiabatic and the other with them assumed isothermal. The output of this approach is a distribution of heat transfer coefficient and equivalent free-stream temperature which, combined with equivalent internal convection cooling conditions, provide the necessary boundary values for the thermal problem in the blade continuum.

The motivation behind the 2-Calculation approach can be illustrated as in [88] and included here for reference. Starting from the second Crocco-Busemann energy integral (for Pr = 1, dp/dx = 0) for compressible boundary layers,

$$H = h + \frac{U^2}{2} = h_w + (H_e - h_w)\frac{U}{U_e} \qquad \text{EE 1}$$

In EE 1, H represents the total enthalpy. If we let,

$$h = c_p T + const \qquad \text{EE 2}$$

EE 1 becomes

$$T = T_w + \left(T_e + \frac{U_e^2}{2c_p} - T_w \right)\frac{u}{U_e} - \frac{u^2}{2c_p} \qquad \text{EE 3}$$

but,

$$T_e + \frac{U_e^2}{2c_p} = T_{aw} \qquad \text{EE 4}$$

where the subscript "*aw*" refers to adiabatic-wall conditions. EE 3 can thus be rewritten as,

$$T = T_w + (T_{aw} - T_w)\frac{u}{U_e} - \frac{u^2}{2c_p} \qquad \text{EE 5}$$

Invoking the assumption of a Newtonian fluid, differentiation of EE 5 allows us to relate the heat flux and the skin friction as,

$$q_w = k_w\left(\frac{\partial T}{\partial y}\right)_w = \frac{(T_{aw} - T_w)k_w\tau_w}{U_e\mu_w} \qquad \text{EE 6}$$

or, in terms of Stanton number, St and heat transfer coefficient, h_f,

$$S_t = \frac{q_w}{\rho_e U_e c_p (T_{aw} - T_w)} = \frac{C_f}{2P_r} = \frac{h_f}{\rho_e U_e c_p} \qquad \text{EE 7}$$

EE 7 is a form of the Reynolds Analogy and shows that the wall heat flux is governed by the adiabatic wall temperature. It is strictly valid for zero pressure gradient and $P_r = 1$ but, as stated in [88] is a good approximation for gases under both laminar and turbulent arbitrary conditions, particularly if the exponent on the Prandtl number, P_r, is changed from unity to 2/3. In the context of the approach for heat transfer, T_{aw} and q_w would be obtained from adiabatic and isothermal calculations respectively. Assuming that the flow field remains approximately the same for the two calculations, the heat transfer coefficient can then be calculated. The blade surface pressure distributions at mid-span plotted in Figure E 1 are for two such calculations.

For the analysis of many blades, a method employing only one calculation to obtain the wall heat flux, q_w and a good approximation to the adiabatic wall temperature, T_{aw}, would be advantageous. This can be accomplished by using an approach similar to that used in [35] starting with the empirical expression for adiabatic wall temperature,

$$T_{aw} \approx T_e + \frac{rU_e^2}{2c_p} \qquad \text{EE 8}$$

where the recovery factor, r, varies slightly with the Prandtl number as [88]

$$r = P_r^{1/3} \qquad \text{EE 9}$$

This method, referred to as the Recovery Factor method, was compared against the 2-Calculation method on Blade 1 and the mid-span results are shown in Figure E 2. Given the level of agreement between the two approaches, the Recovery Factor method was used for

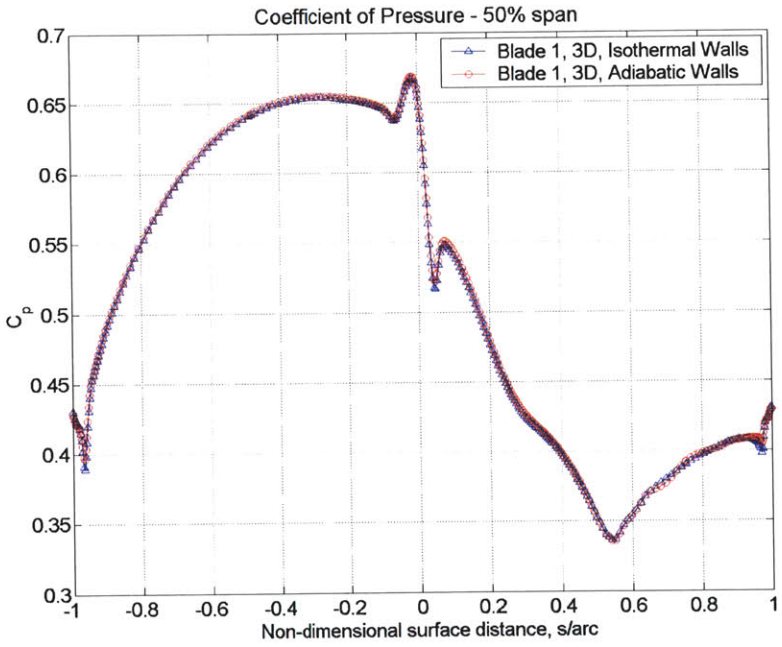

Figure E 1: Two-dimensional pressure distribution with isothermal and adiabatic wall conditions at 50% span.

the generation of all MHI heat transfer coefficient plots in this thesis. The application details for the Recovery Factor Method (RFM) are given in the next section.

E2 Impact of Choice of Recovery Factor Method

In the previous section, the case was made for the use of the adiabatic wall temperature as the heat transfer driving temperature and 50% span calculations showed the RFM to be a good approach to approximate it. This section deals with the impact of using the RFM to approximate the adiabatic wall temperature every along the blade's span.

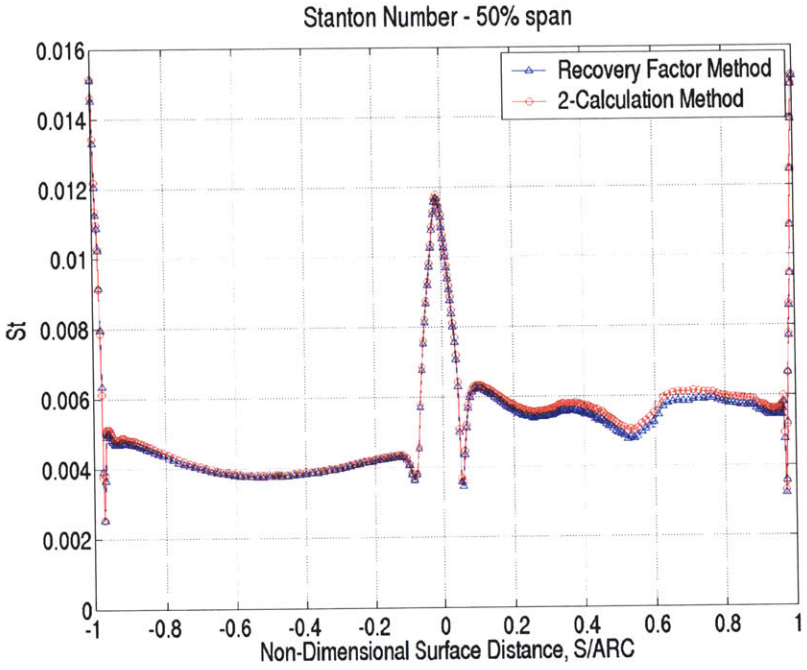

Figure E 2: Two-dimensional heat transfer coefficient comparison using Recovery Factor Method and 2-Calculation Method at 50% span.

In this thesis, the adiabatic wall temperature was estimated from an isothermal calculation as follows. Starting with EE 8 repeated here as,

$$T_{aw} \approx T_e + \frac{rU_e^2}{2c_p} \qquad \text{EE 10}$$

the freestream temperature, T_e, can be written as,

$$T_e = T_T - \frac{U_e^2}{2c_p} \qquad \text{EE 11}$$

The freestream velocity, U_e, in EE 11 can be expressed in terms of isentropic Mach number and freestream temperature as,

$$U_e = M_{is}\sqrt{RT_e\gamma} \qquad \text{EE 12}$$

Another expression for the freestream temperature is,

$$T_e = \frac{T_T}{\left(1+\frac{(\gamma-1)}{2}M_{is}^2\right)} \qquad \text{EE 13}$$

Combining EE 10 through EE 13, the final expression for the adiabatic wall temperature becomes,

$$T_{aw} = T_T\left(1+\frac{(r-1)}{2c_p}\frac{M_{is}^2}{\left(1+\frac{(\gamma-1)}{2}M_{is}^2\right)}\right) \qquad \text{EE 14}$$

where the isentropic Mach number is calculated as,

$$M_{is}^2 = \left(\left(\frac{P_T}{P}\right)^{(\gamma-1)/\gamma} - 1\right)\frac{2}{(\gamma-1)} \qquad \text{EE 15}$$

and the recovery factor, r, as in EE 9.

The above procedure was performed to obtain the adiabatic wall temperature at every point on the blade using the inlet relative total temperature and pressure in EE 14 and EE 15.

Since the inlet relative total quantities varied in the radial direction, the values used at any particular point on the blade was determined as the circumferentially-averaged value existing at the same spanwise location as the point under consideration. This assumption obviously neglects any effects of temperature redistribution and secondary flows.

As shown in Figure E 3 a) and c), due to the presence of secondary flows, the error in the estimation of the adiabatic wall temperature is considerable away from midspan. However, while making an error in T_{aw}, a compensating error is also made in the estimation of the heat transfer coefficient as,

$$h = \frac{q}{(T_{aw} - T_w)} \qquad \text{EE 16}$$

The goal is to define the difference in heat flux supplied to the FEM thermal model compared to that which would be supplied using the 2-Calculation method. The heat flux to the thermal model is not only dependent on the convection conditions obtained from the CFD but on the local wall temperature attained at any point in the thermal solution. To provide a worst case for the error bounding, the difference in heat flux was calculated as,

$$\frac{(q_{RFM} - q_{2-Calc})}{q_{2-Calc}} = \left(\frac{h_{RFM}(T_{aw_{RFM}} - T_{w_{ANSYS}})}{h_{2-Calc}(T_{aw} - T_{w_{ANSYS}})} - 1 \right) \qquad \text{EE 17}$$

over the range of surface temperatures observed in the nominal Blade 1 thermal solution, 0.46 to 0.72 of the vane inlet mass-averaged total temperature. Values for the RMS and worst errors at 7 spanwise locations are listed in Table E 1.

The RMS error incurred in using the Recovery Factor Method is always lower than 11%. Given that the life-limiting region was actually one of the hotter regions in the structural model, the errors potentially affecting the life estimation are more likely to be closer to those shown in the right hand side of the table which, at least for the RMS, are lower than those incurred in the colder regions.

At 5% span, the lower boundary of the defined life-limiting region, the maximum difference reported in Table E 1 was actually located on the trailing edge circle, a location where the CFD data was not mapped due to the presence of the cooling slot here. At 10% span, the worst errors occurred at S/ARC = 0.633 which corresponds to the location where the passage vortex crosses the 10% span line and begins to bring warmer fluid onto the suction side. The worst error in this case was likely due to small calculation-to-calculation differences in the predicted path of the vortex.

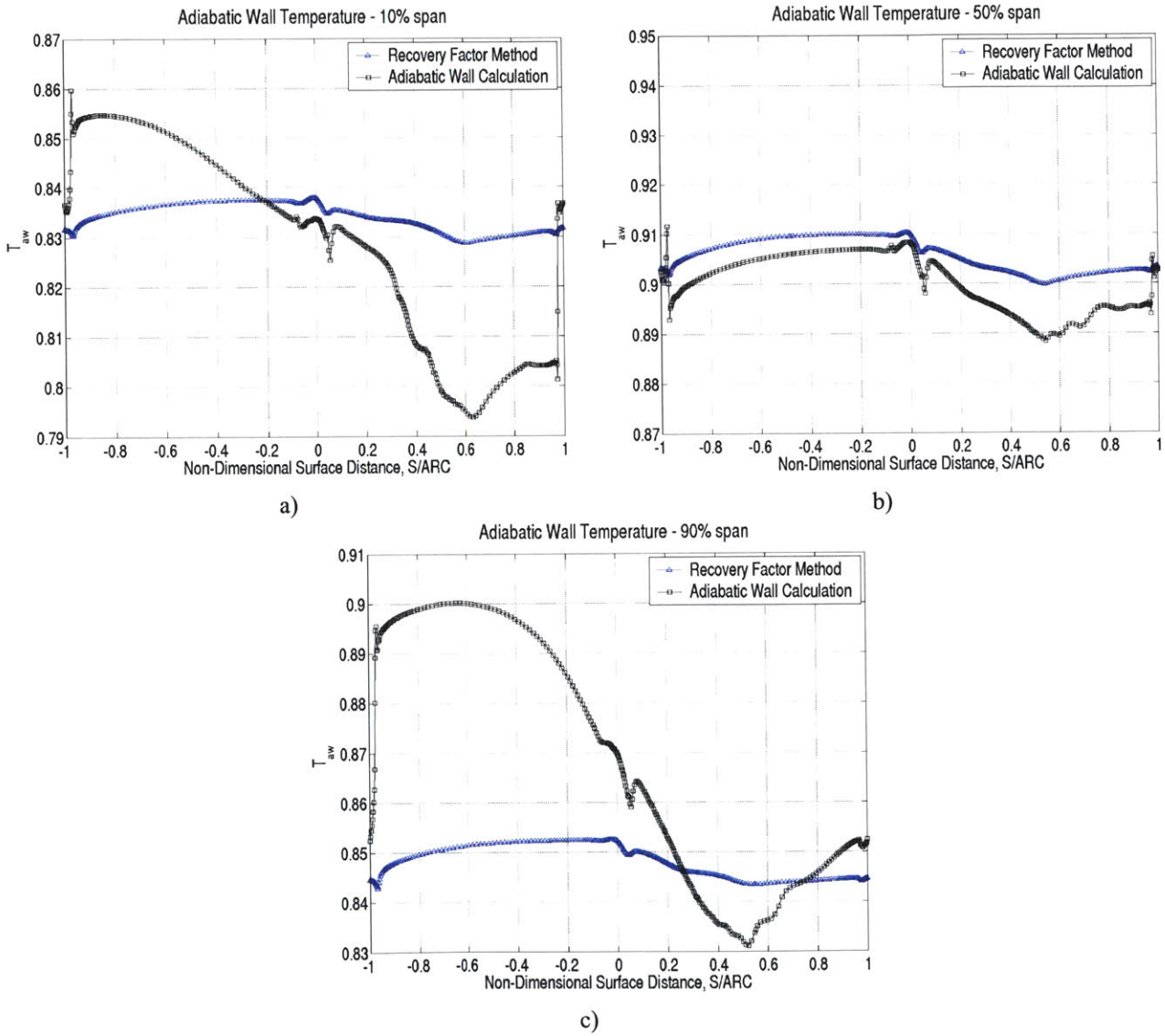

Figure E 3: Comparison of actual adiabatic wall temperature and that estimated using the Recovery Factor Method: a) 10% span, b) 50% span, c) 90% span.

Location	Percent Error in Heat Flux to ANSYS Model			
	Low Wall Temperature (0.46)		High Wall Temperature (0.72)	
	RMS	Worst	RMS	Worst
5% span	5.9	15.4	4.8	-10.5
10% span	7.0	-14.3	4.3	14.7
25% span	8.5	-19.9	7.2	18.2
50% span	1.2	-2.4	0.7	1.4
75% span	4.0	-10.1	2.6	7.1
90% span	7.1	14.7	4.1	-8.3
95% span	11.0	21.8	6.6	-12.4

Table E 1: Heat flux errors (in percent) incurred in using the Recovery Factor Method versus the 2-Calculation Method to provide boundary conditions to the thermal-structural analyses.

In conclusion, based on the low dependence of life calculations on external heat transfer conditions, the Recovery Factor Method was deemed to have been sufficient for the needs of the project.

F. Adjustment of Driving Temperature for Film and Showerhead Cooling

To maintain blade metal temperatures below the allowable maximum in the thermal-structural calculations, as in the real blade, film and showerhead cooling were necessary. As mentioned earlier, film and showerhead cooling were not part of the CFD simulations. Instead, the effects of these cooling schemes were incorporated into the thermal boundary condition file provided to the thermal-structural analyses via a change in heat transfer driving temperature. The temperature modification was accomplished in both cases through the use of a film cooling effectiveness defined as,

$$\eta = \frac{(T_r - T_{rf})}{(T_r - T_c)} \qquad \text{EF 1}$$

where T_r, the recovery temperature, was approximated by what is called the adiabatic wall temperature in this thesis and T_c is the coolant temperature. T_{rf} is the recovery temperature

with film cooling and no other type of cooling present and is the modified heat transfer driving temperature supplied to the thermal-structural calculations.

F1 Trailing Edge Film Cooling

As shown in Figure F 1, the MHI blades have four inclined (streamwise and spanwise) cooling holes in the trailing edge pressure side region. During preliminary thermal-structural calculations without cooling, this region was the site of maximum metal temperature over the allowable limit. Film cooling was required to lower this temperature below allowable limits.

Given that the film cooling hole pitch was approximately 2.5 hole diameters in the streamwise direction, that the holes were angled in the spanwise and streamwise directions, and that the external flow had an important spanwise component in this region (1:4 spanwise to streamwise ratio of velocities), the assumption was made that there was no interaction between the cooling holes. Each cooling hole was thus assumed responsible for cooling a patch of metal of width equal to the streamwise pitch and length equal to the distance between the edge of the cooling hole and the blade tip.

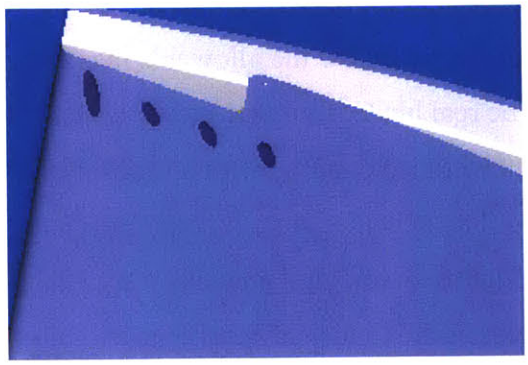

Figure F 1: Trailing edge pressure side near-tip film cooling configuration.

Experimental data were found in [72] for single hole angled injection from a flat plate at various blowing and density ratios. In the trailing edge pressure side region, the blade surface geometry approaches that of a flat plate. The data in [72] consisted of film cooling effectiveness variations with streamwise and pitchwise distance from the hole center. For

our configuration, since the length of the cooled patch was relatively short (1.25 hole diameters from edge of hole to tip), an area-average of the film effectiveness data in [72] at typical blowing and density ratios (0.5 and 1.0 respectively) was constructed by averageing the pitchwise variation in effectiveness at one streamwise location x/D = 1.25 shown in Figure F 2. A more realistic blowing ratio of 1.8 was assumed for the MHI cases and the effectiveness result scaled to yield a final average film cooling effectiveness estimate of 0.374. The coolant temperature used in setting the modified recovery temperature, T_{rf}, in EF 1 was assumed as that of the coolant inside the cooling passages in the tip region.

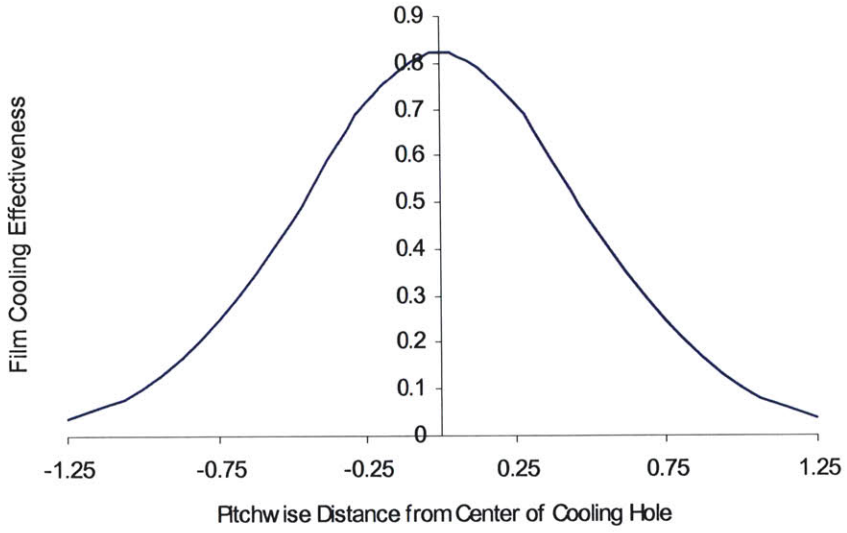

Figure F 2: Single hole angled injection, flat plate film cooling effectiveness distribution as a function of pitchwise distance from center of cooling hole (Blowing Ratio = , Density Ratio = , Streamwise Distance = 1.25 hole diameters) [72].

The modified recovery temperature in this region was successful in reducing the near-tip pressure side trailing edge metal temperature below the allowable maximum.

F2 Tip Film Cooling

On the blade tip, shown in Figure F 3, the heat transfer driving temperature obtained from the three-dimensional CFD calculations was only used in the region upstream of the leading edge cooling passage exit. Between the exits of leading edge midbody cooling passages, a

constant temperature equal to that of the coolant exiting the leading edge passage was used. Downstream of the midbody passage exit, the coolant temperature exiting that passage was used. This choice of temperature was supported by the following points:

- Though not modeled in the CFD analyses, the actual blades have a "crown" around the tip. As shown in Figure F 3, the only portion of this "crown" open to the main gas path is on the pressure side near the trailing edge where the spanwise-inclined film cooling is implemented.
- Modeling errors can be tolerated in the tip region since it is far from the identified low-durability region.

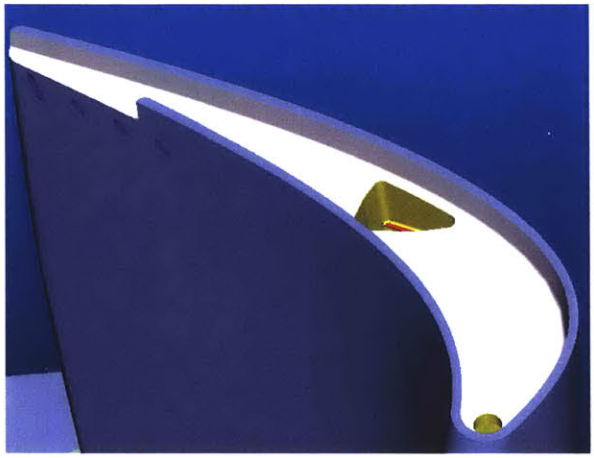

Figure F 3: Tip crown and internal cooling passage outlets.

This tip cooling arrangement reduced the blade tip metal temperature to below the allowable maximum. Coupled with the pressure side film cooling, the tip film cooling shifted the highest metal temperature to the blade leading edge for which showerhead cooling was included as described next.

F3 Leading Edge Showerhead Cooling

For the showerhead cooling scheme, very few past experimental studies were found with a cooling scheme similar to the one used in the MHI blades. An estimate for the film cooling effectiveness, η, was obtained from experiments conducted with five cooling rows at the

leading edge of a cylinder in [69]. As shown in Figure F 4, the MHI blades have three rows of inclined cylindrical holes at the rotor leading edge.

Figure F 4: Leading edge showerhead cooling configuration.

In [69], plots of spanwise-averaged cylindrical hole showerhead cooling effectiveness showed that this quantity did not depend strongly on the blowing and momentum ratios, F and I, when these two values were above 1.0 and 0.6 respectively. Estimated values for F and I for the MHI blades were in the ranges of 1.4 to 2.62 and 1.0 to 4.0 respectively. The effectiveness was therefore not scaled with regards to these parameters. The leading edge passage coolant temperature was provided at three spanwise locations by MHI. The coolant temperature variation in the spanwise direction was taken into account in EF 1 by assuming a linear coolant temperature variation between these three locations.

A stepwise distribution of effectiveness as a function of distance from leading edge was generated based on the experiments mentioned above. Since the experiments did not consider locations more than 14 hole diameters downstream, the latter portion of the distribution was assumed and made to smoothly decrease to nil at 23 hole diameters from the

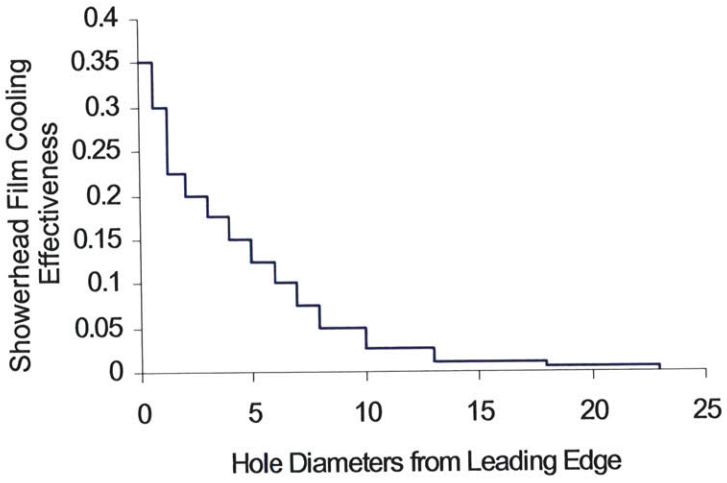

Figure F 5: Showerhead film cooling effectiveness distribution.

leading edge. The distribution is shown in Figure F 5. The resulting heat transfer driving temperature distribution compared with that without film and showerhead cooling is shown in Figure F 6. The maximum metal temperature at the leading edge was reduced to below the allowable maximum using this cooling scheme. The addition of cooling at the leading edge, tip and pressure side trailing edge was successful in reducing blade metal temperatures below the allowable maximum.

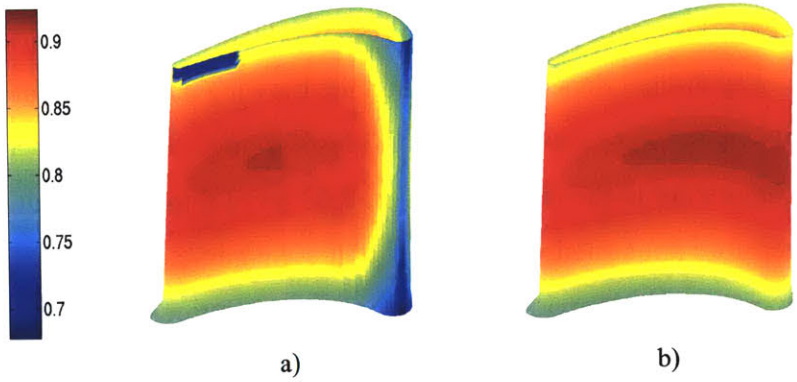

Figure F 6: Heat transfer driving temperature: a) with film and showerhead cooling, b) without cooling.

G. Grid Convergence Study

To study the impact of finite grid resolution on the heat transfer and life calculations, a

refined grid was generated for the nominal blade. In the interests of maintaining computational efficiency while capturing the potential impact of grid resolution on blade life, the grid refinement was localized in the near-hub region. Specifically, the number of spanwise cells was doubled between 0 and 10% span. The resulting grid was identical in topology to the original but with the total number of cells increased from 1.5 million to 2.1 million.

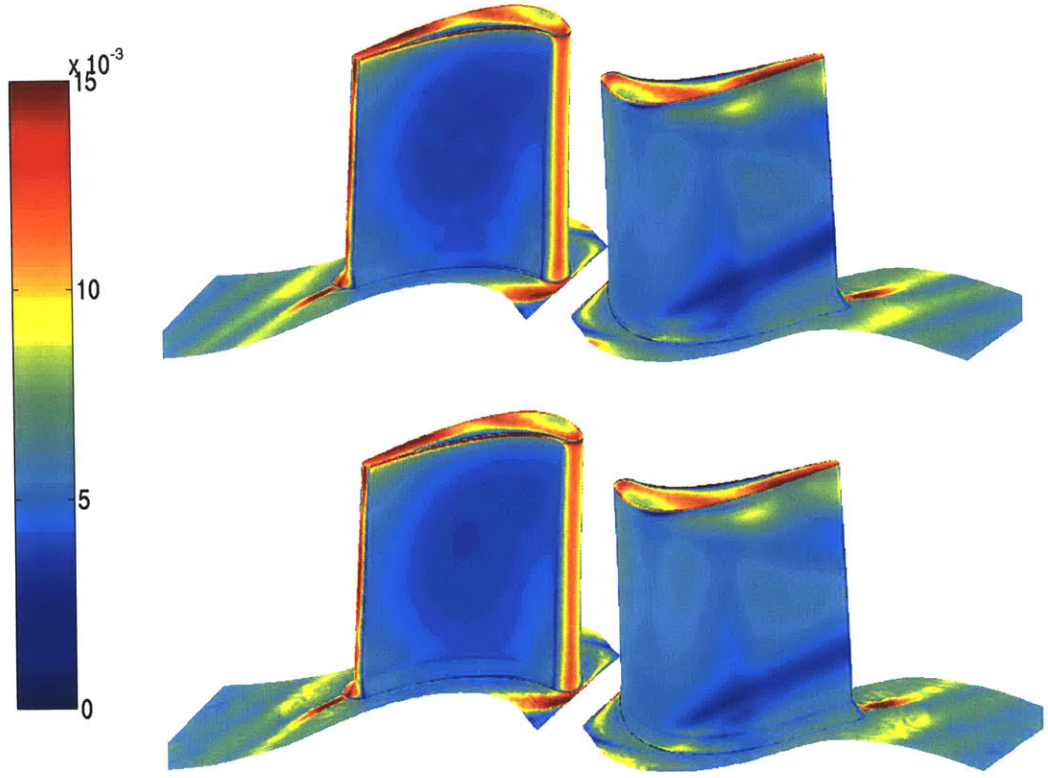

Figure G 1: Blade 1 suction side heat transfer coefficient with nominal (top) and refined (bottom) grid.

Figure G 1 shows the heat transfer coefficient distribution for both the nominal and refined grid on the suction side of the nominal blade. The vortex structures described in Chapter 3 were captured on both grids. The refined grid estimated the changes in heat transfer coefficient in the first 10% span more sharply, particularly where the fillet met the blade. At 10% span, the hot spot below the vortex attachment line was predicted thinner with the refined grid.

A more detailed look at the heat transfer distribution in Figure G 2 shows maximum differences in heat transfer coefficient at 5% span of 45% at S/ARC = 0.4 and 20% in the

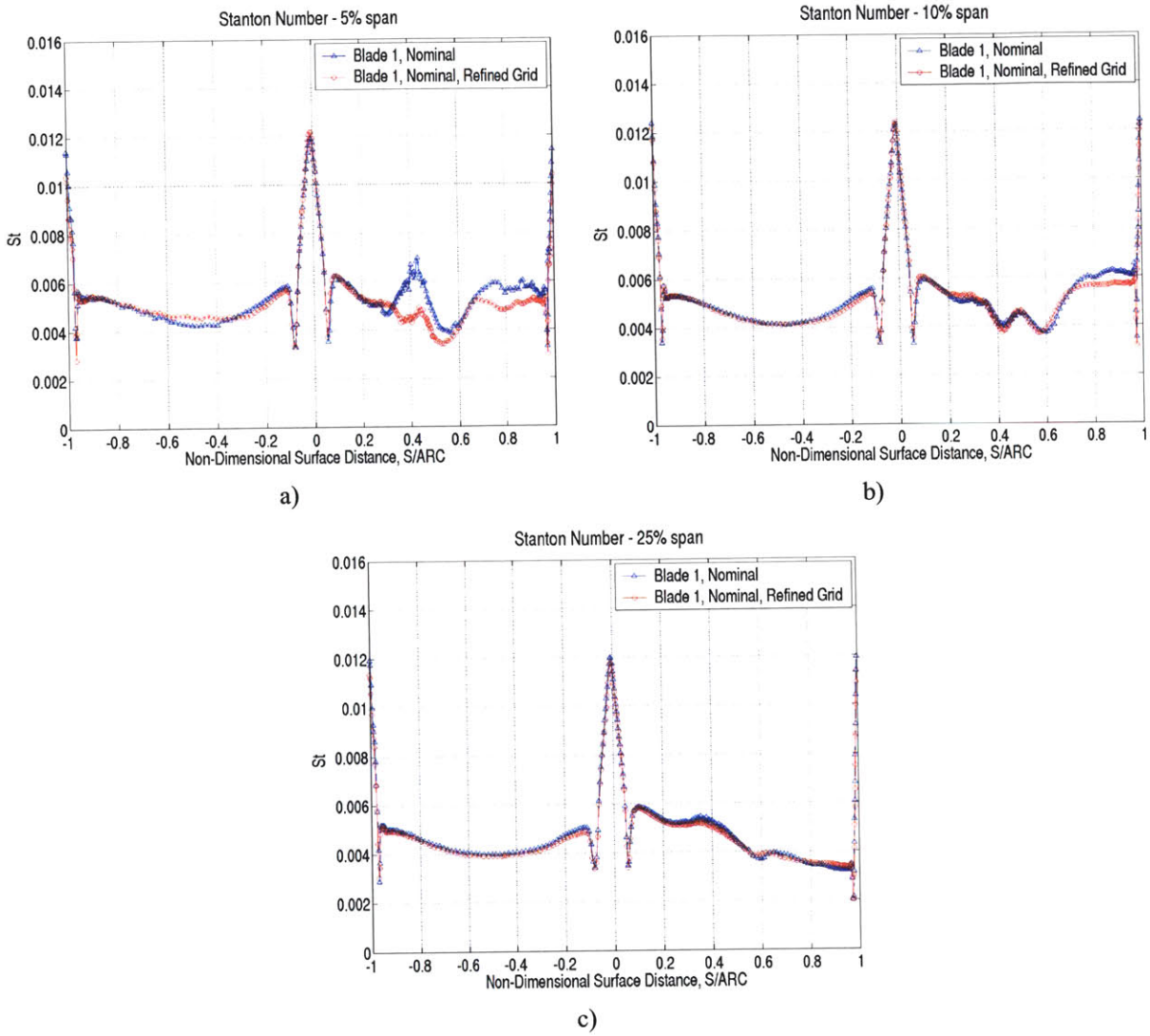

Figure G 2: Three-dimensional heat transfer results on nominal and refined grid: a) 5% span, b) 10% span, c) 25% span.

trailing edge region. Although apparently large, these differences were not expected to affect the life calculations since the differences in heat transfer coefficient are restricted to a very small region where the fillet interfaced with the rest of the blade creating a sharp corner. Such a corner would not exist if the actual fillet geometry had been modeled rather than the straight fillet approximation used in this thesis. Additionally, the FEM model's moderate

level of resolution required for the probabilistic simulations was not likely to capture these localized differences.

More relevant to life are the differences at 10% span. Here, the blade surface was not affected by unrealistically sharp corners. The largest difference in heat transfer coefficient of 10% at 10% span is located on the suction side in the life-limiting region and is a result of the smaller estimated hot spot in this region with the refined grid. On the pressure side, very good agreement was obtained between the two grids. Given the results presented in Chapters 3 and 4, the 10% difference on the suction side was not expected to have an appreciable impact on the life calculations. At 25% span, the heat transfer differences between the calculations were less than 5% everywhere.

Convection boundary conditions were constructed with the data from the calculation on the refined grid and used in an additional deterministic thermal-structural analysis. The stress and strain distributions were very similar to those obtained using the nominal CFD results and a decrease of 0.04% in average equivalent stress was reported. The average equivalent strain in the case with refined grid was reduced by 0.65% from nominal resulting in an increase in life of 1.4%. Given the observed differences in life between the three nominal blades and the apparent low sensitivity of life to the external thermal boundary conditions, CFD grid resolution is deemed to have had no impact on the conclusions from the life calculations. The nominal grid was thus satisfactory for the intended purposes of this study.

H. Additional Three-Dimensional Case Studies

H1 Effect of Root Fillet Geometry

H1.1 Description of Study

The shape of the root fillet was shown to have an impact on secondary flows and their associated losses in a turbine vane passage in [74, 91]. An investigation of the effect of the root fillet geometry on heat transfer was thus carried out.

To approximate the fillet, a straight 45° wedge of side equal to the actual fillet radius was generated at the blade's base. The generation of this baseline fillet geometry was described in Section 2.4.1. An additional fillet geometry was generated which approximated MHI's round fillet with a curved fillet constructed to merge smoothly with the blade surface as opposed to the sharp edge formed in the straight fillet configuration. To assess the impact of the root fillet, irrespective of shape, a third blade geometry was generated with no root fillet. The three fillet geometries investigated are shown in Figure H 1 near the suction side shoulder.

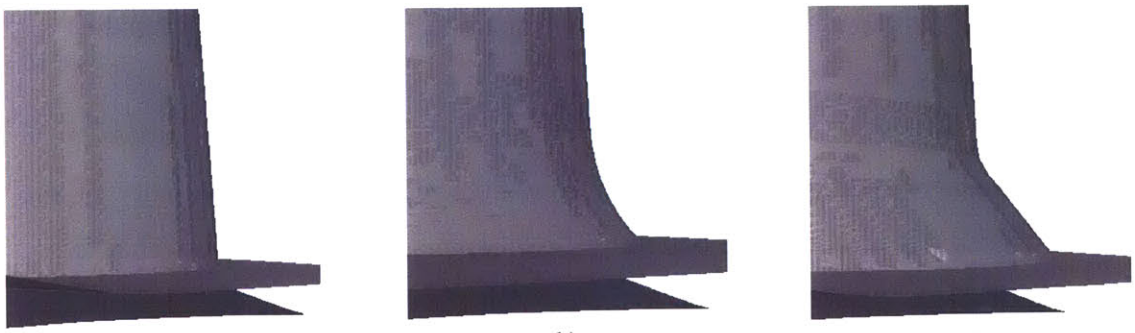

a) b) c)

Figure H 1: Fillet geometries (on suction side) compared for effect on heat transfer and life: a) no fillet, b) curved fillet, c) straight fillet (default)

The actual fillet geometry for Blade 1 is shown in Figure H 2. A similar view of Blade 1 with the straight fillet geometry created in MATLAB is shown in Figure H 3.

The results of the study confirmed that, insofar as its effect on external heat transfer was concerned, the root fillet geometry had a negligible impact on blade life[17].

H1.2 Overall Heat Transfer Comparison

The flow features in this case study's simulations were very similar. The impact of the root fillet geometry on the development of secondary flows reported in [74, 91] was not observed

[17] The reader is cautioned that very different conclusions would likely have resulted here should the various fillet geometries have been modeled in the FEM simulations.

due to the leading edge fillet modifications brought about by the proximity of the cavity here. The modifications resulted in negligible differences in blade-hub interface geometry between the three cases.

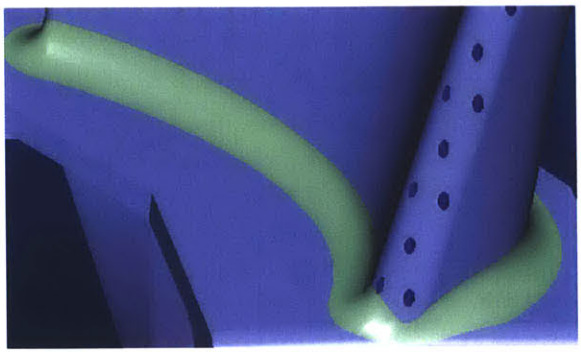

Figure H 2: Actual Blade 1 fillet geometry.

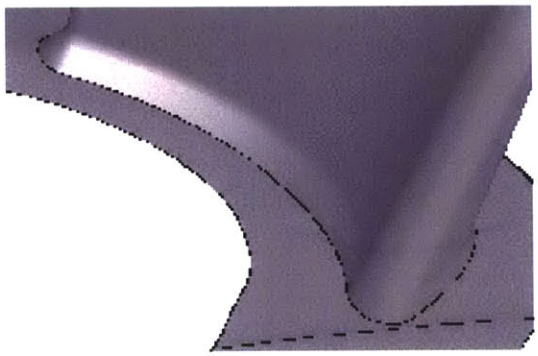

Figure H 3: Straight fillet configuration used in nominal calculations.

On the pressure side, heat transfer differences were confined to the first 5% span. As shown in Figure H 4 a), at 2.5% span, heat transfer was consistently lower for the case without fillet due to spanwise flow impinging on the filleted geometries at this location, increasing heat transfer.

On the suction side, all three simulations predicted a zone of low heat transfer where a low temperature streak convected from the leading edge was pushed spanwise by the incoming passage vortex. In the case with fillets, this streak was smeared spanwise resulting in a delayed and less pronounced low heat transfer peak near S/ARC = 0.4 in Figure H 4 a) and b). The decrease in heat transfer associated with the spanwise migration of the colder hub

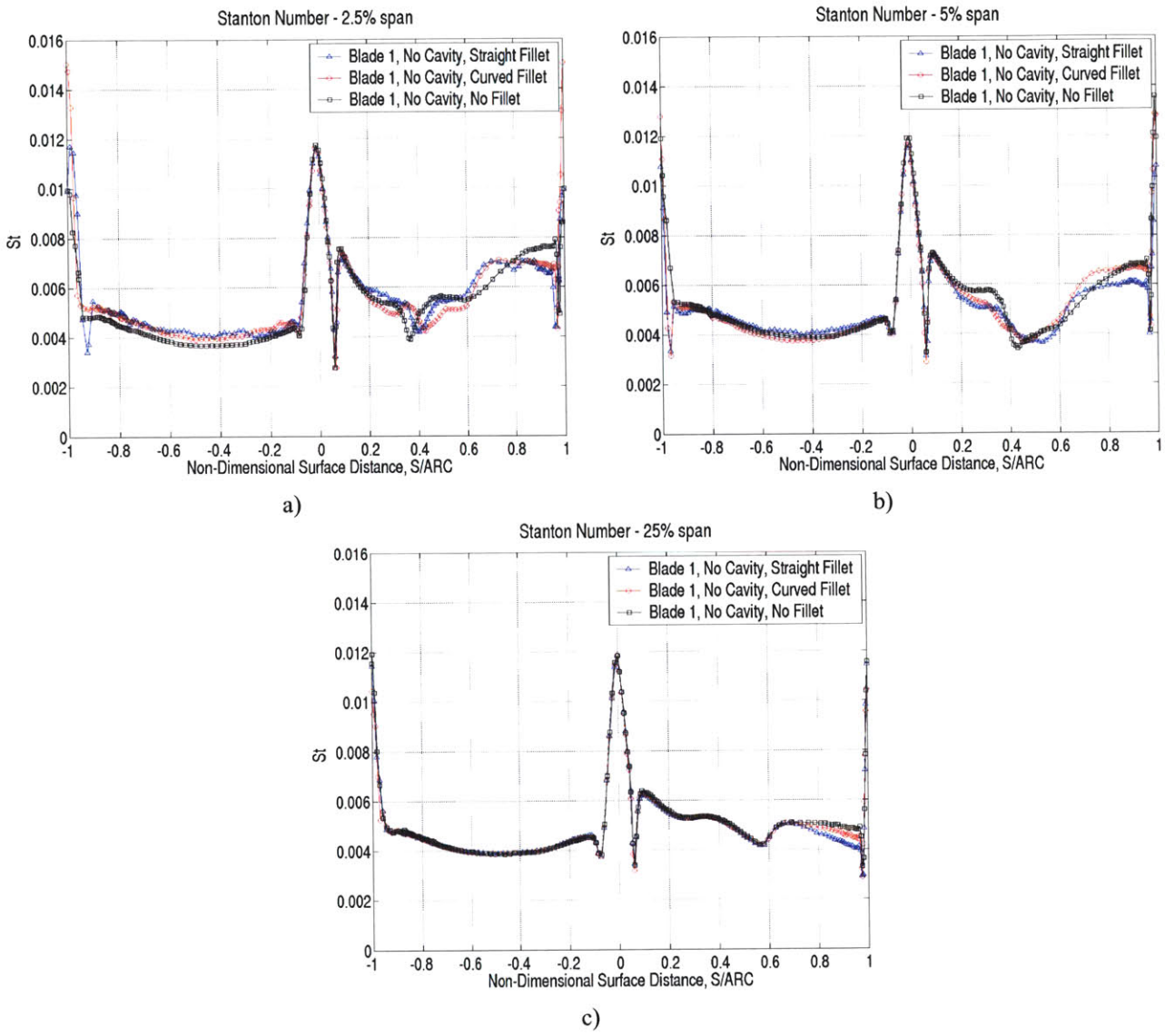

Figure H 4: Effect of root fillet on heat transfer: a) 2.5% span, b) 5% span, c) 25% span.

flow and the passage vortex detachment line was predicted sharper and confined to a smaller region in the case without fillet. Higher spanwise, the vortex structure and its associated cooler flow was ramped up further on the suction side in the case with fillets, the extent of which was larger in the case of the larger straight fillet. This effect is shown in Figure H 4 c) and Figure H 5.

In summary, the flow structures in all three cases were very similar. The blade heat transfer was affected by the root fillet's ability to spread out colder hub flow on the suction side and

exacerbate the passage vortex migration in the spanwise direction. Above 25% span, the root fillet geometry had no impact on external heat transfer.

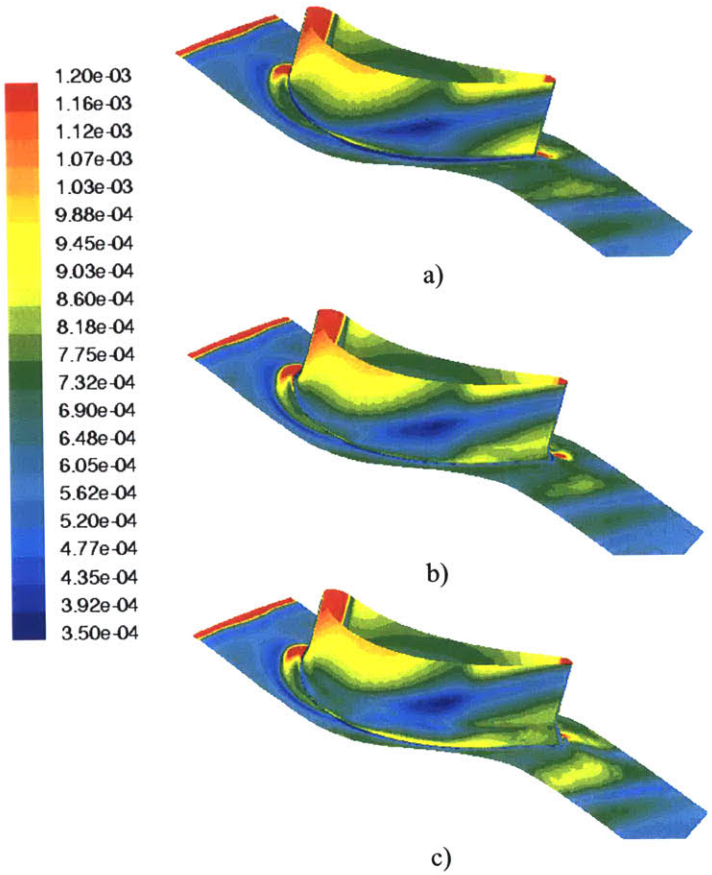

Figure H 5: Three-dimensional suction side heat flux patterns for various fillet geometries (blades shown from 0 to 25% span): a) no fillet, b) curved fillet, c) straight fillet

H1.3 Heat Transfer Comparison in Life-Limiting Region

In the life-limiting region, maximum pressure side differences between the case with straight fillet and that without are 7.4% and 5% at 5% and 10% span respectively. On the suction side, due to differences in the vortex migration path, the maximum differences are 15.3% and 5.5% at 5% and 10% span respectively. Maximum pressure side differences between the case with straight fillet and that with curved fillet were of 4.5% and 4.3% at 5% and 10% span respectively. On the suction side, the maximum differences were 11% and 3.6% at 5% and 10% span respectively.

H1.4 Effect of Root Fillet Geometry on Blade Life

Since only minor differences in heat transfer were observed in the life-limiting region, only quantitative differences in thermal-structural results are presented in Table H 1[18]. The negligible differences in stress, strain, and blade life are consistent with the minor heat transfer differences. The root fillet geometry, insofar as its effect on external heat transfer is concerned, was thus concluded to have a negligible impact on blade life.

	% Difference in Average Equivalent Stress	% Difference in Average Equivalent Strain	% Difference in Estimated Blade Life
No Fillet	0.05	0.09	-0.2
Curved Fillet	0.02	-0.17	0.3

Table H 1: Effect of root fillet geometry on results of thermal-structural calculations.

H2 Effect of Inlet Boundary Layer Without Seal Cavity

H2.1 Description of Study

Endwall boundary layers were not included in the nominal MHI inlet profile. To estimate the heat transfer and life impact of the inlet boundary layer, an additional profile was generated based on the nominal inlet profile and the results of a simulation conducted on the MHI stator. The stator exit circumferentially-averaged total pressure profile was extracted and the near-wall portions were used in generating the new rotor inlet profile. The edges of the boundary layer were determined to be at 6.7% span at the hub and 97.9% span at the casing. Radial equilibrium was maintained in the generation of the new profile. In the freestream region, the total pressure was scaled from the nominal profile values to maintain the same total mass flow to the rotor. The total temperature was maintained as in the nominal profile. To isolate the impact of inlet boundary layers on blade heat transfer, the simulations in this study did not include the seal cavity.

[18] The percentage differences are quoted with respect to the baseline straight fillet geometry.

The inlet boundary layers were found to strengthen secondary flows, increase suction side impingement heat transfer, shift the path of the passage vortex further up on the suction side, and decrease life by 2%.

H2.2 Overall Heat Transfer Comparison

As shown in Table H 2, due to thicker boundary layers and associated larger horseshoe vortex at the blade leading edge, the addition of an inlet boundary layer increased the leading edge peak heat transfer from 5% to 25% span.

On the pressure side, as shown in Figure H 6 a) and b), the computed near-hub heat transfer was higher with boundary layer due to stronger secondary flows entraining hot flow from midspan down the pressure side towards the hub. Figure H 6 c) and d) show that further outboard, pressure side heat transfer was not affected by the presence of boundary layers.

Spanwise Location	Difference in Leading Edge Peak Heat Transfer
5% span	1.7%
10% span	2.9%
25% span	1.5%

Table H 2: Effect of inlet boundary layer without seal cavity on leading edge peak heat transfer.

On the suction side, differences greater than 100% were estimated at 5% and 10% span near S/ARC = 0.5 due to the stronger secondary flows with boundary layer. The pressure side to suction side flow migration occurs further upstream with boundary layer and its impact on suction side heat transfer is shown in Figure H 7. As seen in Figure H 7, with boundary layers, the stronger vortex lifted further off the hub and pulled hot midspan flow to impinge on the suction side in the trailing edge region. The increased spanwise shifting of the vortex attachment-detachment line is responsible for the 30% difference in heat transfer at 25% span. At 50% span, the endwall boundary layers had a negligible effect on heat transfer.

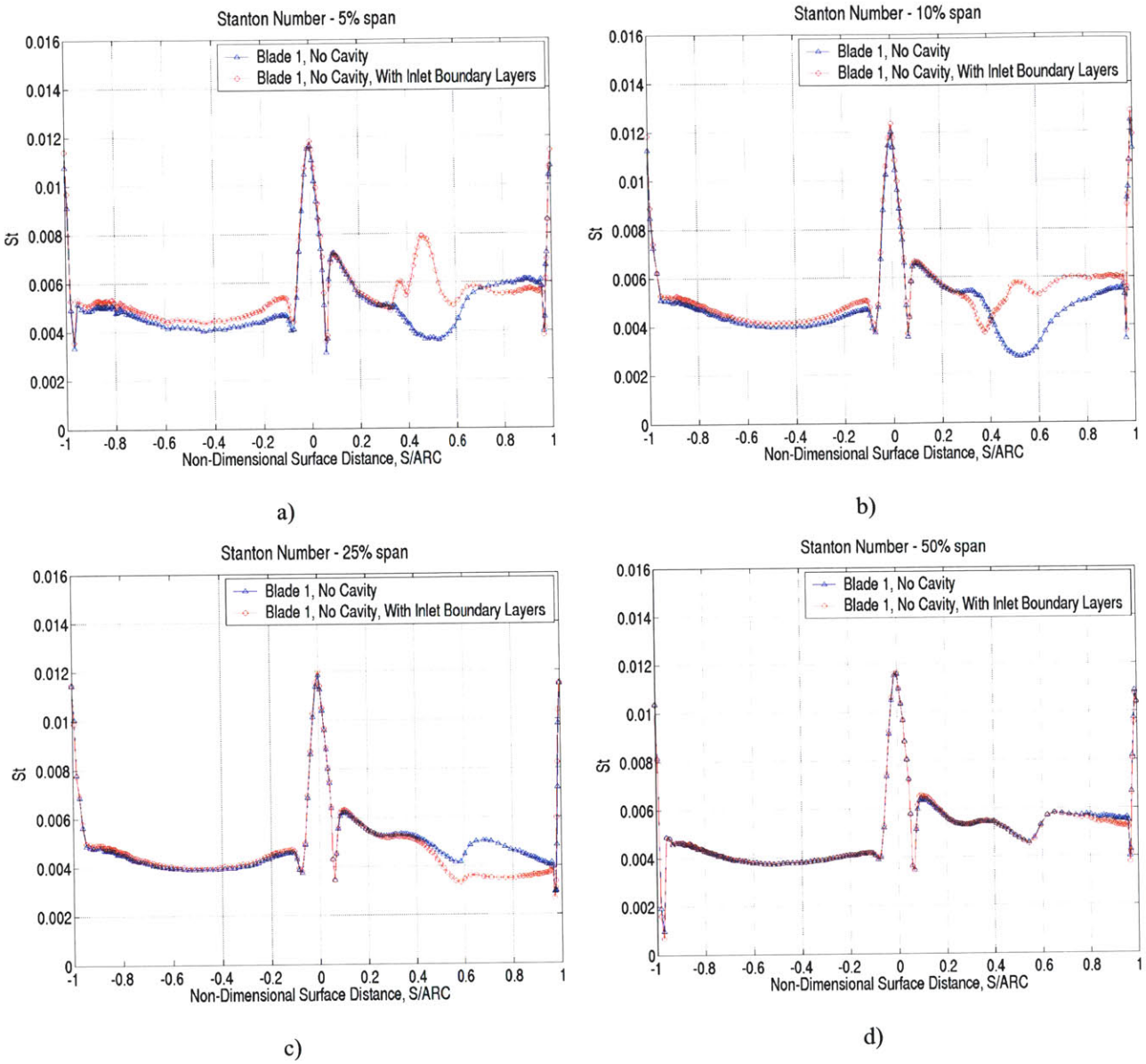

Figure H 6: Effect of inlet boundary layers without seal cavity on heat transfer: a) 5% span, b) 10% span, c) 25% span, d) 50% span.

Above midspan, similar flow features as observed in the lower half of the passage were responsible for the heat transfer differences. Near the casing, a stronger pressure side to suction side flow migration was predicted in the case with boundary layers, postponing the formation of the tip vortex. As shown in Figure H 8 upon impinging on the suction side, the migrating flow was responsible for setting up high heat loads in the tip region.

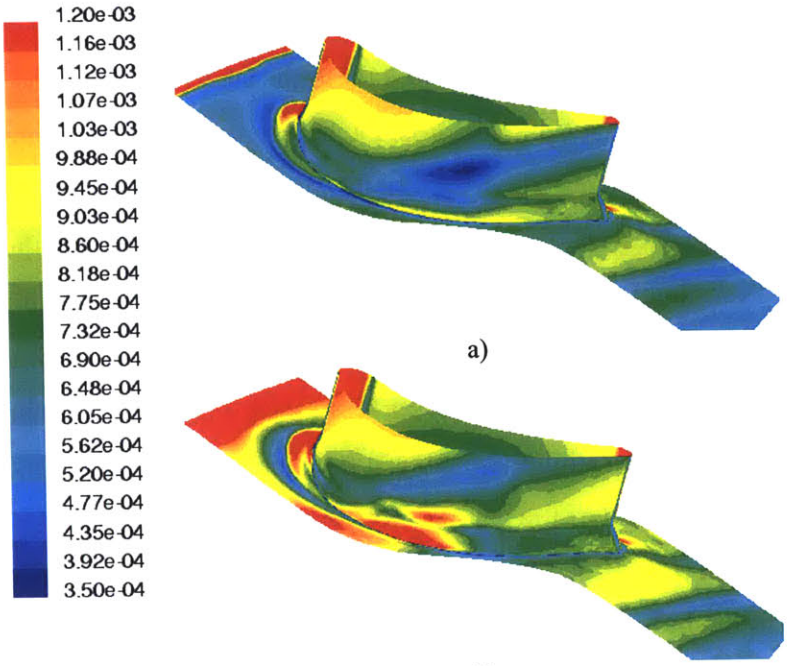

Figure H 7: Three-dimensional heat flux contours showing impact of flow impingement on suction side heat transfer (blades shown from 0 to 25% span): a) without boundary layers, b) with boundary layers.

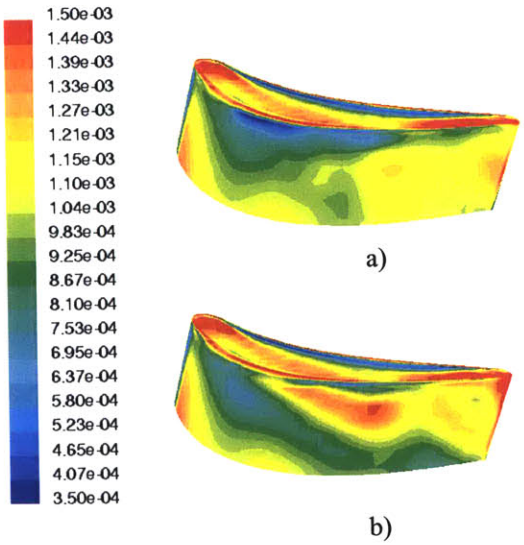

Figure H 8: Three-dimensional heat flux contours showing impact of flow impingement on near-tip suction side heat transfer (blades shown from 75% to 100% span): a) without boundary layer, b) with boundary layer.

H2.3 Heat Transfer Comparison in Life-Limiting Region

In the life-limiting region, on the suction side, the effect of inlet boundary layers was to

increase the heat transfer from the case without boundary layers by 17% at 10% span due to the impingement of higher temperature flow brought to the suction side by the stronger passage vortex. At 5% span, on the suction side, the heat transfer was estimated 6.7% lower than without boundary layer because the location of trailing edge heat transfer augmentation by impingement is lower spanwise in the case without boundary layers. On the pressure side the heat transfer was estimated higher by 4.5% and 3.8% at 5% and 10% span respectively.

In summary, the addition of inlet boundary layers to the case without seal cavity resulted in stronger secondary flows, higher impingement heat transfer near the suction side shoulder, and spanwise shifting in the path of the passage vortex on the suction side. This shifting resulted in increased heat transfer to the upper part of the life limiting region but decreased heat transfer closer to the hub.

H2.4 Effect of Inlet Boundary Layer without Seal Cavity on Blade Life

The metal temperature distribution for both cases considered in this study are shown in Figure H 9. The higher spanwise path of the vortex detachment-attachment line had an effect on the thermal calculations as seen in Figure H 9 b). The life-limiting region remained a hot spot in both simulations.

As in all other case studies presented so far, the stress and strain distributions were once again similar and the location of maximum stress and strain was consistent with that in the nominal comparisons. Increases of 0.06% and 0.97% in average equivalent stress and strain were calculated for the case with inlet boundary layer.

A reduction in life of 2% was estimated for the case with inlet boundary layers. In Section 4.2.1, the addition of the seal cavity to the lower endwall was shown to decrease blade life by 2.6%. As can be seen by comparing the CFD results of Section 4.2.1 and those of the current section, the impact of both features (addition of seal cavity in one instance and addition of inlet boundary layer in another to the case without either feature) on suction side heat transfer was similar in that stronger secondary flows were generated, the vortex attachment-

detachment line was pushed further spanwise, and hotter main gas path flow was pulled down from midspan to impinge on the life-limiting region. Based on the life results of these two case studies, the actual life impact of the two features appears to be minor. However, the fact that the change in estimated life is comparable in both cases points at a consistent trend in the relation between heat transfer and life estimates.

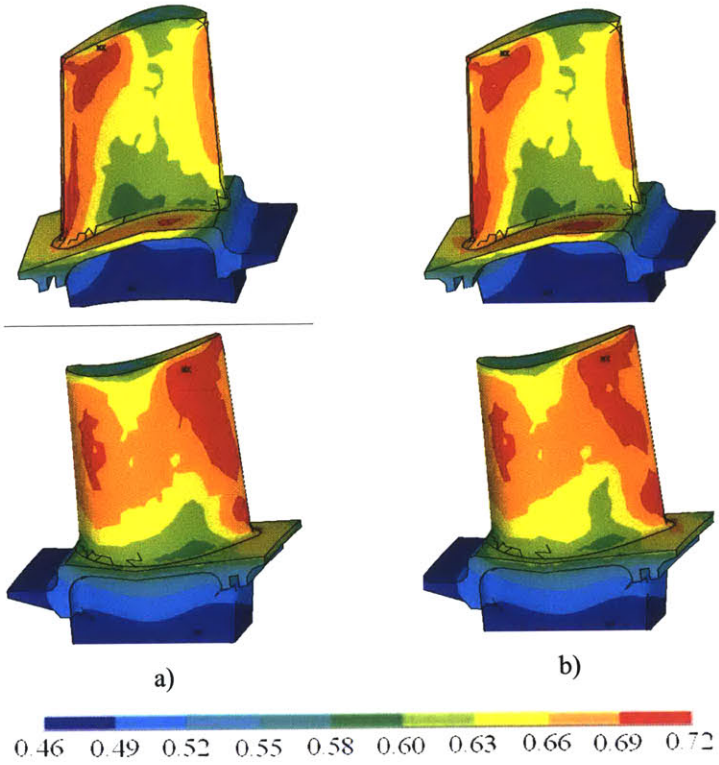

Figure H 9: Metal temperature distributions on pressure (top) and suction (bottom) side: a) without boundary layer, b) with boundary layer.

References and Bibliography

1. *Mitsubishi Heavy Industries, LTD.*, http://www.mhi.co.jp/power/e_power/product/idx_gas_turbine.html, *2003.*

2. *Project Meeting, MHI at MIT, September, 2003.*

3. *GridPro v4.1 User's Guide and Reference Manual for TIL, Ggrid, and Other Utilities.* 1999, Program Development Corporation, 300 Hamilton Ave., Suite 409, White Plains, NY 10601.

4. *The AZ Graphic Manager Manual.* 2000, Program Development Corporation, 300 Hamilton Ave., Suite 409, White Plains, NY 10601.

5. *FLUENT 6.0 User's Guide.* 2001, Fluent Inc., 10 Cavendish Court, Centerra Park Lebanon, NH 03766.

6. *FLUENT 6.1 v^2-f Turbulence Model Manual.* 2003: Fluent Inc., 10 Cavendish Court, Centerra Park Lebanon, NH 03766.

7. Bannister, R.L., Scalzo, A. J., *Evolution of Westinghouse Heavy Duty Power Generation and Industrial Combustion Turbines.* ASME Journal of Engineering for Gas Turbines and Power, 1996. **118**(2): p. 316-330.

8. Behnia, M., Parneix, S., Shabany, Y., Durbin, P. A., *Numerical Study of Turbulent Heat Transfer and Confined and Unconfined Impinging Jets.* International Journal of Heat and Fluid Flow, 1999. **20**: p. 1-9.

9. Blair, M.F., *Influence of Free-Stream Turbulence on Boundary Layer Transition in Favorable Pressure Gradients.* ASME Journal of Engineering for Power, 1982. **104**: p. 743-750.

10. Blair, M.F., *Influence of Free-Stream Turbulence on Turbulent Boundary Layer Heat Transfer and Mean Profile Development, Part 1- Experimental Data.* ASME Journal of Heat Transfer, 1983. **105**: p. 33-40.

11. Blair, M.F., *Influence of Free-Stream Turbulence on Turbulent Boundary Layer Heat Transfer and Mean Profile Development, Part 2 - Analysis of Results.* ASME Journal of Heat Transfer, 1983. **105**: p. 41-47.

12. Bohn, D.E., Becker, V. J., *A Conjugate 3-D Flow and Heat Transfer Analysis of a Thermal Barrier Cooled Turbine Guide Vane.* 98-GT-89, 1998.

13. Bohn, D.E., Becker, V. J., Kusterer, K. A., *3-D Conjugate Flow and Heat Transfer Calculations of a Film-Cooled Turbine Guide Vane at Different Operation Conditions.* 97--GT-23, 1997.

14. Bohn, D.E., Becker, V. J., Kusterer, K. A., Otsuki, Y., Sugimoto, T., Tanaka, R., *3-D Internal Flow and Conjugate Calculations of a Convective Cooled Turbine Blade with Serpentine-Shaped and Ribbed Channels.* 99-GT-220, 1999.

15. Bohn, D.E., Tummers, C., *Numerical 3-D Conjugate Flow and Heat Transfer Investigation of a Transonic Convection-Cooled Thermal Barrier Coated Turbine Guide Vane with Reduced Cooling Fluid Mass Flow.* GT2003-38431, 2003.

16. Boyle, R.J., Giel, P. W., *Three-Dimensional Navier-Stokes Heat Transfer Predictions for Turbine Blade Rows.* AIAA Journal of Propulsion and Power, 1995. **11**(6): p. 1179-1186.

17. Butler, T.L., Sharma, O. P., Joslyn, H. D., Dring, R. P. *Redistribution of an Inlet Temperature Distortion in an Axial Flow Turbine Stage.* in *AIAA/ASME/SAE/ASEE 22nd Joint Propulsion Conference, AIAA-86-1468.* 1986. Huntsville, Alabama.

18. Camci, C., Arts, T., *Experimental Heat Transfer Investigation Around the Film-Cooled Leading Edge of a High-Pressure Gas Turbine Rotor Blade.* ASME Journal of Engineering for Gas Turbines and Power, 1985. **107**: p. 1016-1021.

19. Camci, C., Arts, T., *Short-Duration Measurements and Numerical Simulation of Heat Transfer Along the Suction Side of a Film-Cooled Gas Turbine Blade.* ASME Journal of Engineering for Gas Turbines and Power, 1985. **107**: p. 991-997.

20. Camci, C., Arts, T., *An Experimental Convective Heat Transfer Investigation Around a Film-Cooled Gas Turbine Blade.* ASME Journal of Turbomachinery, 1990. **112**: p. 497-503.

21. Casey, M., Wintergerste, T., *Best Practice Guidelines.* 1.0 ed. ERCOFTAC Special Interest Group on "Quality and Trust in Industrial CFD". 2000.

22. Consigny, H., Richards, B. E., *Short Duration Measurements of Heat-Transfer Rate to a Gas Turbine Rotor Blade.* ASME Journal of Engineering for Power, 1982. **104**: p. 542-551.

23. Dorney, D.J., Davis, R. L., *Navier-Stokes, Analysis of Turbine Blade Heat Transfer and Performance.* ASME Journal of Turbomachinery, 1992. **114**: p. 795-806.

24. Drela, M., *MISES.* 1998: Cambridge.

25. Drela, M., Youngren, H., *A User's Guide to MISES 2.53.* 1998, Cambridge. 61.

26. Drost, U., Bolcs, A., *Performance of a Turbine Airfoil with Multiple Film Cooling Stations Part I: Heat Transfer and Film Cooling Effectiveness.* 1999-GT-171, 1999.

27. Dunham, J., *CFD Validation for Propulsion System Components.* 1997, NATO, AGARD Advisory Report 355.

28. Dunn, M.G., *Convective Heat Transfer and Aerodynamics in Axial Flow Turbines.* ASME Journal of Turbomachinery, 2001. **123**: p. 637-686.

29. Durbin, P.A., *Separated Flow Computations with the k-e-v2 Model.* AIAA Journal, 1995. **33**(4): p. 659-664.

30. Durbin, P.A., *On the k-e Stagnation Point Anomaly.* International Journal of Heat and Fluid Flow, 1996. **17**: p. 89-90.

31. Eckert, E.R.G., *Analysis of Film Cooling and Full-Coverage Film Cooling of Gas Turbine Blades.* ASME Journal of Engineering for Gas Turbines and Power, 1984. **106**: p. 206-213.

32. Garg, V.K., *Heat Transfer on a Film-Cooled Rotating Blade.* International Journal of Heat and Fluid Flow, 2000. **21**: p. 134-145.

33. Garg, V.K., Ameri, A. A., *Two-Equation Turbulence Models for Prediction of Heat Transfer on a Transonic Turbine Blade.* International Journal of Heat and Fluid Flow, 2001. **22**: p. 593-602.

34. Ghia, K., Thornburg, H., Ghia, U., *On Flow in Turbine Cascades and its Management.* AIAA Meeting Papers, 2003(2003-764).

35. Giel, P.W., Bunker, R. S., Van Fossen, J. G., Boyle, R. J., *Heat Transfer Measurements and Predictions on a Power Generation Gas Turbine Blade.* ASME PAPER 2000-GT-209, 2000.

36. Goebel, S.G., Abuaf, N., Lovett, J. A., Lee, C. P., *Measurements of Combustor Velocity and Turbulence Profiles.* ASME Paper 93-GT-228, 1993.

37. Goldstein, R.J., Lau, K. Y., Leung, C. C., *Velocity and Turbulence Measurements in Combustion Systems.* Exp. Fluids, 1983. **1**: p. 93-99.

38. Greitzer, E.M., *Personal Communication.* 2003: Cambridge, Massachusetts.

39. Han, Z.-X., Dennis, B. H., Dulikravich, G. S., *Simultaneous Prediction of External Flow-Field and Temperature in Internally Cooled 3-D Turbine Blade Material.* 2000-GT-253, 2000.

40. Harasgama, S.P., *Combustor Exit Temperature Distortion Effects on Heat Transfer and Aerodynamics within a Rotating Turbine Blade Passage.* ASME Paper 90-GT-174, 1990.

41. Heidemann, J.D., Rigby, D. L., Ameri, A. A., *A Three-Dimensional Coupled Internal/External Simulation of a Film-Cooled Turbine Vane.* ASME Journal of Turbomachinery, 2000. **122**: p. 348-359.

42. Hermanson, K., *Effect of Inlet Conditions on Endwall Secondary Flows, Master of Science Thesis*. 1999, University of Wisconsin: Madison.

43. Hermanson, K.S., Kern, S., Picker, G., Parneix, S, *Predictions of External Heat Transfer for Turbine Vanes and Blades With Secondary Flowfields.* ASME Journal of Turbomachinery, 2002. **125**: p. 107-113.

44. Hermanson, K.S., Thole, K. A., *Effect of Inlet Conditions on Endwall Secondary Flows.* AIAA Journal of Propulsion and Power, 2000. **16**(2): p. 286-296.

45. Hermanson, K.S., Thole, K. A. *Effect of Non-Uniform Inlet Conditions on Endwall Secondary Flows*. in *ASME TURBOEXPO 2002*. 2002. Amsterdam, The Netherlands.

46. Hildebrandt, T., Fottner, L. *A Numerical Study of the Influence of Grid Refinement and Turbulence Modelling on the Flow Field Inside a Highly Loaded Turbine Cascade*. in *International Gas Turbine & Aeroengine Congress & Exhibition*. 1998. Stockholm, Sweden.

47. Irmisch, S., Walker, D., Bettelini, M., Haselacher, A., Benz, E., Kallinderis, Y., *Efficient Use of Hybrid Grids in Modern Turbomachinery Applications.* AIAA Meeting Papers, 1999(99-0783).

48. Kalitzin, G., Iaccarino, G., *Computation of Heat Transfer in a Linear Turbine Cascade.* Center for Turbulence Research Annual Research Briefs, 1999: p. 277-288.

49. Kang, M., Thole, K. A., *Flowfield Measurements in the Endwall Region of a Stator Vane.* ASME Journal of Turbomachinery, 2000. **122**: p. 458-466.

50. Kao, K.-H., Liou, M.-S., *On the Application of Chimera/Unstructured Hybrid Grids for Conjugate Heat Transfer.* 96-GT-156, 1996.

51. Kassab, A.J., Divo, E. A., Rodriguez, F., Steinthorsson, E., *Conjugate Heat Transfer Effects on a Realistic Film-Cooled Turbine Vane.* GT2003-38553, 2003.

52. Kim, K., Cizmas, G. A., *Three-Dimensional Hybrid Mesh Generation for Turbomachinery Airfoils.* Journal of Propulsion and Power, 2002. **18**(3): p. 536-543.

53. Kountras, A., *Probabilistic Analysis of Turbine Blade Durability, Master's Thesis*, in *Aeronautics and Astronautics*. 2004, Massachusetts Institute of Technology: Cambridge, Massachusetts.

54. Kuotmos, P., McGuirk, J. J., *Isothermal Flow in a Gas Turbine Combustor - A Benchmark Experimental Study.* Exp. Fluids, 1989. **7**: p. 344-354.

55. Langston, L.S., *Secondary Flows in Axial Turbines - A Review.* Annals of the New York Academy of Sciences, 2001. **934**: p. 11-26.

56. Larsson, J., *Turbine Blade Heat Transfer Calculations Using Two-Equation Turbulence Models.* Journal of Power and Energy, 1997. **211**(3): p. 253-262.

57. Lee, S.W., Jun, S. B., Park, B-K., Lee, J. S. *Effects of High Free-Stream Turbulence on the Near-Wall Flow and Heat/Mass Transfer on the Endwall of a Linear Turbine Rotor Cascade.* in *ASME Turbo Expo 2002*. 2002. Amsterdam, The Netherlands.

58. Li, H., Kassab, A. J. *Numerical Prediction of Fluid Flow and Heat Transfer in Turbine Blades with Internal Cooling.* in *30th AIAA/ASME/SAE/ASEE Joint Propulsion Conference, AIAA 94-2933*. 1994. Indianapolis, IN.

59. Lien, F.-S., Kalitzin, G., *Computations of Transonic Flow with the v2-f Turbulence Model.* International Journal of Heat and Fluid Flow, 2001. **22**: p. 53-61.

60. Ligrani, P.M., Camci, C., Grady, M. S., *Thin Film Heat Transfer Gauge Construction and Measurement Details.* VKI TM, 1982. **33**.

61. Luo, J., Lakshminarayana, B., *Numerical Simulation of Turbine Blade Boundary Layer and Heat Transfer and Assessment of Turbulence Models.* ASME Journal of Turbomachinery, 1997. **119**: p. 794-801.

62. Mayle, R.E. *The Role of Laminar-Turbulence Transition in Gas Turbine Engines.* in *International Gas Turbine and Aeroengine Congress and Exposition*. 1991. Orlando, FL.

63. Medic, G., Durbin, P. A., *Toward Improved Prediction of Heat Transfer on Turbine Blades.* ASME Journal of Turbomachinery, 2002. **124**: p. 187-192.

64. Parneix, S., Durbin, P. A., Behnia, M., *Computation of a 3D Turbulent Boundary Layer Using the V2F Model.* Flow Turbulence and Combustion, 1998. **10**: p. 19-46.

65. Pasinato, H.D., Liu, Z,. Roy, R. P., Howe, W. J., Squires, K. D., *Prediction and Measurement of the Flow and Heat Transfer Along the Endwall and Within an Inlet Vane Passage.* ASME Turbo Expo 2002 - Technical Papers, 2002(GT-2002-30189): p. 73-79.

66. Priddy, W.J., Bayley, F. J., *Turbulence Measurements in Turbine Blade Passages and Implications for Heat Transfer.* ASME Journal of Turbomachinery, 1988. **110**: p. 73-79.

67. Radomsky, R.W., Thole, K. A., *Flowfield Measurements for a Highly Turbulent Flow in a Stator Vane Passage.* ASME Journal of Turbomachinery, 2000. **122**: p. 255-262.

68. Radomsky, R.W., Thole, K. A., *High Free-Stream Turbulence Effects on Endwall Heat Transfer for a Gas Turbine Stator Vane.* ASME Journal of Turbomachinery, 2000. **122**: p. 699-708.

69. Reiss, H., Bolcs, A., *Experimental Study of Showerhead Cooling on a Cylinder Comparing Several Configurations Using Cylindrical and Shaped Holes.* ASME Journal of Turbomachinery, 2000. **122**: p. 161-169.

70. Rigby, D.L., *Prediction of Heat and Mass Transfer in a Rotating Ribbed Coolant Passage with a 180 Degree Turn.* 98-GT-329, 1998.

71. Rigby, D.L., Steinthorsson, E., Ameri, A. A., *Numerical Prediction of Heat Transfer in a Channel with Ribs and Bleed.* 97-GT-431, 1997.

72. Rohsenow, W.M., Hartnett, J. P., Ganic, E. N., *Handbook of Heat Transfer Applications*. 2 ed. 1985, New York: McGraw-Hill.

73. Sarkar, S. *Analysis of Transitional Flow and Heat Transfer Over Turbine Blades: Algebraic Versus Low-Reynolds Number Turbulence Model.* in *Proceedings of the IMECHE, Part C, Journal of Mechanical Engineering*. 2001.

74. Sauer, H., Müller, R., Vogeler, K., *Reduction of Secondary Flow Losses in Turbine Cascades by Leading Edge Modifications at the Endwall.* ASME Journal of Turbomachinery, 2001. **123**: p. 207-213.

75. Schlichting, H., *Boundary-Layer Theory*. 1987, New York: McGraw-Hill.

76. Schultz, S.L., Jones, T. V., *Heat Transfer Measurements in Short Duration Hypersonic Facilities*. 1973, AGARD.

77. Sharma, O.P., Butler, T. L., *Predictions of Endwall Losses and Secondary Flows in Axial Flow Turbine Cascades.* ASME Journal of Turbomachinery, 1987. **109**: p. 229-236.

78. Sieverding, C.H., *Recent Progress in the Understanding of Basic Aspects of Secondary Flows in Turbine Blade Passages.* ASME Journal of Engineering for Gas Turbines and Power, 1985. **107**: p. 248-257.

79. Sieverding, C.H., Van Den Bosche, P., *The Use of Colored Smoke to Visualize Secondary Flows in a Turbine-Blade Cascade.* Journal of Fluid Mechanics, 1983. **134**: p. 85-89.

80. Simoneau, R.J., Simon, F. F., *Progress Towards Understanding and Predicting Heat Transfer in the Turbine Gas Path.* International Journal of Heat and Fluid Flow, 1993. **14**(2): p. 106-128.

81. Takahashi, T., Watanabe, K., Takahashi, T., *Thermal Conjugate Analysis of a First Stage Blade in a Gas Turbine.* 2000-GT-251, 2000.

82. Takeishi, K.-I., Aoki, S. *Contribution of Heat Transfer to Turbine Blades and Vanes for High Temperature Industrial Gas Turbines Part 1: Film Cooling.* in *International Symposium on Heat Transfer in Gas Turbine Systems*. 2000.

83. Takeishi, K.-I., Aoki, S. *Contribution of Heat Transfer to Turbine Blades and Vanes for High Temperature Industrial Gas Turbines Part 2: Heat Transfer on Serpentine Flow Passage.* in *International Symposium on Heat Transfer in Gas Turbine Systems*. 2000.

84. Taslim, M.E., Bakhtari, K., Liu, H. *Experimental and Numerical Investigation of Impingement on a Rib-Roughened Leading-Edge Wall, GT-2003-38118.* in *Proceedings of the ASME Turbo Expo 2003*. 2003. Atlanta, Georgia.

85. Thole, K.A., Radomsky, R. W., Kang, M. B., Kohli, A., *Elevated freestream turublence effects on heat transfer for a gas turbine vane.* International Journal of Heat and Fluid Flow, 2002. **23**: p. 137-143.

86. Thurman, D., Poinsatte, P., *Experimental Heat Transfer and Bulk Air Temperature Measurements for a Multipass Internal Cooling Model with Ribs and Bleed.* ASME Journal of Turbomachinery, 2001. **123**(90-96).

87. Viswanathan, R., *Damage Mechanisms and Life Assessment of High-Temperature Components*. 1989, Metals Park, Ohio: ASM International. 497.

88. White, F., *Viscous Fluid Flow*. 1974, New York: McGraw-Hill, Inc.

89. Yang, Z., Voke, P. R., Savill, A. M., *Mechanism and Models of Boundary Layer Receptivity Deduced from Large-Eddy Simulation of Bypass Transition.* Direction and Large-Eddy Simulation, 1994. **1**: p. 225-236.

90. York, W.D., Leylek, J. H., *Three-Dimensional Conjugate Heat Transfer Simulation of an Internally-Cooled Gas Turbine Vane.* GT2003-38551, 2003.

91. Zess, G.A., Thole, K. A., *Computational Design and Experimental Evalulation of Using a Leading Edge Fillet on a Gas Turbine Vane.* ASME Journal of Turbomachinery, 2002. **124**: p. 167-175.